SAPIENZA
UNIVERSITÀ DI ROMA

Loss of Landau Damping in Double Harmonic RF Systems

Istituto Nazionale di Fisica Nucleare (INFN) and "Sapienza" Universita di Roma

Dottorato di Ricerca in Fisica degli Acceleratori – XXXVI Ciclo

Leandro Intelisano

ID number 1322671

Advisors

Prof. Mauro Migliorati

Dr. Heiko Damerau

Co-Advisor

Dr. Ivan Karpov

Academic Year 2022/2023

CERN-THESIS-2023-396
31/01/2024

Thesis defended on 31 January 2024
in front of a Board of Examiners composed by:

Prof. Maria Cristina Morone (chairman)

Dr. Elias Metral

Prof. Giandomenico Amendola

Loss of Landau Damping in Double Harmonic RF Systems
Sapienza University of Rome

© 2023 Leandro Intelisano. All rights reserved

This thesis has been typeset by LaTeX and the Sapthesis class.

Version: May 30, 2024

Author's email: leandrointelisano@gmail.com

"The true scientific history of our heritage is richer than all fairy tales and, in its reality, is more mysterious and bizarre than all myths."

- Leon Lederman

Abstract

Landau damping is a natural stabilization mechanism to mitigate coherent beam instabilities. In the absence of synchrotron radiation, it plays a crucial role in hadron accelerators, representing an effective way to maintain the beam stable. A double harmonic RF system is a common technique employed in several accelerators to increase beam stability as well as to perform RF manipulations. This method also finds application in the Proton Synchrotron (PS) and Super Proton Synchrotron (SPS) at CERN, which both utilize higher harmonic RF systems to reach the beam parameters for the High-Luminosity Large Hadron Collider (HL-LHC).

In the longitudinal plane, loss of Landau damping (LLD) occurs when a coherent mode of oscillation moves out of the incoherent band of the bunch synchrotron frequencies. This thesis expands the recent LLD studies to the important case of double harmonic RF systems. It is shown that in the bunch shortening mode (both RF systems in phase at the bunch position for a non-accelerating bucket), inductive impedance above transition energy leads to a vanishing LLD threshold for a binominal particle distribution, similar to the single harmonic RF case.

In this configuration, refined analytical estimates for the synchrotron frequency distribution allowed the derivation of an analytical equation for the LLD threshold by introducing an upper cutoff frequency.

The LLD threshold is extensively studied using the concept of van Kampen modes and taking into account the effect of the voltage ratio and the relative phase between the two RF systems for reactive impedance below and above transition energy. The results are supported by self-consistent numerical calculations based on the Oide-Yokoya method implemented in the code MELODY, as well as macroparticle tacking simulation in BLonD.

This validity of the theoretical studies is demonstrated with extensive beam measurements under different bucket-filling conditions in two synchrotrons, the PS and the SPS. The measurements consist of observing single-bunch oscillations after a rigid-dipole perturbation at the high-energy plateau to minimize space-charge contributions. Beyond the analytical estimates, the observations are moreover compared in detail to the results in the semi-analytical code MELODY and macroparticle simulation in BLonD.

Acknowledgments

Every journey has an end.
After three years, my doctoral studentship is coming to an end. Many people have contributed to increasing my knowledge. Firstly, I would like to express my gratitude to my supervisors at CERN, Dr. Heiko Damerau and Dr. Ivan Karpov, for their daily support, teachings, and valuable suggestions during these three years. I want to thank Dr. Danilo Quartullo and Dr. Fabian Batsch for reading and providing useful comments for this manuscript. I am grateful to all my colleagues in my section for welcoming me warmly into the team and for all the helpful insights. I sincerely thank Dr. Elias Metral and Prof. Oliver Boine-Frankenheim, who kindly accepted to review this manuscript as referee. Last but not least, I want to thank Prof. Mauro Migliorati for the preparation and defense of the thesis. The list of people I should mention at CERN is definitely too long for just one page. Therefore, I will limit myself to expressing my gratitude to all those who have endured and supported me during this period.

A special acknowledgment should be addressed to my family. I thank my father, Pancrazio, and my mother, Iris, who guided me with love during my education and my life, encouraging me to pursue my interests. A special thanks go to Massimo, my brother and point of reference. I also want to remember my uncle Christian, who, together with my father, inspired me and believed in me till the end.

Contents

List of Figures

List of Tables

Chapter 1

Introduction

Particle physics studies the fundamental constituents of matter and explains the physical phenomena through their interactions. Presently, this understanding is consolidated with the so-called standard model [1] of particle physics, which has provided highly precise and robust predictions of experimental observations. Particle accelerators play a key role in advancing the understanding of the fundamental principles of nature. In particular, high-energy accelerators and colliders are the only artificial possibility to achieve the required energy, producing new exotic matter by means of particle collisions. Thanks to the advent of synchrotrons [2, 3], the high alternating magnetic field gradient [4] allowed to accelerate beams of charged particles to energies never achieved before.

Besides nuclear and particle physics, accelerators are now employed in a wide spectrum of applications, spanning from industrial purposes to therapies for cancer treatment. Nevertheless, the demand for high-intensity beams leads to particular challenges, including beam instabilities and particle losses, representing a limitation for present and future projects.

1.1 The CERN Accelerator Complex

The European Organization for Nuclear Research, known as CERN (Conseil Européen pour la Recherche Nucléaire), is a world-renowned institution at the forefront of cutting-edge scientific research. Located on the Franco-Swiss border near Geneva (Switzerland), CERN is home to the largest particle accelerator complex in the world. Over the years, it has been instrumental in advancing our understanding in many scientific areas, shedding new light on particle physics and the fundamental constituents of matter, as well as the principal laws governing the universe.

The accelerator complex at CERN, illustrated in Fig. 1.1, is a sophisticated accelerator chain that works together to accelerate particles to increasingly higher energies. It consists of several different accelerators, each with its specific purpose and function. The injector chain is able to accelerate protons and ions for collisions in the last stage of the accelerator complex and fixed target experiments. As far as the proton beam is concerned, they are generated from negative hydrogen ions. They are accelerated in the Linear Accelerator 4 (LINAC 4) up to a kinetic energy of 160 MeV. The ions are then stripped of their two electrons during injection from

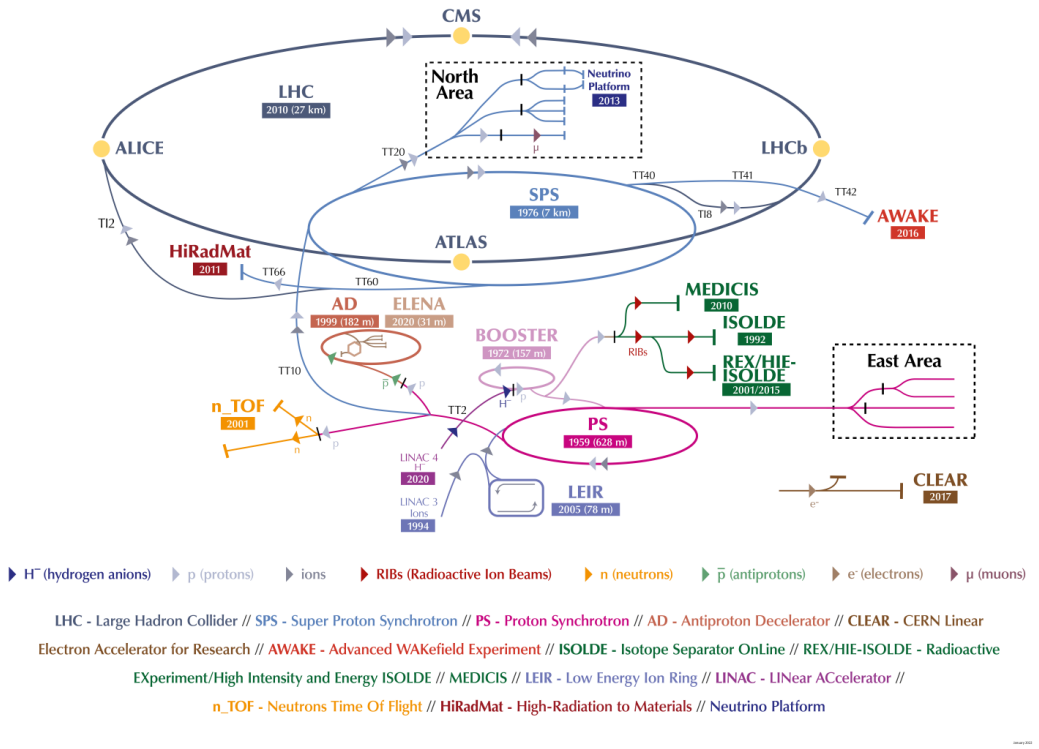

Figure 1.1. Sketch of the CERN accelerator complex. The colored arrows denote the type of accelerated particles and their direction of motion, as illustrated in the legend [5].

LINAC 4 into the Proton Synchrotron Booster (PSB), consisting of four superimposed synchrotron rings, each 157 m long. In the PSB, bunches are formed from the beam using RF manipulation and further accelerated to energies of up to 2 GeV before injecting them into the next accelerator. The Proton Synchrotron (PS) is the oldest synchrotron at CERN and was initially commissioned in 1959. It increases the particle energies up to 26 GeV, providing beams to several experiments and the Super Proton Synchrotron (SPS). The SPS is the largest injector of the complex, pushing the proton beams to reach kinetic energies of 450 GeV. It delivers different types of beams to several experiments, including AWAKE (Advanced WAKefield Experiment [6]), HiRadMat (High-Radiation to Materials [7]), and the North Area [8]. Thereafter, the protons are sent to the final stage of the chain, namely the 27 km long Large Hadron Collider (LHC). Two counter-rotating beams are injected, reaching the nominal energy of 6.8 TeV per beam before colliding in the four detectors: LHCb, ALICE, ATLAS, and CMS. In particular, the latter two had a key role in the discovery of a new boson compatible with the Higgs boson [9, 10].

All the synchrotrons have different limitations and constraints due to intensity effects. Hence, if any accelerator in the chain experiences performance restriction, the beam cannot fulfill the LHC (or related experiment) requirements. The primary aim of the LHC Injectors Upgrade (LIU) project [11] is to discern these limitations and implement remedies that allow delivering the requested beam for the High Luminosity Large Hadron Collider (HL-LHC) project [12]. Currently, one of the main bottlenecks is the SPS, primarily due to issues related to beam loading and

longitudinal instabilities [13–16].

Below, a brief presentation of the two injectors studied in the present work (i.e., PS and SPS) is provided.

1.2 The Proton Synchrotron and LHC-type beam cycle

The PS represents the third stage in the accelerator complex for an LHC-type beam, and it provides the necessary beam also to other projects and accelerators, including the AD (Antiproton Decelerator) [17] and the experiments in the East Area (see Fig. 1.1) [18].

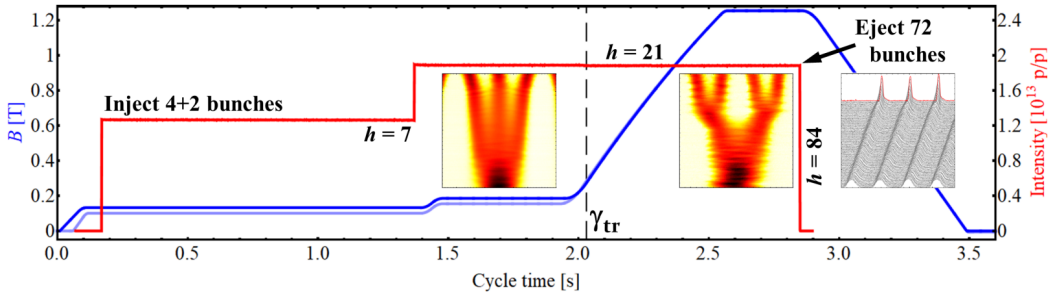

Figure 1.2. Scheme illustrating the generation of the LHC-type beam with 25 ns and intensity $N_p = 2.6 \times 10^{11}$ p/b in the PS. The magnetic cycle before (light blue) and after (dark blue) the long shutdown in 2019-2020 is reported on the left axis [19].

In the framework of the HL-LHC, before the long shutdown of 2019-2020 (LS2), the RF systems of the PS had been majorly upgraded together with the feedback system to fulfill the LIU project requirements. The nominal operational mode for filling the LHC is sketched in Fig. 1.2 [19] for the nominal intensity for HL-LHC $N_p = 2.6 \times 10^{11}$ p/b (proton per bunch). The PS delivers a batch of 72 bunches spaced by 25 ns and 4σ bunch length below 4 ns at extraction. Each batch cycle starts with 6 bunches injected from the PSB with a kinetic energy of 2 GeV and captured by the main RF system (3 MHz) on a harmonic number $h = 7$. After 1.2 s, the bunches are triple split in the intermediate plateau at kinetic energy of 3.1 GeV. The 18 bunches are then accelerated to 26 GeV on harmonic $h = 21$, crossing the transition energy at the beginning of the ramp ($\gamma_{\mathrm{tr}} = 6.1$). Two consecutive splits occur at flat-top energy on $h = 42$ (20 MHz) and $h = 84$ (40 MHz). The 40 MHz, then, in addition to damp quadrupolar coupled-bunch instabilities has to operate throughout the flat-top as a Landau system to enhance the stability. Thereafter, the batch composed of 72 bunches is extracted and sent to the SPS.

1.3 The Super Proton Synchrotron

The SPS, initially commissioned in 1976 for fixed-target experiments, is a versatile synchrotron and the second-largest synchrotron at CERN with a circumference of 6.9 km. It was also used as a proton-antiproton collider (Sp$\bar{\mathrm{p}}$S) and subsequently as an injector for the Large Electron Positron collider (LEP). Nowadays, besides protons, it also accelerates ions.

The high intensity in the SPS leads to several instability mechanisms mostly driven by collective effects. Each particle interacts with its surroundings, leaving behind an electromagnetic field that persists in time, depending on the accelerator component characteristics. This perturbation can be evanescent, affecting only particles from the same bunch or standing longer and affecting the following bunches also in the next turns. The spectral component of this electromagnetic field is referred to as beam coupling impedance (or simply impedance).

In the framework of the LIU project, the SPS has been prepared as an injector for the HL-LHC. The SPS upgrades, include an impedance reduction campaign to reduce the impedance sources arising from the higher-order modes of the RF system. Furthermore, to cope with instabilities and to deliver LHC nominal intensity of 1.15×10^{11} protons per bunch, the SPS is equipped with an additional RF system working at four times the fundamental frequency (800 MHz) operating in phase (in the stationary case) at the bunch position [14, 20]. Eventually, Tab. 1.1 summarizes the current principal accelerator parameters of the SPS for the LHC proton beam, while Tab. 1.2 reports the main fewest parameters of the LIU project.

Table 1.1. The machine parameters of the CERN SPS for the LHC-type beam.

Parameter	**Unit**	**LHC beam type**
Circumference, $2\pi R$	m	6911.55
Beam energy, E_0	GeV	$26 - 450$
Lorentz factor, γ		27.7-479.6
Lorentz factor at transition, γ_t		17.95
Revolution frequency, f_0	kHz	43.29
Main harmonic number, h		4620
Main RF frequency, f_{rf}	MHz	200
Max. RF voltage at fundamental harmonic, V_0	MV	7.5
Frequency of the 4^{th} harmonic RF system	MHz	800
Max. RF voltage of the 4^{th} harmonic RF system	kV	850

Table 1.2. The goals of the LIU project in view of HL-LHC.

Parameter	**Unit**	**Target**
Intensity at flattop, N_p		2.3×10^{11}
Number of bunches per batch		4×72
Bunch spacing	ns	25
Longitudinal emittance, ε_l	eVs	< 0.6
Bunch length, $\tau_{4\sigma}$	ns	< 1.7

1.4 Motivation

In the absence of synchrotron radiation, Landau damping plays a crucial role in hadron synchrotrons, representing the only passive mechanism to suppress coherent instabilities. In the longitudinal plane, it is established by means of the spread of

synchrotron frequencies of individual particles, which is caused by the non-linear voltage of the RF system. In general, loss of Landau damping (LLD) occurs when the frequency of the coherent bunch oscillation emerges from the incoherent synchrotron frequency band.

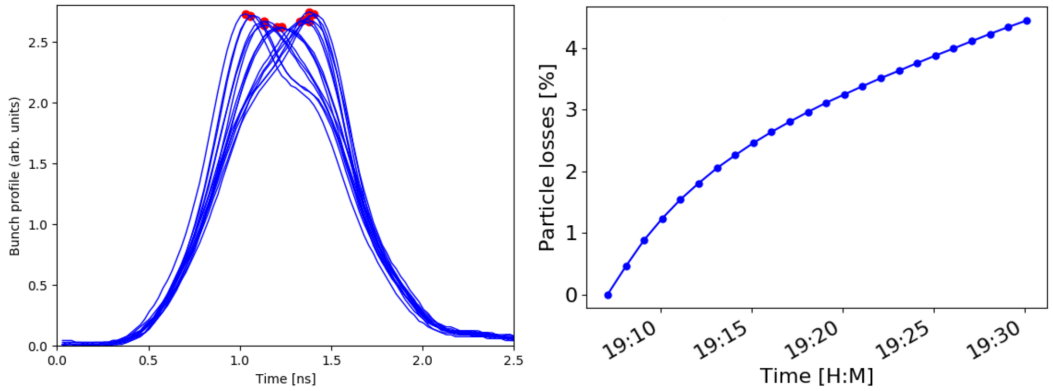

Figure 1.3. Dipole oscillations seen on the bunch profile after the injection (left) and evolution of particle losses (right) in the LHC [21].

The LLD in LHC has been seen since 2010 [22], occurring in different parts of the cycle for bunches with small longitudinal emittances. In particular, undamped or even growing phase oscillations were observed during the ramp. Furthermore, measurements [21] showed that dipole oscillations (Fig. 1.3, left) due to the LLD can lead to particle losses (Fig. 1.3, right). Undampeded coherent motion was also observed at RHIC [23] (Fig. 1.4, left) and Tevatron [24] (Fig. 1.4, right) [24] for proton bunches.

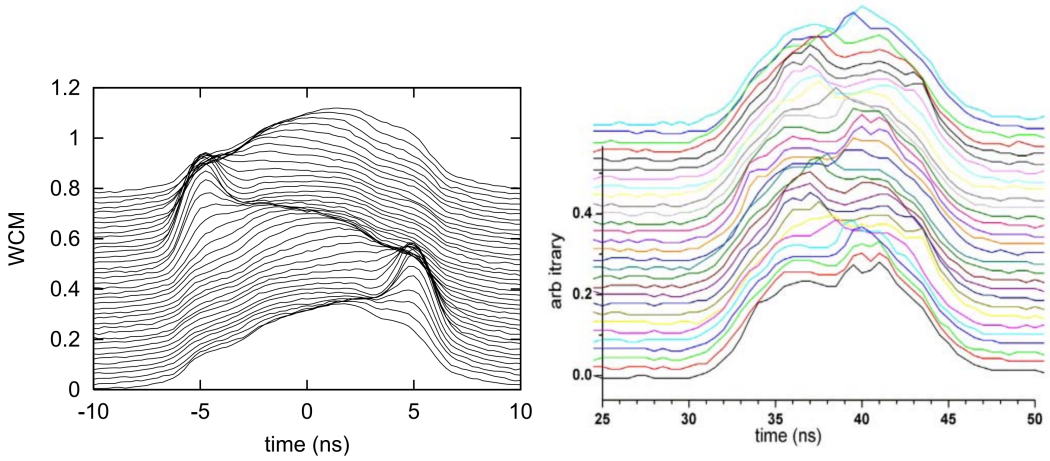

Figure 1.4. Mountain range of the line density. Undamped dipole oscillations in RHIC (left) [23] and in Tevatron (right) [24].

Different techniques are applied to enlarge the synchrotron frequency spread, such as increasing the longitudinal emittance. The most effective method is introducing higher harmonic RF systems (these are often referred to as Landau RF systems). Several accelerators, including the CERN injector synchrotrons, operate with double-

harmonic RF systems (DRF) to enhance the instability threshold [20, 25, 26] and manipulate the bunch shape.

An example is depicted in Fig. 1.5 where a single bunch with full bunch length of $\tau_{\text{full}} = 0.95$ ns is generated considering 1° of initial offset from the center of the RF bucket and tracked for 9×10^5 turns. The simulation is performed with the macroparticle tracking code BLonD (Beam Longitudinal Dynamics simulation suite; Chapter 4) [27–29] using 10^6 macroparticles, representing $N_p = 2.5 \times 10^{10}$ protons and accelerator parameters listed in Tab. 1.1. Considering only the conventional single RF system (Fig. 1.5; left), the dipole oscillation remains even after 9×10^5 turns, suggesting that the Landau damping is lost. This is more visible from the time projection, where the line density evolves similarly to Fig. 1.3. Adding a DRF at a higher harmonic RF system at four times the fundamental RF frequency, with both RF systems in phase (Fig. 1.5; right) increases the LLD threshold, ultimately damping the coherent motion.

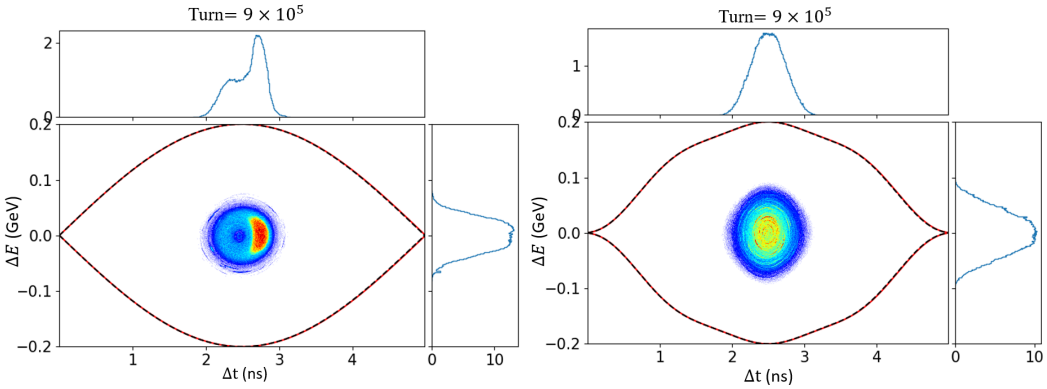

Figure 1.5. Simulated longitudinal phase space after 9×10^5 turns in the SPS (Tab. 1.1) with 1° as initial phase offset with respect to the center of the bucket. The simulations are performed with the macroparticle tracking code BLonD for a full bunch length $\tau_{\text{full}} = 0.95$ ns on the intensity of $N_p = 2.5 \times 10^{10}$ protons and 9×10^5 turns in a single (left) and fourth harmonic RF systems (right). The bucket borders are highlighted in red.

The LLD also plays a key role to the threshold of multi-bunch instabilities. It has been shown that it can modify and lower the coupled bunch instability threshold, $N_{\text{th}}^{\text{CBI}}$ below the LLD threshold in single bunch $N_{\text{th}}^{\text{LLD}}$ leading to a generalized multi-bunch instability threshold that can be summarized as follows [30]:

$$N_{\text{th}}^{\text{Instability}} \approx \frac{N_{\text{th}}^{\text{LLD}} N_{\text{th}}^{\text{CBI}}}{N_{\text{th}}^{\text{LLD}} + N_{\text{th}}^{\text{CBI}}} \,. \tag{1.1}$$

Therefore, if the LLD threshold is comparable to $N_{\text{th}}^{\text{CBI}}$, the resulting multi-bunch instability will be lowered accordingly to Eq. (1.1).

In conclusion, Landau damping is essential in reaching and preserving beam stability in longitudinal and transverse planes. Consequently, gaining a comprehensive understanding and making accurate predictions of the LLD threshold becomes indispensable for single and multi-bunch instability for present (LHC-type beams in the SPS and HL-HLC) and future projects as the Future Circular Collider (FCC) [31].

1.5 Historical background

In 1946, Landau predicted a collisionless damping process of coherent oscillations in an electronic plasma [32]. This phenomenon, referred to as Landau damping, has also found extensive application across various disciplines, spanning hydrodynamics, biophysics, as well as astrophysics. In particle accelerator physics Landau damping was introduced for the first time in [33] and it is a natural mechanism providing beam stability to a wide variety of working high-intensity accelerators.

Several approaches have been developed to assess the LLD threshold. In 1973, Sacherer proposed a stability diagram derived from a general integral equation [34]. The coherent modes were calculated, assuming a linear RF field and neglecting the incoherent frequency spread. The LLD occurs when the coherent mode crosses the boundary of the stability diagram. Similarly to the Sacherer analytical criterion, the LLD threshold was also obtained from the integral form of the Lebedev equation [35] in [36] for a constant reactive impedance.

Hoffman and Pedersen proposed a new method [37] in 1979, to compute the frequency of a rigid-dipole mode, including synchrotron frequency spread in a single harmonic RF system and elliptic particle distribution. Landau damping is lost when the coherent frequency is outside the band of incoherent frequencies. In 2005 and in 2007, Boine-Frankenheim, Shukla, and Chorniy [38, 39] extended the Hofmann-Pedersen approach to the multi-harmonic RF system case. The Sacherer stability criterion and the Hoffman and Pedersen can overestimate the actual LLD threshold due to inherent approximations as seen in calculations [26] and confirmed in measurements [40].

In 1983, Chin, Satoh, and Yokoya [41] contributed to a new description of Landau damping, explaining it as the phase mixing of the van Kampen modes [42, 43]. LLD occurs when any of these modes emerge from the boundaries of the incoherent synchrotron frequencies band. In 2010, Burov [26] applied this concept together with an eigenvalue approach developed by Oide and Yokoya [44] (Chapter 2) to study the LLD threshold without neglecting potential well distortion and synchrotron frequency spread.

Recent works exploited the Lebedev equation and emerged van Kampen mode criterion to determine the LLD thresholds in a single RF system [45]. Contrary to the previous studies, it has been observed that for a particle distribution belonging to the binomial family, the presence of a pure inductive impedance results in a zero LLD threshold unless an upper cutoff to the impedance is introduced. Moreover, both analytical and numerical studies have shown that above transition (or capacitive impedance below transition), the LLD threshold becomes inversely proportional to the cutoff frequency f_c when the cutoff is at high frequency such as $f_c \gg 1/\tau_{\text{full}}$ (τ_{full} represents the full bunch length).

This thesis follows up the aforementioned work, extending the theory to the common case of synchrotrons in double harmonic RF systems. The findings are compared with macroparticle tracking simulations in BLonD, and numerical solutions using the Oide-Yokoya method, as well as extensive beam-based measurements in two synchrotrons, the PS and SPS at CERN.

1.6 Structure of the thesis

The present thesis is structured as follows. After the introduction, Chapter 2 is divided into two main sections. The first briefly reviews the fundamental equations governing longitudinal motion and provides solutions for the single stationary particle in single and DRF. The second part takes into account intensity effects, introducing the perturbation formalism and the linearized Vlasov [46] equation. The solution of the linearized Vlasov equation is found by means of two complementary approaches, namely the Lebedev matrix equation [35] and the Oide-Yokoya method [44]. Eventually, the concept of emerged van Kampen modes [42] as a description of the LLD is presented.

Expanding upon the findings in [45], Chapter 3 develops an analytical expression for the LLD threshold for a constant inductive impedance above transition energy (or capacitive below). The threshold is derived using the Lebedev equation for binomial distributions in a DRF in bunch shortening mode (both RF systems in phase at the bunch position for non-accelerating buckets). Furthermore, the additional force, attributed to the beam-induced voltage, distorts the potential well, leading to the collapse of the bucket. The limiting conditions for a binomial particle distribution are calculated.

The semi-analytical and numerical approaches used in this thesis are presented in Chapter 4, namely the Matrix Equations for LOngitudinal beam DYnamics (MELODY) [47] and the macroparticle tracking code BLonD.

Chapter 5 is dedicated to studying the LLD, applying both codes for a constant inductive impedance above and below transition energy. In particular, in the bunch shortening mode above transition, the analytical LLD threshold is extensively tested with the Oide-Yokoya method implemented in MELODY. Furthermore, we demonstrate the monotonicity of the LLD threshold along the bunch length, which differs from previous studies in [25]. A method to visualize coherent modes behavior versus the intensity is presented in BLonD and compared with the van Kampen modes computed in MELODY. Different bunch lengths are covered to analyze the impact on the coherent modes due to the presence of local minima in the synchrotron frequency distribution. Thereafter, the case of the DRF system operating in bunch lengthening mode (both RF systems in counter-phase at the bunch position) is examined. The limitations caused by the zero derivatives of the frequency distribution leading to vanishing LLD threshold at any intensity, as well as the relative phase between the RF systems, are illustrated. The study is repeated below transition energy, revealing a distinctly different behavior for the LLD threshold in contrast to the above transition case. In this regime, the additional focusing force, due to the beam-induced voltage, narrows the potential well, ultimately collapsing the bucket. This phenomenon can occur before reaching the LLD threshold, even for short bunches. The limiting conditions are evaluated using the analytical equation and benchmarked with MELODY.

Chapter 6, introduces a method for studying LLD through the beam response to a longitudinal rigid-dipole perturbation. In particular, simulations of the bunch offset evolution for a constant inductive impedance are presented and compared to reconstructed bunch offset evolution from perturbations expanded as a series of van Kampen modes. This method was therefore applied in two distinct accelerators

operating under different conditions: the SPS (Chapter 7) and PS (Chapter 8). The findings of this extensive campaign of beam measurements are presented and compared to semianalytical calculations using the code MELODY and macroparticle tracking simulations in BLonD.

Chapter 2

Fundamentals of longitudinal beam dynamics in synchrotrons

Longitudinal beam dynamics is the field of study in accelerator physics that focuses on the behavior, manipulation, and control of charged particle beams along their longitudinal axis, corresponding to their motion in the direction of the beam. This field includes various phenomena such as acceleration, deceleration, energy modulation, phase stability, as well as beam interactions with RF cavities and the surrounding environment [25, 48–52].

The fundamental principles of longitudinal beam dynamics in synchrotrons are introduced in this section. The concepts will then serve as a basis and find extensive application in the subsequent chapters of this thesis.

2.1 Single particle motion

A synchrotron is a specialized type of circular particle accelerator that utilizes electromagnetic fields to accelerate and confine a charged particle beam on a closed orbit. The acceleration of particles is achieved through the electric field, while magnetic fields bend and focus the particle beam along its curved path. The bending radius of the particle is determined by its momentum and the strength of the magnetic bending field. As the particles gain energy during the acceleration process, the magnetic field is precisely synchronized with the gain in momentum to keep the bending radius constant.

2.1.1 Synchronism condition

The force experienced by a particle with charge q as it moves through an electromagnetic field with velocity, v, is given by the Lorentz force

$$\vec{F} = q(\vec{\mathscr{E}} + \vec{v} \times \vec{B}) \,, \tag{2.1}$$

where the electric field, $\vec{\mathscr{E}}$, and magnetic field, $\vec{B}$, are provided by the RF cavities and the magnets placed along the ring, respectively.

In order to fix the particle trajectory to the reference orbit[1], dipole magnets are placed along the circumference to bend the beam. These bending magnets define a bending radius ρ and a vertical magnetic field with an amplitude B. In Fig. 2.1,

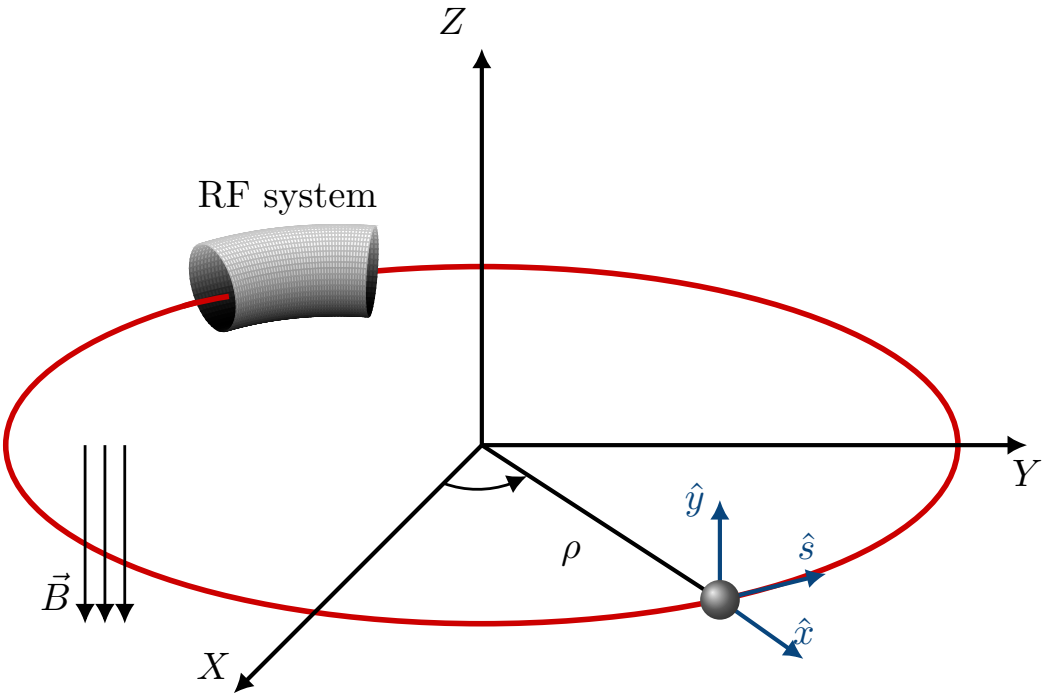

Figure 2.1. Sketch of a synchrotron with a bending radius ρ. Two distinct coordinate systems are employed to describe the particle motion. The first coordinate system is the classical Cartesian coordinate system attached to the laboratory frame. The second $(\hat{x}, \hat{y}, \hat{s})$ is fixed to the moving particle. A magnetic induction field $\vec{B}$ is in the ring circumference perpendicular to the direction $\hat{s}$. An RF system supplies a dynamic electric field $\vec{\mathscr{E}}$, providing acceleration longitudinally.

a simplified illustration of the particle position is presented. Conventionally, the position of a particle is described using a reference frame fixed to the particle itself, employing the coordinate system $(\hat{x}, \hat{y}, \hat{s})$, also called Frenet-Serret coordinate system (Appendix A). The particle is maintained at a fixed orbit by the magnetic field $\vec{B}$ perpendicular to the direction $\hat{s}$. The acceleration then is periodically provided by the RF system[2] with the revolution period:

$$T_0 = \frac{1}{f_0} = \frac{C}{\beta c}\,, \tag{2.2}$$

where C is the accelerator circumference and $\beta = v/c$ is the ratio of the particle velocity, v, and the speed of light, c. In the stationary case, synchronism implies that

[1] Design orbit on which the center of the quadrupole magnets are aligned.

[2] For circular machines DC acceleration is impossible as

$$\oint \vec{\mathscr{E}} \cdot d\hat{s} = 0$$

the reference (or synchronous) particle must be synchronized with the RF cavity to arrive at each turn at the same RF phase, i.e., $\phi_{\mathrm{rf}} = \phi_{s0}$, where ϕ_{s0} referred to us synchronous phase. Moreover, for sinusoidal RF voltages, the RF system must be periodic with the revolution period, i.e.,

$$f_{\mathrm{rf}} = h f_0 \,, \tag{2.3}$$

where h is the RF harmonic number, and $f_{\mathrm{rf}} = \phi_{\mathrm{rf}}/(2\pi t)$ expresses the frequency of the RF system, with t representing the time variable. This leads to an additional relation linking the synchronous phase ϕ_{s0} to the azimuthal position θ, i.e.:

$$\phi_{s0} = h\theta_{s0} \,. \tag{2.4}$$

A substantial portion of the accelerator ring is generally dedicated to accommodating the bending magnets. For instance, in the context of the SPS, dipole magnets occupy approximately 78% of the entire ring. Consequently, the circumference is not perfectly circular but consists of curved and several straight sections. The straight sections offer the necessary space to several types of devices spanning from RF systems to beam diagnostics, multi-pole magnets (quadrupole, sextupole, etc.), as well as injection and extraction systems. Hence, the total circumference C is linked to the bending radius ρ and the length of the remaining straight sections L; namely:

$$C = 2\pi R = 2\pi\rho + L \,, \tag{2.5}$$

where R is the average radius of the whole accelerator.

The product of the magnetic field strength required to maintain particles with the momentum p on the reference orbit and the bending radius ρ is referred to as magnetic rigidity

$$B\rho = p/q \,. \tag{2.6}$$

Hence, it is essential to increase the magnetic field strength during the acceleration process by synchronizing it with the frequency of the RF system.

2.1.2 Energy gain per turn

In order to accelerate a charged particle, the RF system provides a longitudinal time-varying electric field $\mathscr{E}$ of the following form:

$$\mathscr{E}(t) = \mathscr{E}_0 \sin(\omega_{\mathrm{rf}} t + \phi_{\mathrm{rf}}) \,, \tag{2.7}$$

where $\mathscr{E}_0$ and ϕ_{rf} are, respectively, the designed amplitude and phase of the electric field. Let us consider an RF cavity with an inner gap with length, g. The amplitude $\mathscr{E}_0$ is assumed to be constant inside the gap. Therefore, the energy gained by a particle over a single passage inside a cavity is equal to:

$$(\Delta E)_{\mathrm{gain}} = q \int_{-g/2}^{g/2} \vec{\mathscr{E}} \cdot d\hat{s} = q\mathscr{E}_0 \int_{-g/2}^{g/2} \sin\left(\frac{\omega_{\mathrm{rf}}}{v} s + \phi_{\mathrm{rf}}\right) ds \,. \tag{2.8}$$

Assuming a symmetric gap with respect to the longitudinal axis, as shown in

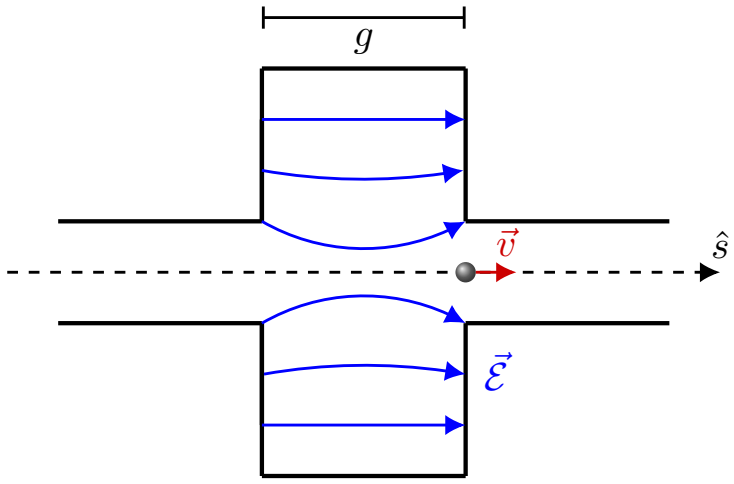

Figure 2.2. Electric field vectors in the cavity gap g. The direction of the particle is illustrated in red with its velocity vector. The gap is assumed symmetric with respect to the axis $\hat{s}$.

Fig. 2.2, the Eq. (2.8) for the synchronous particle can be solved as follows:

$$(\Delta E)_{\text{gain}} = q\mathscr{E}_0 \int_{-g/2}^{g/2} \cos\left(\frac{\omega_{\text{rf}}}{v}s\right) \sin\left(\phi_{\text{rf}}\right) ds = \frac{2q\mathscr{E}_0 v \sin\left(\phi_{\text{rf}}\right)}{\omega_{\text{rf}}} \sin\left(g\frac{\omega_{\text{rf}}}{2v}\right) . \quad (2.9)$$

The provided expression is obtained considering the sum trigonometric identity in conjunction with the observation that the cosine function has even symmetry over the interval $[-g/2, g/2]$. Rearranging Eq. (2.9), yields:

$$(\Delta E)_{\text{gain}} = qV_0 T \sin\phi_{\text{rf}} , \quad (2.10)$$

where $V_0 = \mathscr{E}_0 g$ and T is the transit time factor[3] equal to:

$$T = \frac{\sin\left(g\frac{\omega_{\text{rf}}}{2v}\right)}{g\frac{\omega_{\text{rf}}}{2v}} . \quad (2.11)$$

In general, $T < 1$, and for a short gap that is traversed much faster than the RF period, the transit time factor asymptotically approaches unity, $T \approx 1$.

2.1.3 Non-synchronous particle and equation of motion

Let us consider a particle with deviations in terms of energy and phase with respect to the synchronous particle, i.e.,

$$\begin{cases} \phi = \varphi - \phi_{s0}, \\ \Delta E = E - E_0, \\ \Delta\theta = \theta - \theta_{s0}, \\ \Delta p = p - p_0, \end{cases} \quad (2.12)$$

[3]The transit time factor arises from the fact that the field changes while the particle passes through the cavity.

where φ, E, θ, and p are the phase of the particle with respect to the RF wave, energy, azimuthal orbital angle, and momentum for an off-momentum particle. Similarly, ϕ_{s0}, E_{s0}, θ_{s0}, and p_0 represent the corresponding parameters for the synchronous particle. Therefore, Eq. (2.4) for a non synchronous particle becomes:

$$\phi = -h\Delta\theta\,. \tag{2.13}$$

The negative sign indicates that the particles that are behind the synchronous one, i.e., $\Delta\theta < 0$ will arrive later in the RF cavity, meaning $\phi > 0$.

Taking into account Eq. (2.13), the angular revolution frequency deviation of a particle can be written as:

$$\Delta\omega = \frac{d}{dt}\Delta\theta = -\frac{1}{h}\frac{d\phi}{dt} = -\frac{1}{h}\frac{d\varphi}{dt}\,. \tag{2.14}$$

Given that $\omega_0 = 2\pi\beta c/C$, the relative change of the angular revolution frequency with respect to the synchronous particle can be alternatively expressed as

$$\frac{\Delta\omega}{\omega_0} = \frac{C}{R}\Delta\beta - \frac{\beta C}{R^2}\Delta R = \frac{\Delta\beta}{\beta} - \frac{\Delta C}{C}\,. \tag{2.15}$$

A particle with a small deviation Δp from the reference momentum p_0 results in a different bending radius $\Delta\rho$ within the dipole magnets and consequently a different orbit radius ΔR in the synchrotron, as described by Eqs. (2.5) and (2.6). This phenomenon, known as dispersion, is a fundamental aspect of transverse beam dynamics and is quantified by the dispersion function $D_x(s)$ along the ring. The relationship between Δp and ΔR is obtained by integrating the dispersion function over one complete turn in the synchrotron, leading to the definition of the momentum compaction factor α according to

$$\alpha = \frac{1}{C}\oint \frac{D_x(s)}{\rho(s)}ds = \frac{\Delta R/R}{\Delta p/p_0}\,. \tag{2.16}$$

Most high-energy synchrotrons have a positive momentum compaction factor[4], $\alpha > 0$.

From $p = m_0 c\beta\gamma = p_0 + \Delta p$ where $\gamma = 1/\sqrt{1-\beta^2}$ is the so-called Lorentz factor and m_0 the rest mass of the particle, one obtains the relation

$$\frac{\Delta p}{p_0} = \gamma^2\frac{\Delta\beta}{\beta}\,. \tag{2.17}$$

Combining Eqs. (2.15) and (2.17) yields to

$$\frac{\Delta\omega}{\omega_0} = \left(\frac{1}{\gamma^2} - \alpha\right)\frac{\Delta p}{p_0} = -\eta\frac{\Delta p}{p_0}\,, \tag{2.18}$$

where η is the slip factor

$$\eta = \alpha - \frac{1}{\gamma^2}\,. \tag{2.19}$$

[4]Some specially designed synchrotrons have $\alpha < 0$ where the orbit length is shorter for higher-energy particles. An example is the superKEKB (for hadrons J-PARC MR) in Japan [53].

At the critical point where the Lorentz factor $\gamma = 1/\sqrt{\alpha} \triangleq \gamma_{\mathrm{tr}}$, particles with different energy circulate with the same revolution frequency and $\eta = 0$. This energy is called transition energy. Specifically, it sets the boundary of two distinct regimes, namely, below and above transition energy (Sec. 2.1.4).

The first equation of motion, i.e., the time evolution of the particle phase, can be derived by inserting Eq. (2.18) into Eq. (2.14), yielding:

$$\frac{d\phi}{dt} = \dot{\phi} = h\eta\omega_0 \frac{\Delta p}{p_0} = \frac{h\eta\omega_0}{\beta^2}\frac{\Delta E}{E_0} = \frac{h^2\eta\omega_0^2}{\beta^2 E_0}\left(\frac{\Delta E}{h\omega_0}\right) . \tag{2.20}$$

We now derive the second equation of motion, which takes into account the time evolution of the energy deviation ΔE. For the sake of simplicity, we neglect at this stage all types of interaction between particles and the surroundings (it will be taken into account later). The change in energy depends uniquely on the RF system. Furthermore, we consider an arbitrary RF voltage function $V_{\mathrm{rf}}(\phi)$ to include multi-harmonic RF systems. The conditions that $V_{\mathrm{rf}}(\phi)$ has to fulfill are the periodicity and absence of DC components, i.e.:

$$V_{\mathrm{rf}}(\phi) = V_{\mathrm{rf}}(\phi + 2\pi) \quad \text{and} \quad \int_0^{2\pi} V_{\mathrm{rf}}(\phi)d\phi = 0\,. \tag{2.21}$$

The energy gain per revolution for a non-synchronous particle is:

$$\begin{cases} E_n - E_{n-1} = qV_{\mathrm{rf}}(\phi)\,, \\ E_{n,0} - E_{n-1,0} = 0\,. \end{cases} \tag{2.22}$$

Therefore, we consider the difference in gained energy from the synchronous particle

$$(E_n - E_{n-1}) - (E_{n,0} - E_{n-1,0}) = qV_{\mathrm{rf}}(\phi)\,. \tag{2.23}$$

Dividing by the revolution period T_0 on the first term of Eq. (2.23), we obtain:

$$\frac{2\pi}{\omega_0 T_0}\left(\Delta E_n - \Delta E_{n-1}\right) \approx 2\pi\frac{d}{dt}\left(\frac{\Delta E}{\omega_0}\right) . \tag{2.24}$$

The equality of the incremental ratio to the time derivative of the energy difference is justified by the fact that in synchrotrons, the acceleration cycle typically spans many revolutions, ranging from thousands to millions. Therefore, the particle gains only a small amount of energy during each turn, making ΔE a smooth function of time. From Eq. (2.22), we obtain the first equation of motion describing the evolution of the energy deviation with time, i.e.,

$$\frac{d}{dt}\left(\frac{\Delta E}{h\omega_0}\right) = \frac{q}{2\pi h}V_{\mathrm{rf}}(\phi)\,. \tag{2.25}$$

Equations (2.25) and (2.20) can be combined to obtain a more compact expression in the form of a second-order differential equation

$$\frac{d^2\phi}{dt^2} - \frac{h\eta\omega_0^2 q}{2\pi\beta^2 E_0}V_{\mathrm{rf}}(\phi) - = \frac{d^2\phi}{dt^2} + \omega_{s0}^2\ V_{\mathrm{rf}}(\phi) = 0\,. \tag{2.26}$$

2.1.4 Single harmonic RF system

We have established the main concepts of the longitudinal equation of motion for an arbitrary RF voltage. The simple case of a single harmonic RF system is now being considered, assuming a sinusoidal RF voltage.

Small amplitude approximation and phase-stability

In a single harmonic RF system, the electric field is described by Eq. (2.7). We, therefore, simplify Eq. (2.26), as follows:

$$\frac{d^2\phi}{dt^2} - \frac{h\eta\omega_0^2 qV_0}{2\pi\beta^2 E_0}\sin(\phi+\phi_{s0}) = 0\,. \tag{2.27}$$

This equation can be linearized for small phase offset ϕ. Hence, the sine function in Eq. (2.27) can be simplified to

$$\sin(\phi+\phi_{s0}) = \cos\phi_{s0}\sin\phi + \cos\phi\sin\phi_{s0} \approx \phi_{s0}\cos\phi_{s0}\,, \tag{2.28}$$

and, substituting into Eq. (2.27), results in:

$$\frac{d^2\phi}{dt^2} + \omega_{s0}^2\phi = 0\,. \tag{2.29}$$

This expression describes the differential equation of a harmonic oscillator characterized by its angular frequency ω_{s0}, also referred to as the small-amplitude synchrotron frequency:

$$\omega_{s0} = \sqrt{-\frac{h\omega_0^2\eta\cos\phi_{s0}qV_0}{2\pi\beta^2E_0}}\,. \tag{2.30}$$

To ensure the stability of the system, this synchrotron frequency must to be a real value, i.e.:

$$\eta\cos\phi_{s0} < 0\,. \tag{2.31}$$

This is also highlighted in Fig. 2.3 where, according to the RF amplitude (red), we have to comply with the phase condition of Eq. (2.31). Hence, two distinct regions of oscillation can again be identified, whether η is positive or negative (above or below transition energy), i.e.:

$$\begin{cases} 0 \le \phi_{s0} < \pi/2 & \text{if } \gamma < \gamma_{\mathrm{tr}} \quad \text{(below transition)},\\ \pi/2 < \phi_{s0} \le \pi & \text{if } \gamma > \gamma_{\mathrm{tr}} \quad \text{(above transition)}. \end{cases} \tag{2.32}$$

Energy of the synchrotron oscillation and RF bucket

In beam stability studies, it is often convenient to introduce the energy of the synchrotron oscillations

$$\mathcal{E} = \frac{\dot{\phi}^2}{2\omega_{s0}^2} + U_{\mathrm{rf}}(\phi)\,, \tag{2.33}$$

where the RF potential well $U_{\mathrm{rf}}(\phi)$ is defined as the phase integral of the voltage $V_{\mathrm{rf}}(\phi)$:

$$U_{\mathrm{rf}}(\phi) = \frac{1}{V_0\cos\phi_{s0}}\int_0^{\phi} V_{\mathrm{rf}}\left(\phi'\right)d\phi'\,. \tag{2.34}$$

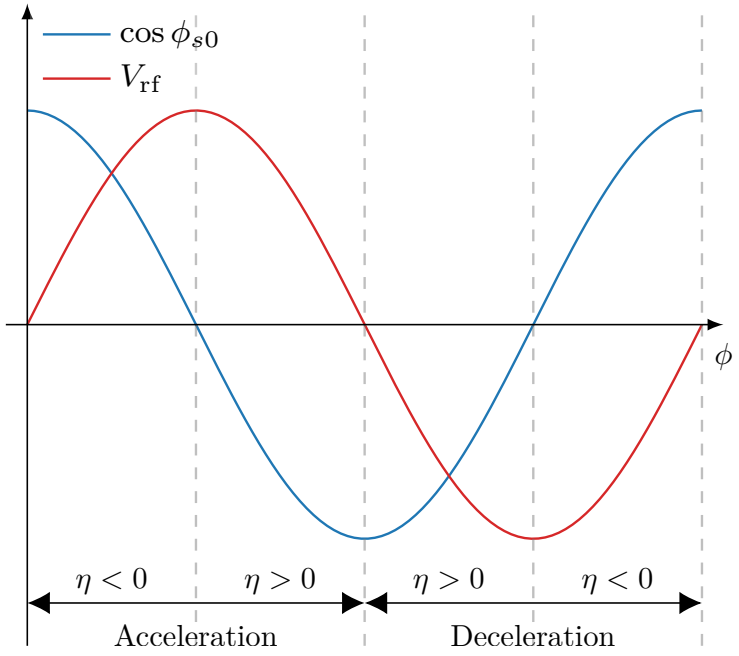

Figure 2.3. Stability condition on the synchronous phase ϕ_{s0} and slip factor η. The voltage generated by a single harmonic RF system is presented in red, while the cosine component of Eq. (2.31) is depicted in blue.

For the case of a single harmonic RF system, the potential well in Eq. (2.34), becomes

$$U_{\mathrm{rf}}(\phi) = -\frac{1}{\cos\phi_{s0}}\left[\cos\left(\phi+\phi_{s0}\right) - \cos\phi_{s0}\right] . \tag{2.35}$$

A particle performs energy-phase oscillations within the potential well around the synchronous phase ϕ_{s0}. Every stable particle trajectory in longitudinal phase-space is associated with a maximum oscillation amplitude $\phi_{\max}$ and constant energy of the synchrotron oscillation $\mathcal{E}_{\max}$.

The equation of the particle phase-space trajectory can be derived through Eq. (2.33), as follows:

$$\frac{\dot{\phi}}{\sqrt{2}\omega_{s0}} = \pm\sqrt{\left[\mathcal{E}_{\max} - U_{\mathrm{rf}}(\phi)\right]} . \tag{2.36}$$

Examples of particle trajectories in the phase space are shown in Fig. 2.4, where the initial condition of $\dot{\phi} = 0$ was imposed (blue dots). Red stars indicate the particle positions in the phase space after 200 revolutions. Due to the non-linearity of the RF system, particles with different phase offsets oscillate around the synchronous phase ϕ_{s0} (red dot) with different angular velocities.

Figure 2.5 illustrates two different potential wells, according to Eq. (2.35). Closed trajectories occur exclusively within the boundaries of the potential well. This means the total energy cannot exceed a specific value; otherwise, the particle will drift away. The maxima of the curve correspond to unstable equilibrium points of the synchrotron motion. The stable phases ϕ_{s0} correspond to the local minima of the curves, while the unstable points are denoted as ϕ_u.

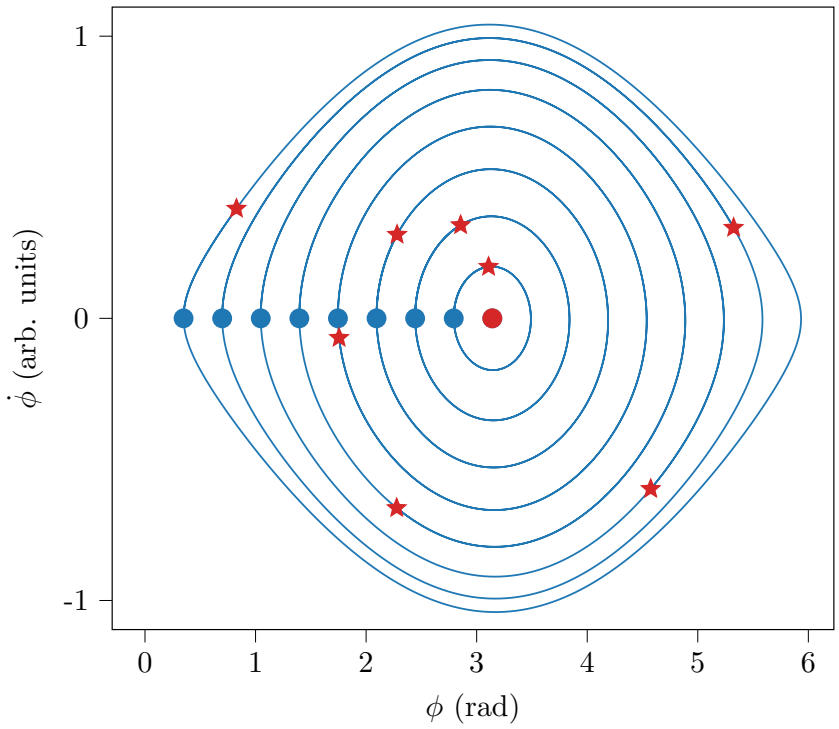

Figure 2.4. Particle trajectories (clockwise) in the phase-space with $\dot{\phi} = 0$ and $\phi \neq \phi_{s0}$ as initial condition (blue dots) in a stationary state above transition energy ($\eta > 0$). The red dot represents the synchronous phase ϕ_{s0} while the stars depict the position in the phase-space after 200 turns.

At the unstable phase ϕ_u, an energy threshold can be defined $\mathcal{E} = \mathcal{E}_{\text{sep}}$, beyond which the particle oscillation is no longer bounded in the potential well. The limiting trajectory in the phase-space traced by $\mathcal{E}_{\text{sep}}$ is called separatrix and marks the separation between distinct domains within which particles are captured (bucket) and accelerated. The energy of the synchrotron oscillation corresponding to the separatrix is expressed as:

$$\mathcal{E}_{\text{sep}} = U(\phi_u) = -\frac{1}{\cos\phi_{s0}} \left[\cos(\phi_u + \phi_{s0}) - \cos\phi_{s0}\right] . \tag{2.37}$$

Combining Eq. (2.33) and Eq. (2.36) allows to calculate the separatrices in the phase-space for a single RF system (Figure 2.6). In particular, Fig. 2.6a depicts the separatrices below transition energy ($\eta < 0$) in steady state (blue) and acceleration for different synchronous phases. While above transition energy, the synchronous phase has to be shifted by π to preserve the stability condition of Eq. (2.31), as shown Fig. 2.6b.

The phase space enclosed by the separatrix is referred to as a bucket. Its area is given by

$$A = \oint_{\text{sep}} \frac{\Delta E(\phi)}{h\omega_0} d\phi = \sqrt{-\frac{V_0 \cos\phi_{s0} q \beta^2 E_0}{\pi \eta \omega_0^2 h^3}} \oint_{\text{sep}} \sqrt{[\mathcal{E}_{\text{sep}} - U_{\text{rf}}(\phi)]} d\phi \,, \tag{2.38}$$

and equivalent to the longitudinal acceptance. In order to avoid particle losses, not

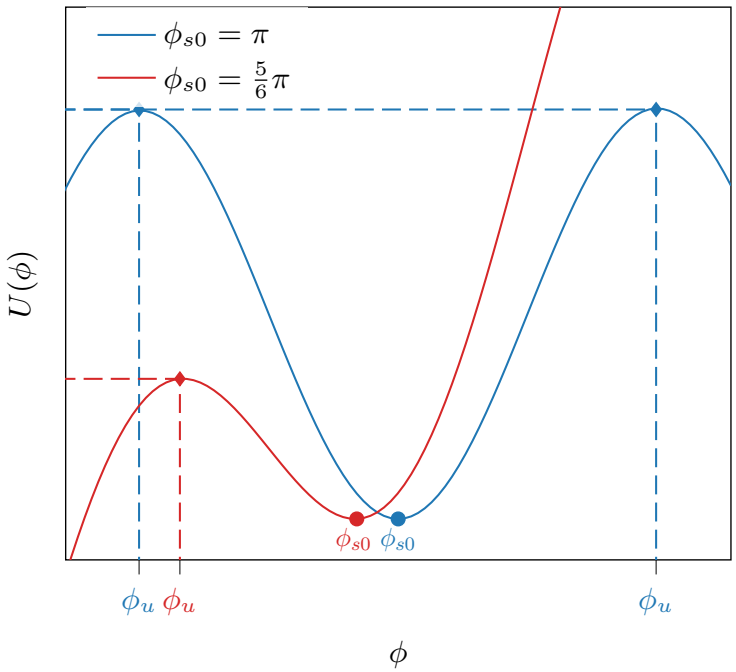

Figure 2.5. RF potential for $\phi_{s0} = \pi$ in blue and $\phi_{s0} = 5/6\pi$ in red above transition energy ($\eta > 0$). The dashed lines indicate the unstable phase location and the related maximum energy.

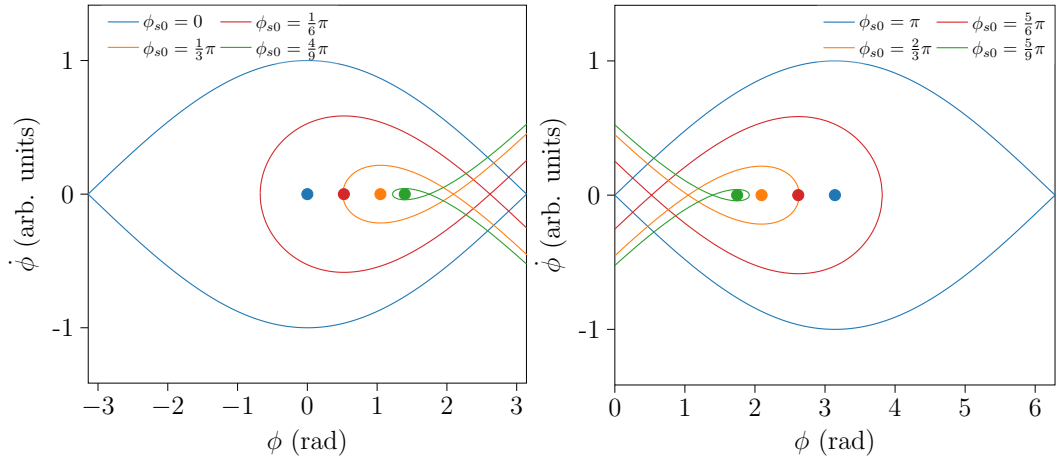

(a) Below transition energy ($\eta < 0$). **(b)** Above transition energy ($\eta > 0$).

Figure 2.6. Separatrices below (left) and above (right) transition energy in a single RF system. Equations (2.33) and (2.36) have been calculated for different synchrotron phases (dots).

the entire stable area is occupied by a beam enclosed by a single particle trajectory in the phase space. The occupied area is denoted as longitudinal single-particle emittance. We define it as:

$$\varepsilon = \oint \frac{\Delta E(\phi)}{h\omega_0} d\phi = \sqrt{-\frac{V_0 \cos\phi_{s0} q \beta^2 E_0}{\pi \eta \omega_0^2 h^3}} \varepsilon_\ell \,. \tag{2.39}$$

The dimensionless longitudinal emittance, ε_ℓ, in Eq. (2.39), is

$$\varepsilon_\ell = 2\int_{\phi_{\min}(\mathcal{E})}^{\phi_{\max}(\mathcal{E})} \sqrt{[\mathcal{E}_{\max} - U_{\rm rf}(\phi)]}d\phi\,, \tag{2.40}$$

where $\phi_{\min}$ is the minimum phase of the particle with energy $\mathcal{E}$.

Synchrotron frequency distribution

We have shown that particles confined in a potential well perform synchrotron oscillations around the synchronous phase ϕ_{s0}. For small amplitude oscillation, the synchrotron frequency is given by Eq. (2.30). However, the RF system amplitude, in Eq. (2.7), is locally linear around ϕ_{s0}. For larger amplitude oscillations, particles exhibit non-linear synchrotron oscillations due to the shape of the RF voltage.

The period of the particle oscillation around the synchronous phase, $T_s(\mathcal{E})$, can be derived from the energy of the synchronous oscillation and the potential, as follows

$$T_s(\mathcal{E}) = \frac{\sqrt{2}}{\omega_{s0}}\int_{\phi_{\min}(\mathcal{E})}^{\phi_{\max}(\mathcal{E})} \frac{d\phi'}{\sqrt{\mathcal{E} - U\left(\phi'\right)}}\,, \tag{2.41}$$

where $\phi_{\min}(\mathcal{E})$ is the minimum phase of the particle with energy of the synchrotron oscillation $\mathcal{E}$ and, together with $\phi_{\max}(\mathcal{E})$, they have to satisfy the relation $\mathcal{E} = U_{\rm rf}(\phi)$. In the stationary case, the potential well is symmetric with respect to the synchronous phase. Hence, replacing the potential of Eq. (2.35) in Eq. (2.41), we obtain:

$$T_s\left(\phi_{\max}\right) = \frac{2}{\omega_{s0}}\int_0^{\phi_{\max}} \frac{d\phi}{\sqrt{\sin^2\left(\phi_{\max}/2\right) - \sin^2(\phi/2)}}\,. \tag{2.42}$$

The integral in Eq. (2.42) can be reduced to the conventional form of the elliptic integral of the first kind

$$K\left[\sin\left(\phi_{\max}/2\right)\right] = \int_0^{\pi/2} \frac{da}{\sqrt{1 - \sin^2\left(\phi_{\max}/2\right)\sin^2 a}}\,, \tag{2.43}$$

with

$$a(\phi) = \arcsin\left[\frac{\sin\left(\phi/2\right)}{\sin\left(\phi_{\max}/2\right)}\right]. \tag{2.44}$$

Eventually, expanding in series the elliptical integral up to the second order, the synchrotron frequency for a particle at maximum phase excursion $\phi_{\max}$ can be approximated to

$$\omega_s(\phi_{\max}) = \omega_{s0}\frac{\pi}{2K[\sin\phi_{\max}/2]} \approx \omega_{s0}\left(1 - \frac{\phi_{\max}^2}{16}\right). \tag{2.45}$$

Figure 2.7 compares the exact solution of Eq.(2.42) and its approximation. While the synchrotron frequency is relatively constant at the central region of the bucket, it decreases for larger amplitudes of synchrotron oscillations. Close to the separatrix, the period diverges to infinity. The synchrotron frequency spread has an impact on longitudinal beam stability. As shown in Appendix. C, it is essential for the fundamental stabilization mechanism of Landau damping.

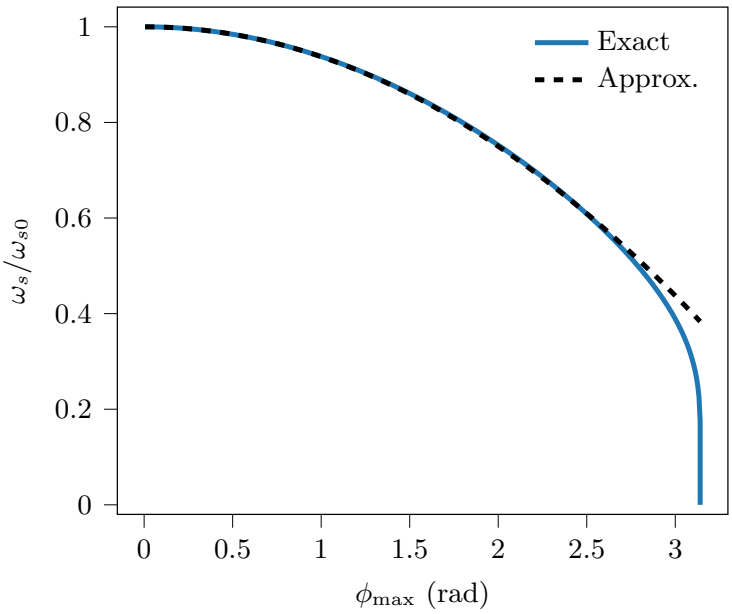

Figure 2.7. Synchrotron frequency in a stationary bucket versus maximum phase excursion $\phi_{\max}$ of the trajectory. The dashed line shows that the approximation according to Eq. (2.45) is valid in a wide range of phase excursions.

2.1.5 Double harmonic RF system

Multi-harmonic RF systems provide the flexibility to control and manipulate longitudinal beam parameters, such as bunch length and bunch spacing. These configurations can be applied in diverse contexts, including mitigating space charge effects or modulating the peak line density in proton and electron synchrotrons [54–56]. This thesis will focus on the double-harmonic RF (DRF) system, the most common multiple RF station configuration, also used in the PSB, PS, and SPS at CERN.

In the case of a DRF, the particles experience a total voltage given by

$$V_{\mathrm{rf}}(\phi) = V_0[\sin(\phi + \phi_{s0}) + r_V \sin\left(r_h\phi + r_h\phi_{s0} + \Phi_2\right)], \tag{2.46}$$

where r_V and r_h are the RF systems voltage and harmonic number ratios, respectively, and Φ_2 represents the relative phase between them. Two main configurations are distinguished according to Φ_2. In the SPS, they are defined such that the high harmonic RF system does not contribute to the acceleration at $\phi = 0$ for the entire cycle. Hence, following the SPS definitions, bunch shortening mode (BSM) occurs at $\Phi_2 = \phi - r_h\phi_{s0}$ while bunch lengthening mode (BLM) for $\Phi_2 = -r_h\phi_{s0}$. In the stationary case, BSM is when both RF systems are in phase at the bunch position; on the contrary, when the RF systems are in counter-phase, the bunch stretches, which reduces the peak longitudinal line density, leading to the BLM. Figure 2.8 illustrates the total voltage at the bunch center in a second-harmonic RF system ($r_h = 2$) according to Eq. (2.46).

In the following subsections, a more comprehensive view regarding the impact of these configurations on the beam is provided.

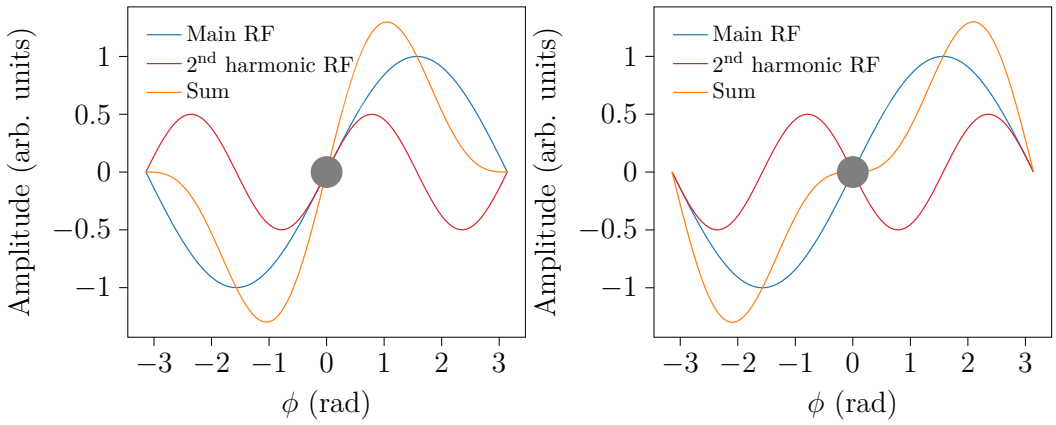

Figure 2.8. Sum of two RF systems (orange) with voltage and harmonic ratio respectively equal to $r_V = 1/2$ and $r_h = 2$. Both RF systems are in phase at the bunch position (BSM, left) with $\Phi_2 = 0$. The RF systems are in counter-phase with $\Phi_2 = \pi$ (BLM, right).

Potential well and equation of motion

Taking into account Eq. (2.46) the potential well $U_{\mathrm{rf}}(\phi)$, in a DRF, assumes the following form:

$$U_{\mathrm{rf}}(\phi) = -\frac{1}{\cos\phi_{s0}}\left\{\cos\left(\phi+\phi_{s0}\right) - \cos\phi_{s0} + \right. \\ \left. + \frac{r_V}{r_h}\left[\cos\left(r_h\phi + r_h\phi_{s0} + \Phi_2\right) - \cos\left(r_h\phi_{s0}+\Phi_2\right)\right]\right\}. \tag{2.47}$$

The equation of motion, in Eq. (2.26), is extended to:

$$\frac{d^2\phi}{dt^2} - \frac{h\eta\omega_0^2 qV_0}{2\pi\beta^2 E_0}\left\{\sin(\phi+\phi_{s0}) + r_V\sin\left[r_h\phi + r_h\phi_{s0} + \Phi_2\right]\right\} = 0\,. \tag{2.48}$$

Figure 2.9 shows the potential well evolution transitioning from the single RF to DRF case. In particular, in BSM the potential well narrows, leading to a shorter bunch. On the contrary, in BLM, the potential well results in a wider minimum and, consequently, longer bunches.

According to the equation of motion of Eq. (2.48), Fig. (2.10) spans different harmonic ratios r_h, with $r_V = 1/r_h$, illustrating the different trajectories (red lines) experienced by the particles in the phase-space. The separatrix of the bucket (black line) changes accordingly by updating Eq. (2.37) with the modified potential well of Eq. (2.47).

Similarly to Sec. 2.1.4, we can again study the particle behavior for small amplitude oscillation by considering $\phi \ll 1$. Thus, in the stationary case, the term in the curly brackets can be simplified as

$$\phi\cos\phi_{s0} + \phi r_V r_h\cos\left(r_h\phi_{s0}+\Phi_2\right). \tag{2.49}$$

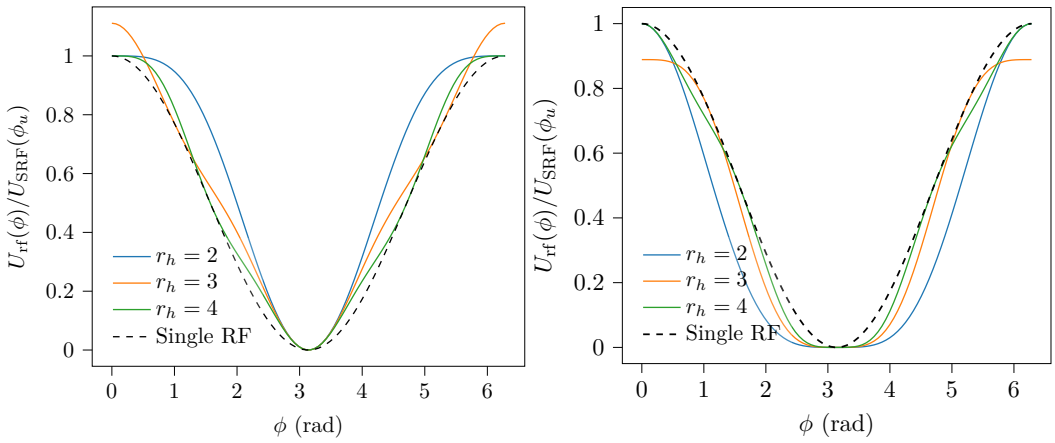

(a) BSM **(b)** BLM

Figure 2.9. Potential well in DRF system normalized by the single RF case computed at the unstable point ϕ_u. Both configurations, i.e., BSM (left) and BLM (right), are compared with the single RF case (black dashed).

Taking into account Eq. (2.30) and using the above approximation, Eq. (2.48) becomes:

$$\frac{d^2\phi}{dt^2} + \phi \frac{\omega_{s0}^2}{\cos\phi_{s0}} \left[\cos\phi_{s0} + r_V r_h \cos\left(r_h\phi_{s0} + \Phi_2\right)\right] = 0\,. \tag{2.50}$$

We recognize the equation characterizing a harmonic oscillator, wherein the angular frequency is equal to:

$$\omega_s = \omega_{s0}\sqrt{1 + r_V r_h \frac{\cos\left(r_h\phi_{s0} + \Phi_2\right)}{\cos\phi_{s0}}}\,. \tag{2.51}$$

Therefore, for small amplitude oscillations, the DRF synchrotron frequency is proportional to the single RF case. Note that in BLM, the synchronous frequency vanishes in the bunch center for the particular case of $r_V = 1/r_h$.

Synchrotron frequency distribution in DRF systems

The particle oscillation period in Eq. (2.41) can be extended for a DRF system case by considering the Eq. (2.47). However, finding a closed solution to the integral can be tedious or not feasible. Nonetheless, in Chapter 3, an approximated solution is derived.

Figure 2.11 shows the exact synchrotron frequency distributions for different values of RF harmonic r_h in both configurations. The DRF system introduces additional nonlinearities, leading to a larger synchronous frequency spread. Increasing this, is generally a desired effect in hadron synchrotrons for suppressing longitudinal instabilities [57].

2.1.6 Relative phase shift

Typically, RF systems can work in a non-ideal configuration due to imperfect calibration, phase shifts due to the beam, etc. Therefore, if the RF cavities are not

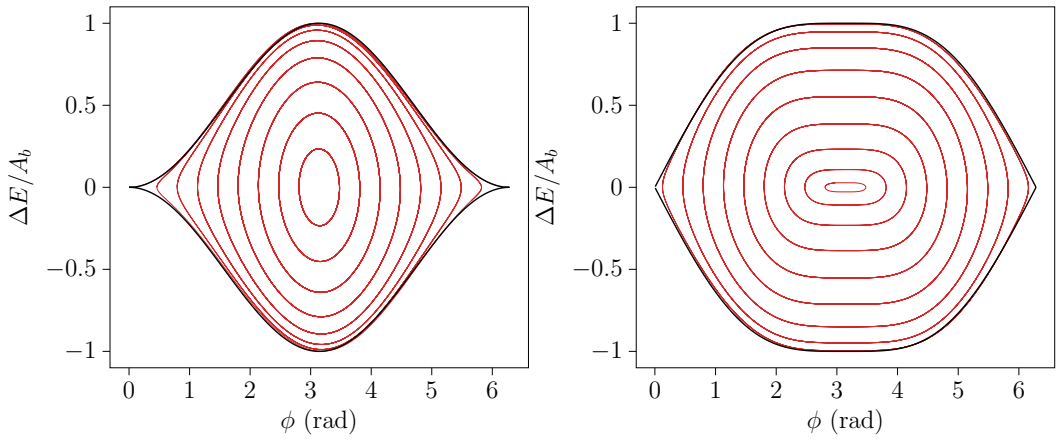

(a) BSM with $r_h = 2$; $r_V = 0.5$.

(b) BLM with $r_h = 2$; $r_V = 0.5$.

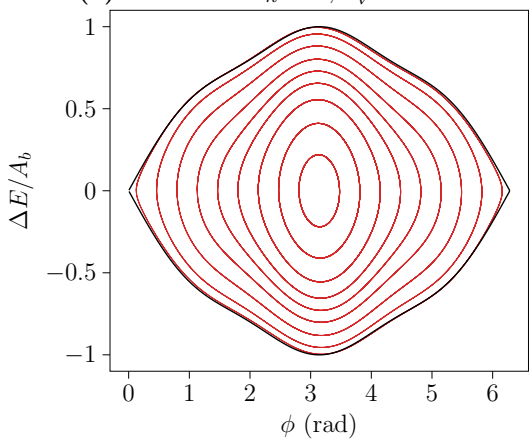

(c) BSM with $r_h = 3$; $r_V = 0.33$.

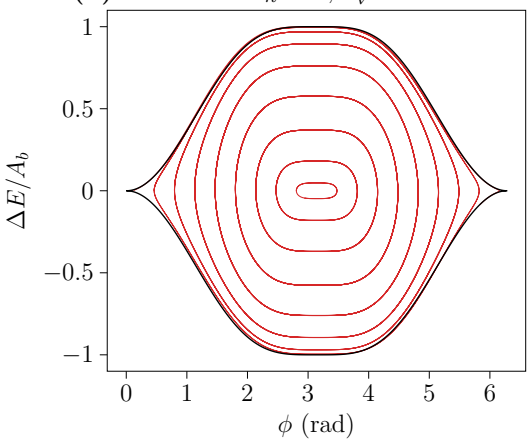

(d) BLM with $r_h = 3$; $r_V = 0.33$.

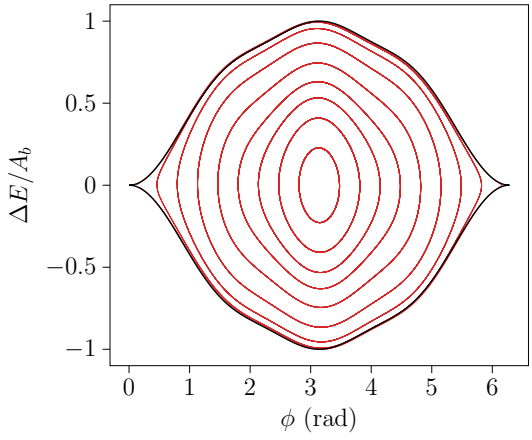

(e) BSM with $r_h = 4$; $r_V = 0.25$.

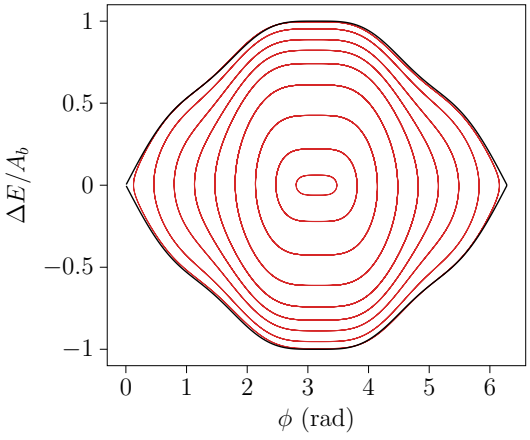

(f) BLM with $r_h = 4$; $r_V = 0.25$.

Figure 2.10. RF bucket (black) in BSM (left) and BLM (right), in the stationary state, for different harmonic ratios normalized by their maximum bunch area A_b. The red curves show the individual particle trajectories in the phase-space for constant energy of the synchrotron oscillation, while the separatrix (black) marks the region of closed trajectories.

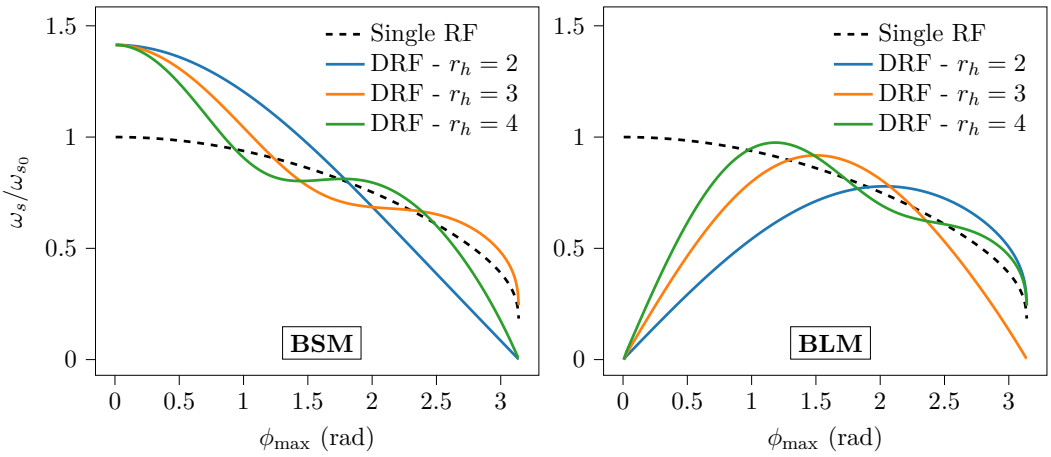

Figure 2.11. Synchrotron frequency distribution for different harmonics r_h, normalized to the small-amplitude synchrotron frequency in single RF. Both operating modes (BSM left, BLM right) are compared as a function of the maximum phase deviation of the particle with $r_{_V} = 1/r_h$. The curves are compared with the conventional single RF system case (black dashed line).

perfectly aligned in phase (or in counter phase), the synchronous phase of the DRF system no longer coincides with the phase of the single RF, ϕ_{s0}. This causes a loss of symmetry in the total potential and, consequently, in the line density of the bunch. The phase shift of the synchrotron phase can be deduced from Eq. (2.48), where deriving the equation of motion in ϕ_{s0} leads to

$$\sin\phi_{s0} = \sin\phi_s + r_{_V}\sin\left(r_h\phi_s + \Phi_2\right). \tag{2.52}$$

The transcendental equation (2.52) is numerically solved for ϕ_s and analyzed as a function of the relative phase Φ_2. The synchronous phase deviation for the example of a fourth harmonic RF system, with respect to the relative phase for various RF voltage ratios, is shown in Fig. 2.12 (left). The zero crossing points (red) designate ideal BSM or BLM conditions. It becomes clear that the BSM is more robust to the relative phase error, allowing a wider range of Φ_2 for a small synchronous phase deviation. On the contrary, in BLM, even slight variations in Φ_2 lead to significant changes in the synchronous phase. This represents a strong limitation for operating in the BLM since achieving this accuracy can be challenging. Similar results can be achieved for other harmonic number ratios, r_h. A consequence of the synchronous phase shift is the small amplitude synchrotron frequency deviation, Δf_s. From Eq. (2.51), taking into account the new synchronous phase ϕ_s, satisfying Eq. (2.52), we obtain

$$f_s(0) = f_{s0}\sqrt{\frac{\cos\phi_s + r_{_V} r_h\cos\left(r_h\phi_s + \Phi_2\right)}{\cos\phi_{s0}}}\,. \tag{2.53}$$

This is also confirmed by Fig. 2.12 (right) which shows that the synchrotron frequency in BSM is less sensitive with respect to the BLM. For the latter, small variations of the relative phase lead to an important synchrotron frequency deviation.

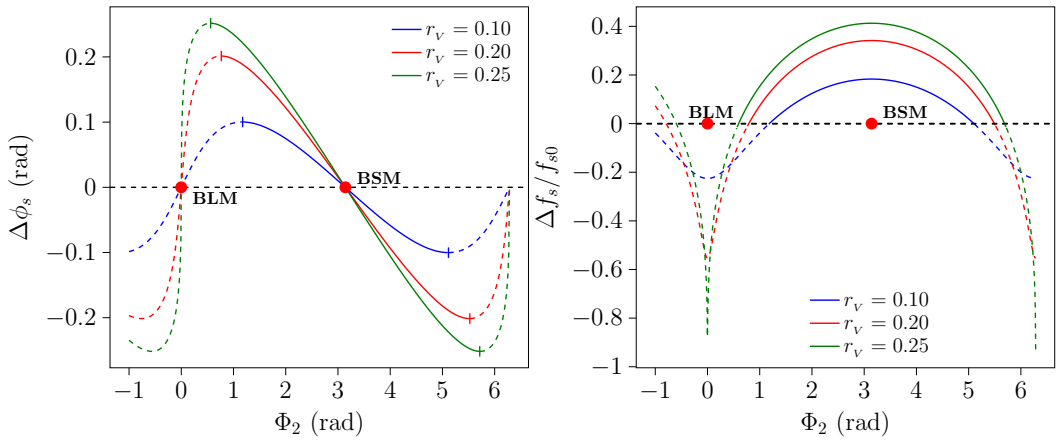

Figure 2.12. Synchronous phase (left) and small amplitude synchronous frequency deviation (right) as a function of the relative phase. Different voltage ratios r_V and $r_h = 4$ have been considered. The red dots indicate the respective working points of ideal BSM and BLM.

2.1.7 Wakefields and beam-coupling impedance

Until now, the prevailing assumption has been that the trajectory of particles is exclusively determined by the externally applied voltage from the RF system. This assumption neglected any collective effects. However, the particles interact with the surroundings (such as RF cavities, kickers, beam monitoring devices, etc.), thereby giving rise to electromagnetic fields [50, 58]. These fields reciprocally influence the beam, inducing deviations in the particle motion. In most high-energy accelerators, since the particles travel close to the speed of light, the electromagnetic waves are generally left behind, leading to the connotation of wake fields.

Let us consider a charged particle q traveling close to the speed of light in a structure with discontinuity, such as a cavity. An electromagnetic field is generated in the wake of the particle as soon as it crosses the discontinuity, as illustrated in Fig. 2.13. A witness particle (red dot), at a distance Δz will experience a force due to the electromagnetic field generated by the particle source (green).

The longitudinal wake function is defined as the induced voltage per unit charge experienced by the trailing particle and is given by

$$\mathcal{W}(\Delta z) = \frac{1}{q}\int_L \mathscr{E}_z(z+\Delta z, t)dz\,, \tag{2.54}$$

where $\mathscr{E}_z$ is the longitudinal component of the wakefield and L the length of the corresponding element. The dimensions of the wake function in the time domain are (V/C). Often, it is more convenient to study Eq. (2.54) in the frequency domain. Thus, applying the Fourier transform over one period of the RF frequncy $\phi/\omega_{\mathrm{rf}}$, yields:

$$Z(\omega) = \int_{-\infty}^{\infty} \mathcal{W}(\phi) e^{-i\omega\phi/\omega_{\mathrm{rf}}} \frac{d\phi}{\omega_{\mathrm{rf}}}\,, \tag{2.55}$$

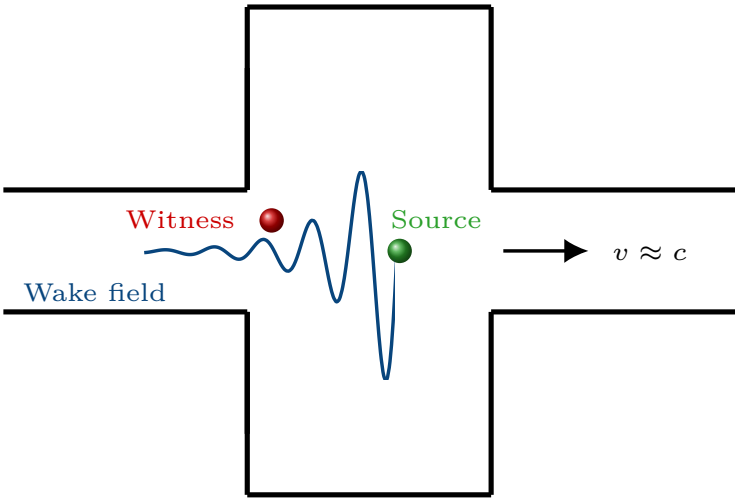

Figure 2.13. Schematic of a wakefield generated by a particle influencing a trailing particle. The source particle is represented in green, while the witness particle, at a distance Δz in red, both traveling close to the speed of light.

and with the corresponding inverse Fourier transform, one obtains:

$$\mathcal{W}(\phi) = \frac{1}{2\pi} \int_{-\infty}^{\infty} Z(\omega) e^{i\omega\phi/\omega_{\mathrm{rf}}} d\omega \,. \tag{2.56}$$

Due to the time integration, the dimension of Eq. (2.55) is as an impedance in Ohm. The function is called longitudinal beam coupling impedance and relates the beam current to the total induced voltage along the beam trajectory.

Based on how long the wake fields persist, they can be divided into two main categories: short-range wakefield, which concerns mainly a single bunch, and long-range wakefield, which couples bunches and is hence a multi-bunch or multi-turn effect. The short-range primarily arises from local interactions such as space charge[5] or inductive wall impedances [51]. In the ultra-relativistic case, space charge can be neglected since the electric field generated by each particle is perpendicular to its motion [58]. In most accelerators, the walls have inductive impedance at low and medium frequencies, and the space charge acts like a capacitive impedance. Thus, the space charge and inductive impedance effects on the bunch can be partly or entirely compensated.

The next section presents the multi-particle case with special attention to the binomial particle distribution, highlighting the basic concepts of beam instability due to intensity effects and coherent motion.

2.2 Multi-particle motion and beam stability

In the context of the analysis of beam instabilities, moving to another set of conjugate variables, namely $\mathcal{E}$ and ψ, is convenient. They correspond, respectively, to the

[5]The beam is composed of particles having identical charge, resulting in a repulsive force between them.

energy and phase of the synchrotron oscillations. Thus, one obtains:

$$\begin{aligned} \mathcal{E} &= \frac{\dot{\phi}^2}{2\omega_{s0}^2} + U_t(\phi)\,, \\ \psi &= \operatorname{sgn}(\eta\Delta E)\frac{\omega_s(\mathcal{E})}{\sqrt{2}\omega_{s0}}\int_{\phi_{\max}}^{\phi}\frac{d\phi'}{\sqrt{\mathcal{E}-U_t\left(\phi'\right)}}\,, \end{aligned} \tag{2.57}$$

where the total potential $U_t(\phi)$, similarly to Eq. (2.34), is defined by the total voltage $V_t(\phi)$, i.e.,

$$U_t(\phi) = \frac{1}{V_0\cos\phi_{s0}}\int_{\Delta\phi_s}^{\phi}\left[V_t(\phi') - V_0\sin\phi_{s0}\right]d\phi'\,. \tag{2.58}$$

The total voltage includes the additional voltage contribution $V_{\mathrm{ind}}(\phi)$ due to intensity effects, namely $V_t(\phi) = V_{\mathrm{rf}}(\phi) + V_{\mathrm{ind}}(\phi)$. Furthermore, the synchronous phase shift, $\Delta\phi_s$, in Eq. (2.58) due to intensity effects has to satisfy the following relation:

$$V_0\sin\phi_{s0} = V_0\sin\left(\phi_{s0}+\Delta\phi_s\right) + V_{\mathrm{ind}}(\Delta\phi_s)\,. \tag{2.59}$$

In the new coordinates, the stationary distribution function $\mathcal{F}$ is a function of only the energy $\mathcal{E}$ with the line density

$$\lambda(\phi) = 2\omega_{s0}\int_{U_t(\phi)}^{\mathcal{E}_{\max}}\frac{\mathcal{F}(\mathcal{E})}{\sqrt{2\left[\mathcal{E}-U_t(\phi)\right]}}d\mathcal{E}\,, \tag{2.60}$$

in which the normalization

$$\int_{-\pi h}^{\pi h}\lambda(\phi)d\phi = 1\,, \tag{2.61}$$

is imposed. Hereafter, binomial particle distributions are considered. They cover most of the realistic longitudinal bunch distributions in proton synchrotrons (from flat bunches, i.e., $\mu = -1/2$, to Gaussian shape for $\mu \to \infty$).

$$\mathcal{F}(\mathcal{E}) = \frac{1}{2\pi\omega_{s0}A_N}\left(1-\frac{\mathcal{E}}{\mathcal{E}_{\max}}\right)^{\mu} = \frac{g(\mathcal{E})}{2\pi\omega_{s0}A_N}\,. \tag{2.62}$$

Furthermore, the normalization factor A_N in Eq. (2.62), is defined as

$$A_N = \omega_{s0}\int_0^{\mathcal{E}_{\max}}\frac{g(\mathcal{E})}{\omega_s(\mathcal{E})}d\mathcal{E}\,. \tag{2.63}$$

Under these assumptions, the integral in Eq. (2.60) can be computed analytically, leading to

$$\lambda(\phi) = \frac{\sqrt{\mathcal{E}_{\max}}\Gamma(\mu+1)}{\sqrt{2\pi}A_N\Gamma(\mu+3/2)}\left[1-\frac{U_t(\phi)}{\mathcal{E}_{\max}}\right]^{\mu+1/2}\,, \tag{2.64}$$

where Γ is the gamma function. For finite μ, the corresponding full bunch length can be derived as:

$$\tau_{\mathrm{full}} \;=\; \left[\phi_{\max}\left(\mathcal{E}_{\max}\right) - \phi_{\min}\left(\mathcal{E}_{\max}\right)\right]/\omega_{\mathrm{rf}}\,. \tag{2.65}$$

2.2.1 Induced voltage

As the beam intensity increases, the particles within the beam cannot be considered as non-interacting single particles anymore, and collective effects become important. We define a voltage acting on the witness charge at position Δz, induced by all the other charges, as in Fig. 2.13. This voltage depends on the longitudinal bunch distribution, in Eq. (2.60), according to [51]:

$$V_{\mathrm{ind}}(\phi) = -qN_p \sum_{k=0}^{\infty} \int_{-\pi h}^{\pi h} \lambda(\varphi)\mathcal{W}(\phi - \varphi + 2\pi hk)d\varphi\,, \tag{2.66}$$

where k is the harmonic of the revolution frequency. Equation (2.66) contains the contribution of the current turn ($k = 0$) and the past turns for $k > 0$. The offset sum of $2\pi hk$ keeps track of the wakefield evolution over time.

For the causality principle, the negative sum limit can be extended to $k = -\infty$. Thus, using Eq. (2.56), one gets

$$V_{\mathrm{ind}}(\phi) = -qN_p \int_{-\pi h}^{\pi h} \lambda(\varphi)d\varphi \int_{-\infty}^{\infty} Z(\omega)e^{i\omega(\phi-\varphi)/\omega_{\mathrm{rf}}} \sum_{k=-\infty}^{\infty} e^{i2\pi k\omega/\omega_0} \frac{d\omega}{2\pi}\,. \tag{2.67}$$

The last term of Eq. (2.67) represents the Fourier expansion of periodic pulses, namely

$$\sum_{k=-\infty}^{\infty} e^{i2\pi k\omega/\omega_0} = \omega_0 \sum_{k=-\infty}^{\infty} \delta(\omega - k\omega_0)\,. \tag{2.68}$$

Eventually, substituting, the induced voltage can be expressed as:

$$V_{\mathrm{ind}}(\phi) = -qN_p h\omega_0 \sum_{k=-\infty}^{\infty} Z_k\lambda_k e^{ik\phi/h} = \sum_{k=-\infty}^{\infty} V_k e^{ik\phi/h}\,, \tag{2.69}$$

where $Z_k = Z(k\omega_0)$ and the harmonic of the line density is equal to

$$\lambda_k = \frac{1}{2\pi h} \int_{-\pi h}^{h\pi} \lambda(\phi)e^{-ik\phi/h}d\phi\,. \tag{2.70}$$

The harmonic expansion of a time-dependent induced voltage is also possible in an analogous way (see Appendix B for the full derivation). It will become relevant for treating perturbations in the beam stability study.

2.2.2 Vlasov equation for beam instability studies

The most common approach in studying beam stability is to analyze the evolution of a distribution function $\mathcal{F}$. In order to include collective effects in the analysis, the perturbations $\tilde{\mathcal{F}}$,$\tilde{\lambda}$ and $\tilde{V}_{\mathrm{ind}}$ must be taken into account. Respectively, they represent the perturbations of the equilibrium distribution function, line density, and induced voltage.

The time evolution of the distribution function is described by Liouville's theorem [59]. It affirms that the phase-space distribution function is constant along the

trajectories of the system and can be expressed by the Vlasov equation [46]. Therefore, assuming the new coordinates system $(\mathcal{E}, \psi)$, the linearized Vlasov equation[6] can be expressed as

$$\frac{\partial \tilde{\mathcal{F}}}{\partial t} + \frac{d\mathcal{E}}{dt}\frac{d\mathcal{F}}{d\mathcal{E}} + \frac{d\psi}{dt}\frac{\partial \tilde{\mathcal{F}}}{\partial \psi} = 0\,, \tag{2.71}$$

where, by definition, $d\psi/dt = \omega_s(\mathcal{E})$.

In the presence of perturbations, the equation of motion Eq. (2.26) becomes

$$\frac{d\dot{\phi}}{dt} + \frac{\omega_{s0}^2}{V_0 \cos\phi_{s0}}\left[V_t(\phi) - V_0 \sin\phi_{s0}\right] = -\frac{\omega_{s0}^2}{V_0 \cos\phi_{s0}}\tilde{V}_{\text{ind}}\,(\phi, t)\,, \tag{2.72}$$

where the voltage in the system has been replaced with the total voltage $V_t(\phi) = V_{\text{rf}}(\phi) + V_{\text{ind}}(\phi)$. Multiplying both sides for $\dot{\phi}$ and considering the first relation in Eq. (2.57) yields

$$\frac{d\mathcal{E}}{dt} = -\frac{d\phi}{dt}\frac{\tilde{V}_{\text{ind}}(\phi, t)}{V_0 \cos\phi_{s0}} = -\omega_s(\mathcal{E})\frac{\partial \tilde{U}_{\text{ind}}(\phi, t)}{\partial \psi}\,. \tag{2.73}$$

The perturbed potential well is defined as:

$$\tilde{U}_{\text{ind}}\,(\phi) = \frac{1}{V_0 \cos\phi_{s0}}\int_{\Delta\phi_s}^{\phi} \tilde{V}_{\text{ind}}\;(\phi')\,d\phi'\,, \tag{2.74}$$

with the assumption that the synchronous phase shift $\Delta\phi_s$, due to intensity effects, must fulfill the relation $V_0 \sin(\phi_{s0}) = V_{\text{rf}}(\Delta\phi_s) + V_{\text{ind}}(\Delta\phi_s)$. Eventually, the linearized Vlasov equation can then be written in the following compact way, i.e.:

$$\left[\frac{\partial}{\partial t} + \omega_s\frac{\partial}{\partial \psi}\right]\tilde{\mathcal{F}} = \omega_s\frac{\partial \tilde{U}_{\text{ind}}}{\partial \psi}\frac{d\mathcal{F}}{d\mathcal{E}}\,. \tag{2.75}$$

Given a stationary distribution $\mathcal{F}(\mathcal{E})$ with wake function $\mathcal{W}(\phi)$, the solutions of Eq. (2.75) determine the stability of the system. Several approaches allow finding accurate solutions of the Vlasov equation without neglecting the synchrotron frequency spread [35, 41, 44, 61].

In the further sections, we will focus on two complementary approaches, namely the Lebedev equation [35] and the Oide-Yokoya method [44], to solve Eq. (2.75), which will serve as a baseline for the analysis performed in this thesis.

2.2.3 Lebedev equation

Lebedev proposed the first self-consistent system of equations suitable for the eigenvalue analysis of longitudinal beam stability [35]. Following [45, 62], we derive the Lebedev equation in his original matrix form.

Since the solution of Eq. (2.75) has to be periodic, it can be represented as a sum of the harmonics $e^{-im\psi}$ (with $m \neq 0$). Hence, assuming Ω as the frequency of the perturbation such us $\tilde{\mathcal{F}}(\mathcal{E}, \psi, t) = \tilde{\mathcal{F}}(\mathcal{E}, \psi, \Omega)e^{i\Omega t}$ and $\tilde{U}_{\text{ind}}(\mathcal{E}, \psi, t) = \tilde{U}_{\text{ind}}(\mathcal{E}, \psi, \Omega)e^{i\Omega t}$, we have:

[6] Since we are dealing with perturbations, the Vlasov equation can be simplified with a linearization. However, in general, the Vlasov equation is not linear [60].

$$\begin{aligned}\tilde{\mathcal{F}}(\mathcal{E},\psi,\Omega) &= \sum_{m=-\infty}^{\infty} \tilde{\mathcal{F}}_m(\mathcal{E},\Omega)e^{-im\psi}\,,\\ \tilde{U}_{\mathrm{ind}}(\mathcal{E},\psi,\Omega) &= \sum_{m=-\infty}^{\infty} \tilde{U}_{\mathrm{ind},m}(\mathcal{E},\Omega)e^{-im\psi}\,,\end{aligned} \tag{2.76}$$

where the respective Fourier components are:

$$\begin{aligned}\tilde{\mathcal{F}}_m(\mathcal{E},\Omega) &= \frac{1}{2\pi}\int_{-\pi}^{\pi} \tilde{\mathcal{F}}(\mathcal{E},\psi,\Omega)e^{im\psi}d\psi\,,\\ \tilde{U}_{\mathrm{ind},m}(\mathcal{E},\Omega) &= \frac{1}{2\pi}\int_{-\pi}^{\pi} \tilde{U}_{\mathrm{ind}}(\mathcal{E},\psi,\Omega)e^{im\psi}d\psi\,.\end{aligned} \tag{2.77}$$

The solution of the Vlasov equation is found substituting the Fourier expansion of Eq. (2.76) in Eq. (2.75). Respectively, each term is equal to

$$\begin{aligned}\frac{\partial}{\partial t}\tilde{\mathcal{F}}(\mathcal{E},\psi,\Omega) &= i\Omega \sum_{m=-\infty}^{\infty} \tilde{\mathcal{F}}_m(\mathcal{E},\Omega)e^{-im\psi}e^{i\Omega t}\,,\\ \frac{\partial}{\partial \psi}\tilde{\mathcal{F}}(\mathcal{E},\psi,\Omega) &= -im \sum_{m=-\infty}^{\infty} \tilde{\mathcal{F}}_m(\mathcal{E},\Omega)e^{-im\psi}e^{i\Omega t}\,,\\ \frac{\partial}{\partial \psi}\tilde{U}_{\mathrm{ind}}(\mathcal{E},\psi,\Omega) &= -im \sum_{m=-\infty}^{\infty} \tilde{U}_{\mathrm{ind},m}(\mathcal{E},\Omega)e^{-im\psi}e^{i\Omega t}\,.\end{aligned} \tag{2.78}$$

Therefore, using Eq. (2.78), the solution of the Vlasov equation (2.75) becomes:

$$\tilde{\mathcal{F}}(\mathcal{E},\psi,\Omega) = -\omega_s(\mathcal{E})\frac{d\mathcal{F}}{d\mathcal{E}} \sum_{m=-\infty}^{\infty} \frac{m\tilde{U}_{\mathrm{ind},m}(\mathcal{E},\Omega)}{\Omega - m\omega_s(\mathcal{E})}e^{-im\psi}\,. \tag{2.79}$$

The perturbed induced voltage is related to the perturbed line density and, similarly to Eq. (2.69), is equal to (see Appendix B)

$$\tilde{V}_k(\Omega) = -qN_p h\omega_0 Z_k(\Omega)\tilde{\lambda}(\Omega)\,, \tag{2.80}$$

where the impedance must be periodic in a ring suchs as $Z_k(\Omega) = Z(k\omega_0 + \Omega)$.

We define, for convenience, the intensity parameter as

$$\zeta \triangleq \frac{qN_p h^2\omega_0}{V_0}\,, \tag{2.81}$$

which is proportional to the number of particles, N_p, and the harmonic number, h, squared. Applying Eq. (2.74), we can link the induced potential well of the perturbation to the perturbed harmonic of the induced voltage, as follows:

$$\tilde{U}_{\mathrm{ind}}(\mathcal{E},\psi,\Omega) = -i\zeta \sum_{k=-\infty}^{\infty} Z_k(\Omega)/k\tilde{\lambda}_k(\Omega)(e^{i\phi k/h} - e^{i\Delta\phi_s k/h})\,. \tag{2.82}$$

According to Eq. (2.77), the Fourier harmonics $\tilde{U}_{\mathrm{ind},m}(\mathcal{E})$ is then:

$$\tilde{U}_{\mathrm{ind},m}(\mathcal{E},\Omega) = -i\zeta \sum_{k=-\infty}^{\infty} Z_k(\Omega)/k\tilde{\lambda}_k(\Omega)I_{mk}(\mathcal{E})\,, \tag{2.83}$$

where the function I_{mk}, was initially introduced for the first time in [35], and is equal to

$$I_{mk}(\mathcal{E}) = \frac{1}{2\pi}\int_{-\pi}^{\pi} e^{i\phi(\mathcal{E},\psi)k/h+im\psi}d\psi = \frac{1}{\pi}\int_{0}^{\pi} e^{i\phi(\mathcal{E},\psi)k/h}\cos(m\psi)d\psi\,. \tag{2.84}$$

Note that $\phi(\mathcal{E},\psi)$ must be an even function with respect to the phase of the synchrotron oscillation. In addition, since $\phi(\mathcal{E},\psi)$ is linked to the potential well distortion, Eq. (2.84) takes into account also intensity effects and has the following properties:

$$I_{-mk} = I_{mk} \quad \text{and} \quad I_{m-k} = I^*_{mk}\,. \tag{2.85}$$

where is I^*_{mk} is the complex conjugate of the function I_{mk}. For a symmetric potential well, we also have $I^*_{mk} = (-1)^m I_{mk}$,

As far as the perturbation line density is concerned, for a perturbation frequency Ω, one can write

$$\tilde{\lambda}(\phi,\Omega) = \sum_{k=-\infty}^{\infty}\tilde{\lambda}_k(\Omega)e^{i\phi k/h}\,. \tag{2.86}$$

Assuming the transformation of variables $d\phi d\dot{\phi} = \omega_{s0}^2 d\psi d\mathcal{E}/\omega_s(\mathcal{E})$, the harmonic $\tilde{\lambda}_k(\Omega)$ are related to the perturbation of the distribution function according to

$$\tilde{\lambda}_k(\Omega) = \frac{1}{2\pi h}\int_{-\pi h}^{\pi h}\tilde{\lambda}(\phi)e^{-i\phi k/h}d\phi = \frac{\omega_{s0}^2}{2\pi h}\int_{-\pi}^{\pi}d\psi\int_{0}^{\mathcal{E}_{\max}}\frac{\tilde{\mathcal{F}}(\mathcal{E},\psi,\Omega)}{\omega_s(\mathcal{E})}e^{-i\phi(\mathcal{E},\psi)k/h}d\mathcal{E}\,. \tag{2.87}$$

Eventually, substituting Eq. (2.79) into Eq. (2.87), leads to the Lebedev equation [35], i.e.:

$$\tilde{\lambda}_p(\Omega) = -\frac{\zeta}{h}\sum_{k=-\infty}^{\infty}G_{p,k}(\Omega)Z_k(\Omega)/k\tilde{\lambda}_k(\Omega)\,. \tag{2.88}$$

It represents an infinite set of equations for harmonics of the line density perturbation, $\tilde{\lambda}$, at frequency Ω. Note that it depends on the intensity through the parameter ζ. The beam transfer matrices, $G_{pk}(\Omega)$ [57] in Eq. (2.88), are defined as

$$G_{pk}(\Omega) = -2i\omega_{s0}^2\sum_{m=1}^{\infty}\int_{0}^{\mathcal{E}_{\max}}\frac{d\mathcal{F}(\mathcal{E})}{d\mathcal{E}}\frac{I^*_{mk}(\mathcal{E})I_{mp}(\mathcal{E})\omega_s(\mathcal{E})}{\Omega^2/m^2-\omega_s^2(\mathcal{E})}d\mathcal{E}\,. \tag{2.89}$$

Replacing the distribution function, $\mathcal{F}(\mathcal{E})$, with the binomial distribution in Eq. (2.62), yields:

$$G_{pk}(\Omega) = -i\frac{\omega_{s0}}{\pi A_N}\sum_{m=1}^{\infty}\int_{0}^{\mathcal{E}_{\max}}\frac{dg(\mathcal{E})}{d\mathcal{E}}\frac{I^*_{mk}(\mathcal{E})I_{mp}(\mathcal{E})\omega_s(\mathcal{E})}{\Omega^2/m^2-\omega_s^2(\mathcal{E})}d\mathcal{E}\,. \tag{2.90}$$

For the Lebedev equation, to admit a non-trivial solution, the determinant to the associated matrix with the system of Eq. (2.88) must be zero. Hence

$$D(\Omega,\zeta) = \det\left|\delta_{pk}+\frac{\zeta}{h}G_{pk}(\Omega)Z_k(\Omega)/k\right| = 0\,, \tag{2.91}$$

where δ_{pk} represents the Kronecker's delta. The solution of the above determinant depends on the intensity, ζ, and specific frequencies Ω.

2.2.4 Oide-Yokoya equation

A complementary approach was proposed by K. Oide and K. Yokoya [41] and employed already for beam stability studies as in [26, 45, 63] allows to derive the bunch modes including the synchrotron frequency spread. In particular, following the Oide-Yokoya method, the perturbed density function may be expanded in a Fourier [64] series as

$$\tilde{\mathcal{F}}(\mathcal{E},\psi,t) = \tilde{\mathcal{F}}(\mathcal{E},\psi,\Omega)e^{i\Omega t} = e^{i\Omega t}\sum_{m=1}^{\infty}\left[C_m(\mathcal{E},\Omega)\cos m\psi + S_m(\mathcal{E},\Omega)\sin m\psi\right] . \tag{2.92}$$

Inserting the series in Eq. (2.92) into the linearized Vlasov equation (2.75), yields [65]

$$\begin{aligned} i\Omega C_m(\mathcal{E},\Omega) + m\omega_s(\mathcal{E})S_m(\mathcal{E},\Omega) &= \frac{m\omega_s(\mathcal{E})}{\pi}\frac{d\mathcal{F}}{d\mathcal{E}}\int_{-\pi}^{\pi}\tilde{U}_{\mathrm{ind}}(\mathcal{E},\psi,\Omega)\sin(m\psi) = 0\,, \\ -m\omega_s(\mathcal{E})C_m(\mathcal{E},\Omega) + i\Omega S_m(\mathcal{E},\Omega) &= -\frac{m\omega_s(\mathcal{E})}{\pi}\frac{d\mathcal{F}}{d\mathcal{E}}\int_{-\pi}^{\pi}\tilde{U}_{\mathrm{ind}}(\mathcal{E},\psi,\Omega)\cos(m\psi) = \\ &= 2i\zeta m\omega_s(\mathcal{E})\frac{d\mathcal{F}}{d\mathcal{E}}\sum_{k=-\infty}^{\infty}Z_k(\Omega)/k\tilde{\lambda}_k(\Omega)I^*_{mk}(\mathcal{E})\,. \end{aligned} \tag{2.93}$$

Furthermore, we can derive the harmonic of the perturbed line density using the expanded distribution of Eq. (2.92) into Eq. (2.87), obtaining:

$$\tilde{\lambda}_k(\Omega) = \frac{\omega_{s0}^2}{h}\sum_{m=1}^{\infty}\int_0^{\mathcal{E}_{\max}}\frac{C_m(\mathcal{E},\Omega)I_{mk}(\mathcal{E})}{\omega_s(\mathcal{E})}\,. \tag{2.94}$$

Eventually, combining Eq. (2.93) with the above, one gets

$$\begin{aligned} [\Omega^2 - m^2\omega_s^2(\mathcal{E})]C_m(\mathcal{E},\Omega) &= 2i\zeta\omega_{s0}^2m^2\omega_s^2(\mathcal{E})\frac{d\mathcal{F}(\mathcal{E})}{d\mathcal{E}} \\ &\times\sum_{m'=1}^{\infty}\int_0^{\mathcal{E}_{\max}}\sum_{k=-\infty}^{\infty}\frac{d\mathcal{E}'}{\omega_s(\mathcal{E}')}\frac{Z_k(\Omega)/k}{hZ_0}I^*_{mk}(\mathcal{E})I_{m'k}(\mathcal{E}')C_{m'}(\mathcal{E}',\Omega)\,. \end{aligned} \tag{2.95}$$

The integral function in Eq. (2.95) can be addressed by reducing it in an eigenvalue problem of linear algebra. In Chapter 4, we will solve this integral function with a semi-analytical code using the Oide-Yokoya discretization [44].

2.3 Van Kampen modes

The first concept of Van Kampen modes was introduced in plasma physics, where an eigensystem of the Vlasov equation was found in an infinite plasma showing a spectrum composed of continuous and discrete parts [42, 43]. The continuous spectrum is delineated by singular functions underscoring the relation with single particle motion, while the discrete one may not necessarily exist.

In the context of beam dynamics, the concept of van Kampen modes can be introduced to describe bunch oscillations in the longitudinal plane [41]. In particular,

it has been shown that at low intensity (i.e., $\zeta \approx 0$), the complete set of van Kampen modes is encompassed within the continuous spectrum ($\Omega = m\omega_s(\mathcal{E})$). In this case, Landau damping results from the decoherence of these modes, which do not represent the collective dynamic but rather the single-particle motions. Once Landau damping is lost for higher intensity, the discrete van Kampen modes emerge from the incoherent band lying outside $\omega_s(\mathcal{E})$.

The concept of van Kampen modes is already well-consolidated in beam dynamics spanning from analyzing power wake [44], capacitive [66] and inductive impedance [67] to instabilities and LLD threshold studies [26, 63].

In the next chapters, the thresholds for the LLD will be derived in a DRF system, similarly to the single RF in Ref. [45], by applying the concept of van Kampen modes to solve the Lebedev equation (2.88) in its original matrix form. These results are then compared with the findings obtained using the Oide-Yokoya method [Eq. (4.7)] and macroparticle simulations, as well as beam measurement.

Chapter 3

Analytical criteria for longitudinal loss of Landau damping in double harmonic RF systems

As introduced in the previous chapters, Landau damping plays a key role in the framework of coherent beam instabilities. This chapter analyzes the LLD in the DRF system for different combinations of $\eta \mathrm{ImZ}/k$ and relative phase Φ_2. For each scenario, the corresponding LLD threshold condition will be provided.

More recent research exploited the emerged van Kampen mode criterion to determine the LLD thresholds in a single RF system [45]. Contrary to these previous studies, it has been observed that for a particle distribution belonging to the binomial family, the presence of a pure inductive impedance above the transition energy (or a capacitive impedance below it) results in a vanishing LLD threshold unless an upper cutoff to the impedance is introduced. Moreover, both analytical and numerical studies have shown that the LLD threshold becomes inversely proportional to the cutoff frequency f_c when $f_c \gg 1/\tau_{\mathrm{full}}$ (τ_{full} represents the full bunch length).

A similar study is conducted in the double-harmonic RF systems, above transition energy, with both cavities in phase at the bunch position (BSM) [68]. In this configuration, an analytical approximation of the synchrotron frequency distribution is calculated as a function of the synchrotron oscillation energy. An analytical expression for the LLD threshold is then derived using the Lebedev equation. The results obtained with this equation will be compared in Chapter 5 with thresholds obtained using the Oide-Yokoya method and subsequently tested with macroparticle tracking simulations and measurements.

3.1 Main scenarios according to the beam energy regimes, impedance, and RF configuration

In the longitudinal plane, LLD occurs when the coherent mode moves out of the incoherent synchrotron frequency band. Let us consider, for example, a bunch in a

single RF system with maximum phase deviation of the particle $\phi_{\max}$, corresponding to a full bunch length of $\tau_{\text{full}} = 2\phi_{\max}/\omega_{\text{rf}}$. The corresponding synchrotron frequency, without acceleration and collective effects, is illustrated in Fig. 3.1. The incoherent band is defined by $f_{\min}$ and $f_{\max}$, and the synchrotron frequency spread coincides with the height of the grey zone (red arrows). Therefore, the Landau damping is lost when a coherent mode lies outside the grey zone.

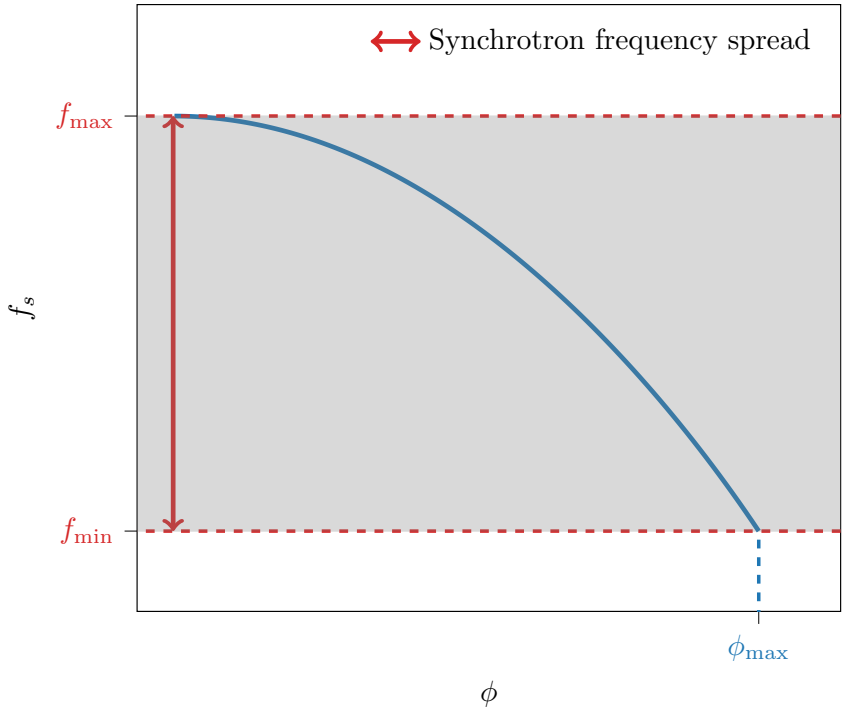

Figure 3.1. Example of synchrotron frequency distribution (blue) in single RF for a bunch with maximum phase deviation of the particle $\phi_{\max}$. The minimum and maximum of the synchrotron frequency distribution are depicted in red dashed lines, while the synchrotron frequency spread is depicted with arrows. No acceleration and collective effects are considered in this illustration.

According to the combinations of $\eta \text{ImZ}/k$ and relative phase between RF systems, the modes can emerge below ($f_{\min}$) or above ($f_{\max}$) the incoherent band. For a constant inductive impedance ($\text{Im}Z/k > 0$), two distinct regimes can be identified based on whether $\eta \text{ImZ}/k$ is positive or negative, resulting in a total of four cases depending on the selected RF configuration. Table 3.1 summarizes the scenarios where, for completeness, the capacitive impedance case has also been considered. Figure 3.2 shows the van Kampen mode (red) coming out of the incoherent synchrotron frequency band (grey) for $\text{Im}Z/k > 0$ (left) and $\text{Im}Z/k > 0$ (right) leading to the LLD. The van Kampen mode, representing the undamped particle oscillation mode, emerges from $f_{\max}$ (left) or $f_{\min}$ (right), as specified in Tab. 3.1.

For convenience, hereafter, we will refer to a purely inductive impedance. The corresponding case for capacitive impedance is equivalently obtained by changing the sign of η.

Table 3.1. The LLD threshold definition according to the possible combinations of $\eta \mathrm{Im}Z/k$.

Inductive impedance $\mathrm{Im}Z/k > 0$		
	BSM	BLM
Above transition $\eta > 0$	$\Omega = \max[\omega_s(\mathcal{E})]$	$\Omega = \max[\omega_s(\mathcal{E})]$
Below transition $\eta < 0$	$\Omega = \min[\omega_s(\mathcal{E})]$	$\Omega = \min[\omega_s(\mathcal{E})]$

Capacitive impedance $\mathrm{Im}Z/k < 0$		
	BSM	BLM
Above transition $\eta > 0$	$\Omega = \min[\omega_s(\mathcal{E})]$	$\Omega = \min[\omega_s(\mathcal{E})]$
Below transition $\eta < 0$	$\Omega = \max[\omega_s(\mathcal{E})]$	$\Omega = \max[\omega_s(\mathcal{E})]$

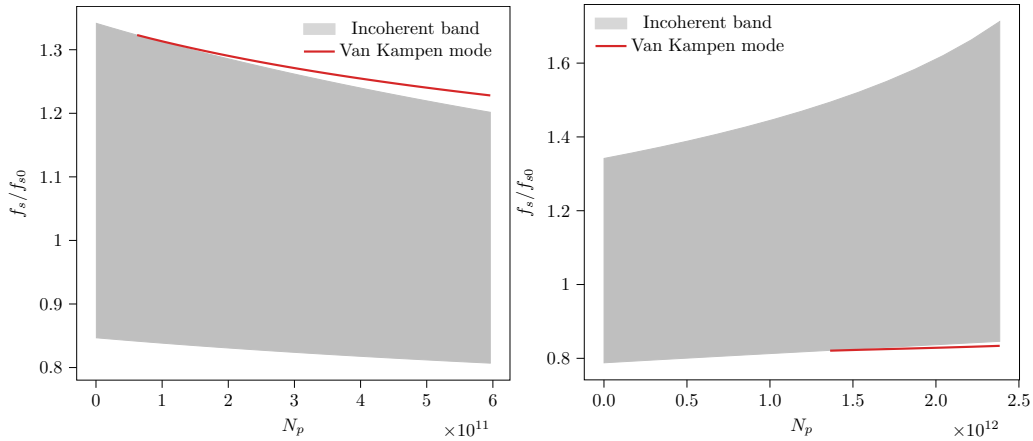

Figure 3.2. Examples of incoherent synchrotron frequency band (grey) as a function of the intensity for $\eta \mathrm{Im}Z/k > 0$ (left) and $\eta \mathrm{Im}Z/k < 0$ (right). The emerged van Kampen mode (red) represents the undamped oscillation mode.

3.2 Analytical equation of the synchrotron frequency distribution in BSM

The synchrotron frequency distribution can generally be derived from the synchrotron oscillation period in Eq. (2.41). However, finding an exact closed solution is not trivial, and numerical solutions are often calculated instead.

Below, we calculate in the DRF system an analytical estimate for the synchrotron frequency distribution [69]. This will allow us to derive an equation of the LLD threshold in BSM above transition energy without neglecting the synchrotron frequency spread. In this configuration (i.e., $\phi_s = \Phi_2$), the energy of the synchrotron oscillation in Eq. (2.57), computed for the maximum particle phase deviation $\phi_{\max}$, is

$$\mathcal{E}(\phi_{\max}) = 2\sin^2\left(\frac{\phi_{\max}}{2}\right) + 2\frac{r_V}{r_h}\sin^2\left(\frac{r_h\phi_{\max}}{2}\right). \tag{3.1}$$

In the small amplitude approximation $\phi_{\max} \ll 1$, it simplifies as

$$\mathcal{E}(\phi_{\max}) = (1 + r_V r_h)\frac{\phi_{\max}^2}{2}. \tag{3.2}$$

In BSM, the integral equation of the synchrotron oscillation period in Eq. (2.41) assumes the form:

$$T_s = \frac{2}{\omega_{s0}} \int_0^{\phi_{\max}} \frac{d\phi}{\sqrt{\sin^2\left(\frac{\phi_{\max}}{2}\right) - \sin^2\left(\frac{\phi}{2}\right) + \frac{r_V}{r_h}\left[\sin^2\left(r_h\frac{\phi_{\max}}{2}\right) - \sin^2\left(r_h\frac{\phi}{2}\right)\right]}}\,. \tag{3.3}$$

Since we are interested in small bunches, we expand in series Eq. (3.3) up to the fourth order. This leads to:

$$T_s = \frac{8}{\omega_{s0}}\sqrt{\frac{3}{1+r_V r_h}} \int_0^{\phi_{\max}} \frac{d\phi}{a\phi_{\max}\sqrt{\left(1-\phi^2/\phi_{\max}^2\right)\left(1-\phi^2/a^2\right)}}\,, \tag{3.4}$$

where the parameter a comprises the RF parameters and is equal to:

$$a^2 = \frac{12(1+r_V r_h)}{1+r_V r_h^3} - \phi_{\max}^2\,. \tag{3.5}$$

Furthermore, considering $x^2 = \phi^2/\phi_{\max}^2$ and $A^2 = \phi_{\max}^2/a^2$ and substituting into Eq. (3.4), the integral equation can be reduced to the conventional elliptic integral of the first kind

$$K(\phi_{\max}/a) = \frac{1}{a}\int_0^1 \frac{dx}{\sqrt{(1-x^2)(1-A^2x^2)}}\,. \tag{3.6}$$

Given that $\omega_s = 2\pi/T_s$, the synchrotron frequency distribution is equal to:

$$\frac{\omega_s(\phi)}{\omega_{s0}} = \frac{\pi}{4}\sqrt{\frac{1+r_V r_h^3}{3}}\frac{a}{K(\phi_{\max}/a)}\,. \tag{3.7}$$

Eventually, for $\phi_{\max}/a \ll 1$ we can approximate further and obtain the following closed form

$$\frac{\omega_s(\phi)}{\omega_{s0}} \approx \sqrt{1+r_V r_h}\left(1 - \frac{1+r_V r_h^3}{1+r_V r_h}\frac{\phi_{\max}^2}{16}\right)\,. \tag{3.8}$$

Figure 3.3 displays the comparison between the synchrotron frequency distribution found by solving numerically Eq. (2.41) (solid lines) and the Eq. (3.8) (dashed lines). As expected, for short bunches, the equation matches very well with the exact solution, and it diverges when the condition $\phi_{\max}/a \ll 1$ is no longer valid.

For convenience, let us rewrite the equation as a function of synchrotron oscillation energy, $\mathcal{E}$. This form will be applied in the next section. Hence, combining Eqs. (3.2) and (3.8), we obtain:

$$\frac{\omega_s(\mathcal{E})}{\omega_{s0}} \approx \sqrt{1+r_h r_V}\left(1 - \frac{1+r_V r_h^3}{(1+r_V r_h)^2}\frac{\mathcal{E}}{8}\right)\,. \tag{3.9}$$

3.3 The LLD threshold equation for a pure inductive impedance

We derive an analytical expression of the LLD threshold in BSM by solving the Lebedev equation (2.88) for $\mathrm{Im}Z/k = \text{const}$ above transition energy (or capacitive below). A similar procedure is adopted as for the single RF system case in [45].

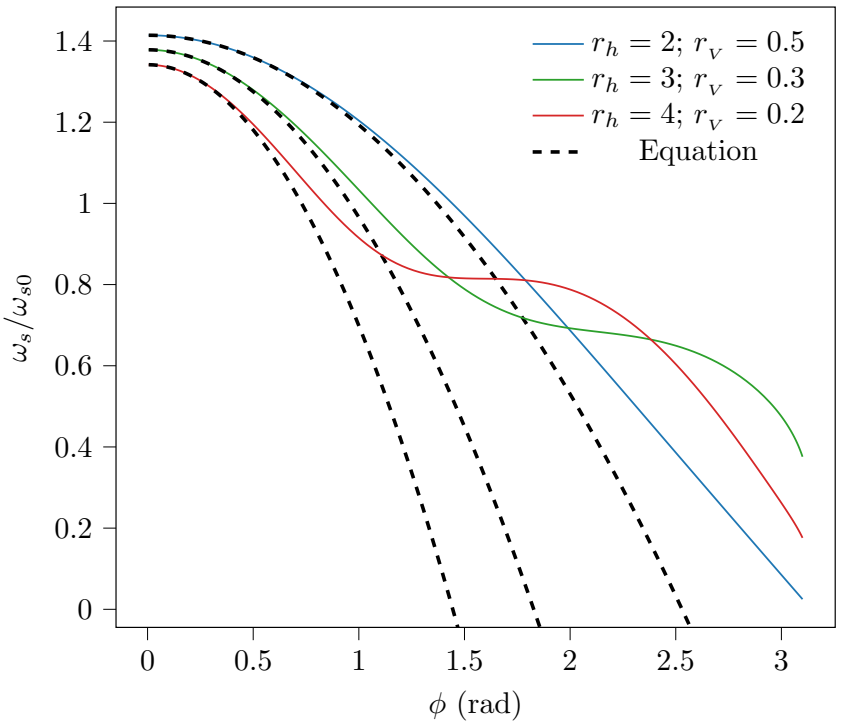

Figure 3.3. Comparison between Eq. (3.8) and synchrotron frequency distributions by solving numerically (solid lines) the Eq. (2.41). No acceleration and collective effects have been considered.

Let us consider the fundamental azimuthal mode $m = 1$ (dipole mode). At low intensities, the synchrotron frequency distribution in BSM is a monotonic function of the energy of synchrotron oscillations, $\mathcal{E}$. Assuming that this still holds at the LLD threshold for a dipole mode, we can determine at what intensity ζ_{th} the coherent mode frequency Ω equals the maximum incoherent frequency. This means solving Eq. (2.91) to derive when $\Omega = \max\left[\omega_s(\mathcal{E})\right] = \omega_s(0)$. The determinant of a square matrix can be expanded in series using the following square matrix properties, i.e.:

$$\det(I + \epsilon X) = 1 + \text{tr}(X)\epsilon + O\left(\epsilon^2\right), \tag{3.10}$$

where I is the identity matrix and $\text{tr}(X)$ is the trace of an arbitrary matrix X; while $O\left(\epsilon^2\right)$ refers to the upper bound of the expansion according to the big O notation. The truncation at the first order is justified when the parameter ϵ is sufficiently small ($\epsilon \ll 1$). Hence, assuming Eq. (3.10), the Eq.(2.91) leads to the general LLD threshold equation:

$$\zeta_{\text{th}} = -h\left[\sum_{k=-\infty}^{\infty} G_{kk}(\Omega)Z_k(\Omega)/k\right]^{-1}, \tag{3.11}$$

where ϵ is proportional to the intensity parameter, ζ.

For low energy oscillation, $\phi(\mathcal{E}, \psi) \approx \sqrt{2\mathcal{E}/(1 + r_V r_h)}\cos\psi$. In this approxima-

tion, the function I_{mk} in Eq. (2.84) becomes:

$$I_{mk} \approx \int_{-\pi}^{\pi} e^{ik/h\sqrt{2\mathcal{E}/(1+r_V r_h)}\cos\psi - im\psi} d\psi \,. \tag{3.12}$$

This allows us to simplify the I_{mk} into a Bessel function of the first kind[1]

$$I_{mk} \approx i^m J_m\left(\frac{k}{h}\sqrt{\frac{2\mathcal{E}}{1+r_V r_h}}\right) . \tag{3.14}$$

Based on Eq. (3.9), the LLD occurs when $\Omega = \omega_{s0}\sqrt{1+r_V r_h}$. We can calculate the matrice G_{kk} in Eq. (2.90), keeping only the first element of the sum over the azimuthal modes ($m = 1$) and including the approximate I_{mk} from Eq. (3.14). This yields

$$\begin{aligned} G_{kk} = &- \frac{8i(1+r_V r_h^3)}{\pi A_N \phi_{\max}^2} \int_0^1 \frac{dg(x)}{dx} J_1^2\left(\frac{kx}{h}\phi_{\max}\right) \\ &\times \frac{(1+r_V r_h)/(1+r_V r_h^3) - \phi_{\max}^2 x^2/16}{x^2(1+r_V r_h)/(1+r_V r_h^3) - \phi_{\max}^2 x^4/32} dx \,. \end{aligned} \tag{3.15}$$

Note that a change of variable has been performed by imposing $x = \sqrt{\mathcal{E}/\mathcal{E}_{\max}}$; moreover, the maximum phase amplitude is defined as $\phi_{\max} = \sqrt{2\mathcal{E}_{\max}/(1+r_V r_h)}$. Combining Eqs. (2.63) and (2.62), we can determine the normalization factor for a binomial distribution by neglecting the synchrotron frequency spread, i.e.:

$$A_N = \frac{\sqrt{1+r_V r_h}\ \phi_{\max}^2}{2(\mu+1)} \,. \tag{3.16}$$

Thus, substituting, the Eq. (3.15) becomes:

$$G_{kk} \approx i\frac{16\mu(\mu+1)(1+r_V r_h^3)}{\pi\phi_{\max}^4(1+r_V r_h)^{1/2}}\left[1 - {}_1F_2\left(\frac{1}{2}; 2, \mu; -y^2\right)\right] , \tag{3.17}$$

where ${}_pF_q\left(a_1, \ldots, a_p; b_1, \ldots, b_q; z\right)$ is the generalized hypergeometric function and $y = k\phi_{\max}/h$. Note that, in Eq. (3.17), for particular values of μ, the expression in the square brackets may be expanded as a combination of Bessel functions of the first kind (e.g., $\mu = 1$ yields $G_{kk} \propto [1 - J_0^2(y) - J_1^2(y)]$). Furthermore, since $G_{kk} \propto \phi_{\max}^4$, the small parameter ϵ, in Eq. (3.10), is defined as

$$\epsilon = \frac{\zeta}{\phi_{\max}^4}\mathrm{Im}Z/k \,. \tag{3.18}$$

Equation (3.11) is evaluated analytically by approximating the sum as an integral. Thus, for a pure inductive impedance, $\mathrm{Im}Z/k$, we obtain:

$$\frac{1}{h}\sum_{k=-\infty}^{\infty} G_{kk}(\Omega)Z_k(\Omega)/k \approx \frac{i}{h}\mathrm{Im}Z/k\int_{-\infty}^{\infty} G_{kk}(\Omega)dk \to \infty \,, \tag{3.19}$$

[1]The general Bessel function in its integral form is:

$$J_n(x) = \frac{1}{2\pi}\int_{-\pi}^{\pi} e^{i(n\tau - x\sin\tau)}d\tau. \tag{3.13}$$

which diverges for $\mu > 0$. For finite threshold, a truncation of the sum at an arbitrary $k_{\max}$ must be taken into account, yielding to the final expression

$$\zeta_{\text{th}} \approx \frac{1 + r_{_V} r_h^3}{\left(1 + r_{_V} r_h\right)^{1/2}} \frac{\pi \phi_{\max}^5}{32\mu(\mu+1)\chi\left(k_{\max}\phi_{\max}/h, \mu\right) \text{Im}Z/k} \,, \tag{3.20}$$

where the function $\chi\left(y, \mu\right)$, is related to the generalized hypergeometric function [70], according to

$$\chi(y, \mu) = y \left[1 - {}_2F_3\left(\frac{1}{2}, \frac{1}{2}; \frac{3}{2}, 2, \mu; -y^2\right)\right] . \tag{3.21}$$

Equation (3.20) shows the significant impact of the order r_h of the harmonic RF system on the LLD threshold, as well as its dependency on the voltage ratio, $r_{_V}$. Note that when the voltage ratio is equal to $r_{_V} = 0$, the equation, as expected, reduces to the simplest case of single RF [45]. Furthermore, in the limit case of $y \to \infty$, the generalized hypergeometric function converges to zero which simplifies Eq. (3.20) to the following form:

$$\zeta_{\text{th}} \approx \frac{1 + r_{_V} r_h^3}{\left(1 + r_{_V} r_h\right)^{1/2}} \frac{\pi \phi_{\max}^4 h}{32\mu(\mu+1)k_{\max}\text{Im}Z/k} \,. \tag{3.22}$$

Equation (3.22) highlights the dependency of the threshold on the fourth power of the bunch length. Furthermore, it is inversely proportional to the cutoff frequency.

In Chapter 5, the closed analytical threshold will be compared with results of semi-analytical calculation with the code MELODY and macroparticle tracking simulations in BLonD.

3.4 Upper limit intensity due to potential well distortion: analytical equation

The induced voltage acts as an additional focusing force when $\eta \text{Im}Z < 0$ or a defocusing force when $\eta \text{Im}Z > 0$, resulting in the narrowing or enlarging of the bucket. For a binomial distribution (2.62), we derive the maximum intensity ζ_{cc} before the collapse of the buckets occurs.

The steady-state potential in Eq. (4.3) can be written in an implicit form, as [37]

$$U_t(\phi) = U_{\text{rf}}(\phi) + \zeta \text{Im}Z/k \left[\lambda(\phi) - \lambda_0\right] \,, \tag{3.23}$$

where $\lambda(\phi)$ and λ_0 are the binomial line density and its normalization factor from Eq. (2.64). Note that the total potential, computed at the maximum particle phase deviation, coincides with the maximum synchrotron oscillation energy in the bunch, namely $U_t(\phi_{\max}) = \mathcal{E}_{\max}$. Therefore, assuming a binomial distribution with $\mu = 0.5$, since $\lambda(\phi_{\max}) = \lambda_0$, we can simplify

$$U_{\text{rf}}(\phi_{\max}) = \mathcal{E}_{\max} + \zeta \text{Im}Z/k\lambda_0 \,. \tag{3.24}$$

Substituting Eq. (3.24) into Eq. (3.23), the total potential can then be expressed as

$$U_t(\phi) = U_{\text{rf}}(\phi) \frac{\mathcal{E}_{\max}}{U_{\text{rf}}(\phi_{\max})} \,. \tag{3.25}$$

The total potential well is directly proportional to the RF potential. To solve Eq. (3.24), we need to find the normalization factor of the binomial line density, $\lambda(\phi)$. Thus, inserting Eq. (3.25) into Eq. (2.64), we can integrate over the maximum phase to obtain λ_0 as

$$\lambda_0 = \frac{1}{\int_{-\phi_{\max}}^{\phi_{\max}} \left[1 - \frac{U_{\mathrm{rf}}(\phi)}{U_{\mathrm{rf}}(\phi_{\max})}\right] d\phi}. \tag{3.26}$$

Eventually, combining Eqs. (3.26) and (3.24), yields

$$\zeta_{\mathrm{cc}} = \frac{1}{\mathrm{Im}Z/k} \left[U_{\mathrm{rf}}(\phi_{\max}) - \mathcal{E}_{\max}\right] \int_{-\phi_{\max}}^{\phi_{\max}} \left[1 - \frac{U_{\mathrm{rf}}(\phi)}{U_{\mathrm{rf}}(\phi_{\max})}\right] d\phi\,. \tag{3.27}$$

Equation (3.27) represents the critical intensity parameter for which the additional contribution of the induced voltage on the total voltage leads the bucket to collapse. Note that Eq. (3.27) holds for an RF potential generated by an arbitrary RF voltage, regardless of whether it is below or above the transition energy.

In Chapter 5, Eq. (3.27) will be benchmarked with the semi-analytical code MELODY. Furthermore, we will show that for inductive impedance below transition energy (or capacitive above), this critical condition often occurs before the LLD threshold.

3.5 Conclusion

An intuitive explanation for the LLD threshold has been given for the simple case of a single RF system. Subsequently, extending to the double harmonic RF case, all the possible combinations of $\eta \mathrm{Im}Z/k$ have been presented, giving for each scenario the respective LLD threshold definition. A refined analytical estimate for the synchrotron frequency distribution in the DRF has been derived. This allowed deriving the LLD threshold from the Lebedev equation for the common case of BSM for a constant inductive impedance above transition energy or, equivalently, capacitive impedance below.

Similarly to the single RF system case, the proposed threshold equation depends on the fourth power of the bunch length. In addition, it is inversely proportional to the cutoff frequency of the impedance. In the limit case of voltage ratio $r_V = 0$, the equation converges to the single RF case [45], as expected.

The additional focusing force due to beam-induced voltage distorts the potential well, ultimately collapsing the bucket. The limit intensity for a binomial particle distribution, with binomial parameter $\mu = 0.5$, was calculated analytically.

Chapter 4

Semi-analytical and numerical approaches for beam stability studies

This chapter presents the primary computational tools utilized within the context of this study. Specifically, it describes the underlying concepts of the MELODY and BLonD codes and the fundamental principles on which these simulation tools are founded. In particular, the two complementary semi-analytical approaches implemented in MELODY, the Lebedev equation and the Oide-Yokoya method, are shown and benchmarked. Thereafter, the macroparticles tracking simulation code BLonD is presented, illustrating the main differences compared to conventional Vlasov solvers and highlighting the main features employed for the beam stability study in the thesis. Finally, both codes are tested and compared.

4.1 Matrix Equations for LOngitudinal beam DYnamics

Matrix Equations for LOngitudinal beam DYnamics (MELODY) [47] is a semi-analytical framework for evaluating longitudinal beam stability by solving the linearized Vlasov equation (see Sec. 2.2.2). It has been developed since 2020 at CERN, and it has already successfully guided the findings of several scientific contributions in the field of longitudinal beam stability [45, 68, 71–73].

The code incorporates two approaches to solve the linearized Vlasov equation (2.75), namely the Lebedev equation (Sec 2.2.3) and the Oide-Yokoya method (Sec. 2.2.4). In both cases, the first problem to address is to find a stationary solution for the total potential $U_t(\phi) = U_{\mathrm{rf}}(\phi) + U_{\mathrm{ind}}(\phi)$. Similarly to Eq. (2.58), the beam-induced potential can be expressed as

$$U_{\mathrm{ind}}\left(\phi\right) = \frac{1}{V_0 \cos\phi_{s0}} \int_{\Delta\phi_s}^{\phi} V_{\mathrm{ind}}\left(\phi'\right) d\phi' \,. \tag{4.1}$$

Equation (4.1) can be written more explicitly as a function of the harmonics of the line density λ_k. Therefore, by taking into account Eq. (2.69), the induced potential

is

$$U_{\text{ind}}\left(\phi\right) = \frac{iqN_p h^2 \omega_0}{V_0 \cos\phi_{s0}} \sum_{k=-\infty}^{\infty} \frac{Z_k}{k} \lambda_k \left(e^{i\frac{k}{h}\phi} - e^{i\frac{k}{h}\Delta\phi_s} \right) . \tag{4.2}$$

To determine a steady-state solution, addressing the distortion of the potential well is necessary. As seen in Eq. (4.2), the induced potential depends on the harmonic components of the line density. Given a step n, the solution for the stationary potential is obtained using an iterative procedure [26]. We compute the total potential in the initial case of $U_{t,0}$ (step $n = 0$) and the line density λ_0 through Eq. (2.64) excluding intensity effects with $N_p = 0$ and $\Delta\phi_s = 0$. Thus, $U_{t,0}$ is equal to the RF potential ($U_{t,0} = U_{\text{rf}}$). The corresponding line density, λ_0, is then used to compute the induced potential and included in the next interaction when computing $U_{t,1}$. The procedure is repeated until it converges to a stationary solution. Therefore, the iterative algorithm for the stationary potential can be summarized as follows:

$$\begin{aligned} U_{t,n} &= (1-\epsilon) U_{t,n-1} + \epsilon U_t\left(\lambda_{n-1}\right); \\ U_{t,n} &= U_{t,n} - \min\left(U_{t,n}\right); \\ \lambda_n &= \lambda\left(U_{t,n}\right); n = 1, 2, \ldots . \end{aligned} \tag{4.3}$$

If it exists, the Eq. (4.3) converges to a stationary solution for an arbitrary ϵ such that $0 < \epsilon < 1$.

4.1.1 Direct solution of the Lebedev equation

The derivation of the Lebedev equation has been shown in Chapter 2. Once the total potential has been obtained, we compute the energy of the synchrotron oscillation, $\mathcal{E}$, from the first equation of motion Eq. (2.57). Subsequently, the beam transfer matrices $G_{pk}(\Omega)$ of Eq. (2.90) can be computed.

The method of calculation utilizing the Lebedev equation (2.91) is based on finding the determinant $D(\Omega, \zeta)$ of the associated matrix with Eq. (2.88). For the linear algebra, a non-trivial solution exists only if the determinant $D(\Omega, \zeta) = 0$. In the MELODY code, a bisection method is implemented, which requires setting an interval $[\zeta_{\text{down}}, \zeta_{\text{up}}]$ where the threshold is expected. A midpoint of the intervals $\zeta' = \left(\zeta_{\text{up}} - \zeta_{\text{down}}\right)/2$ is used to calculate $D(\Omega, \zeta')$. The new interval is then narrowed depending on whether the determinant is positive or negative (e.g., $D(\Omega, \zeta') > 0$; $\zeta_{\text{up}} = \zeta'$). The iteration continues until the error function, e_{bis}, defined as

$$e_{\text{bis}} = \frac{\zeta_{\text{up}} - \zeta_{\text{down}}}{\zeta_{\text{up}} + \zeta_{\text{down}}} , \tag{4.4}$$

is lower than an arbitrary threshold error, e_{th}. This iterative process is illustrated in Fig. 4.1, where the numbers indicate the iteration step. The example considers the BSM with harmonic ratio $r_h = 2$ and voltage ratio $r_V = 0.5$ with RF and accelerator parameters outlined in Tab. 4.1 (Sec. 4.1).

4.1.2 Oide-Yokoya discretization

In order to solve Eq. (2.95), MELODY performs a discretization on the functions $C_m(\mathcal{E}, \omega)$, introduced in the Fourier expansion in Eq. (2.94). In the original work [44],

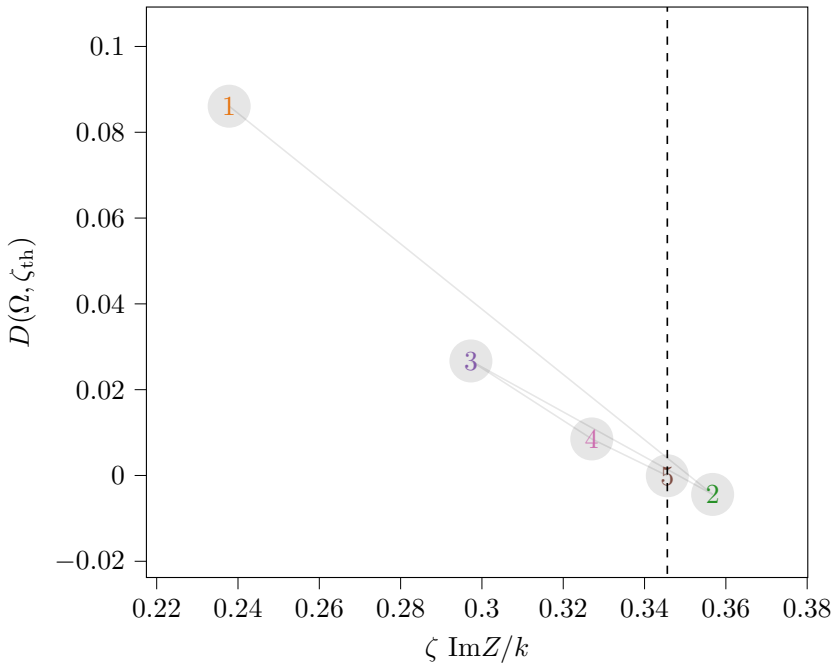

Figure 4.1. Example of the LLD threshold (black dashed line) evaluation in MELODY through the direct computation of the determinant in Eq. (2.91). The calculation is performed in BSM for a double-harmonic RF system ($r_h = 2$) with $r_v = 0.5$, $\eta > 0$, $\text{Im}Z/k = -0.07\ \Omega$, $f_c/f_{\text{rf}} = 20$, $\mu = 1.5$, $\phi_{\max} = 1.37$ rad and $e_{\text{th}} = 2 \times 10^{-2}$ using the accelerator parameters in Tab. 4.1.

these functions were discretized by multiplying them with step-like functions $s_n(\mathcal{E})$, where $\mathcal{E}_n$ is the n-th sample of the energy grid, i.e.

$$C_m(\mathcal{E}, \omega) = \sum_{n=0}^{N_\mathcal{E}} s_n(\mathcal{E}) C_m(\mathcal{E}_n, \omega)\,, \tag{4.5}$$

where

$$s_n(\mathcal{E}) = \begin{cases} 1/\Delta\mathcal{E}_n, & \mathcal{E}_n - \Delta\mathcal{E}_n/2 < \mathcal{E} \leq \mathcal{E}_n + \Delta\mathcal{E}_n/2 \\ 0, & \text{elsewhere} \end{cases}, \tag{4.6}$$

and $\Delta\mathcal{E}_n$ is the thickness of the corresponding step. However, the MELODY code implements a refined non-uniform mesh, with a total number of points $N_\mathcal{E}$, to have a high-resolution matrix in energy and frequency when close to the center or edge of the potential well.

Eventually, Eq. (2.95) can be expressed as an eigenvalue problem of a linear algebra of the kind

$$\Omega^2 C_m\left(\mathcal{E}_n, \Omega\right) = \sum_{n'=1}^{N_\mathcal{E}} \sum_{m'=1}^{m_{\max}} M_{nmn'm'} C_{m'}\left(\mathcal{E}_{n'}, \Omega\right)\,, \tag{4.7}$$

where the matrix is equal to

$$M_{nmn'm'} = m^2\omega_s^2\left(\mathcal{E}_n\right)\delta_{nn'}\delta_{mm'} - \frac{2\zeta m^2\omega_s^2\left(\mathcal{E}_n\right)\omega_{s0}\Delta\mathcal{E}_{n'}}{\pi A_N\omega_s\left(\mathcal{E}_{n'}\right)}\frac{dg}{d\mathcal{E}}\left(\mathcal{E}_n\right) \times \mathrm{Im}\left\{\sum_{k=1}^{k_{\max}}\frac{Z_k/k}{h}I_{mk}\left(\mathcal{E}_n\right)I^*_{m'k}\left(\mathcal{E}_{n'}\right)\right\}. \tag{4.8}$$

The function $\delta_{nn'}$ is the Kronecker delta while $m_{\max}$ and $k_{\max}$ are, respectively, the maximum values of the azimuthal mode and the revolution harmonic number. In general, the exact solution requires an infinite number of azimuthal modes and revolution frequency harmonics; however, a truncation must be considered for numerical reasons.

Following the Oide-Yokoya method, the eigenvalues of the matrix in Eq. (4.8) are calculated as a function of the intensity parameter ζ. In particular, the method is based on computing the difference between the maximum eigenfrequency and the maximum incoherent frequency to find the threshold. Thus, as Fig. 4.2 shows, the LLD threshold (black dashed line) corresponds to the point where the difference between the two functions vanishes.

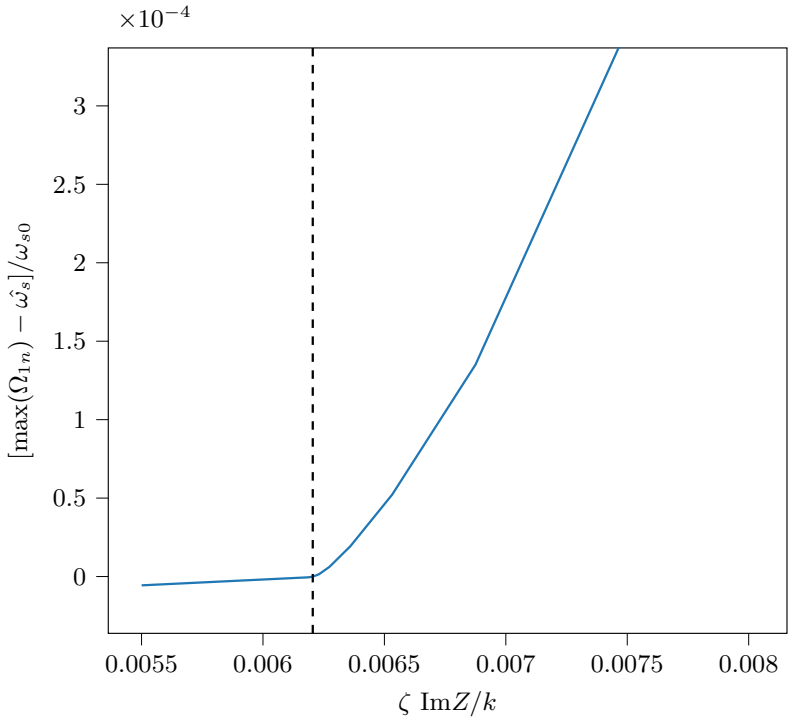

Figure 4.2. Example of the LLD threshold (black, dashed) evaluated with the MELODY with the Oide-Yokoya method. The eigenvalues in Eq. (4.7) are found for LHC parameters with $\eta > 0$, $\mathrm{Im}Z/k = 0.07\ \Omega$, $f_c/f_{\mathrm{rf}} = 10$, $V_0 = 6$ MV, $\mu = 2$, and $\tau_{\mathrm{full}} = 1.3$ ns.

4.2 The Beam Longitudinal Dynamics simulation suite

Since 2014, the Beam Longitudinal Dynamics simulation suite (BLonD) [27–29] has been developed at CERN, an open-source particle tracking code designed to simulate longitudinal motion in synchrotrons. The code is written in two high-level and general-purpose programming languages, Python and C++. It makes use of well-established and efficient scientific libraries such as Numpy [74], Scipy [75], and CuPy [76].

The code employs the widely used concept of macroparticles having the same charge-to-mass ratio as the actual particles. In reality, the intensity of bunches typically spans from 10^8 to 10^{13} particles per bunch, whereas simulations commonly employ only of the order of 10^4 to 10^7 macroparticles per bunch. The lower number of macroparticles with respect to a real bunch is a compromise that allows to mitigate computational resources in simulations.

A distinctive aspect of the BLonD code is its capability to simulate the evolution of both the coordinates of beam particles and the RF system parameters, including its frequency and voltage vector. This is achieved by monitoring them with respect to an external time reference, equivalent to beam measurements in real synchrotrons. The particle coordinate systems in BLonD are the canonically conjugate variables Δt and ΔE, namely relative displacement in time with respect to the reference time and the designed total energy. This offers the advantage of including beam-based feedback systems and collective effects. Furthermore, the code offers additional functionality, including its capacity to generate a matched bunch with the RF and collective effects from a given line density function or distribution.

The BLonD code functionality has been benchmarked [77] through widespread applications across all the CERN [78] and other synchrotrons of other accelerator facilities [79–82] synchrotrons. Below, an overview of the bunch generation and beam tracking algorithm is provided. For a complete description of the functionalities of the BLonD code suite code, refer to [27].

4.2.1 Bunch generation

The routine used in BLonD for matching bunches in the RF bucket from distribution functions is very similar to the iterative algorithm Eq. (4.3) implemented in MELODY. The main difference lies in the fact that BLonD deals with macroparticles binned in the longitudinal phase space by a discrete distribution function. Under certain circumstances, this binning causes numerical noise that can be observed at high frequency and leads to unphysical results, such as artificial emittance blow-up or erroneous beam instability of intensity well below the physical threshold [83]. Therefore, choosing an appropriate number of macroparticles in conjunction with a correct sampling frequency for a given distribution is crucial to minimize the numerical noise. Therefore, a benchmark with a significantly large number of macroparticles is needed to validate the choice.

The bunch generation routine requires the type of target distribution and emittance (or bunch length) as input parameters. The potential well is then preprocessed to check for the minimum, maximum, and center of the frame around the separatrix. For the sake of consistency with MELODY, instead of the emittance, we force as

input the maximum oscillation energy, $\mathcal{E}_{\max}$, as the size of the bunch, in order to generate from both codes the same longitudinal line density (see Sec. 4.3).

Figure 4.3 illustrates the flowchart of the bunch generation function performed in BLonD. After computing the Hamiltonian, the matching procedure consists of iteratively placing the bunch in the center of the distorted potential well until convergence is reached. After finding a stationary solution, random sampling generates the particle distribution according to the density function $\mathcal{F}$.

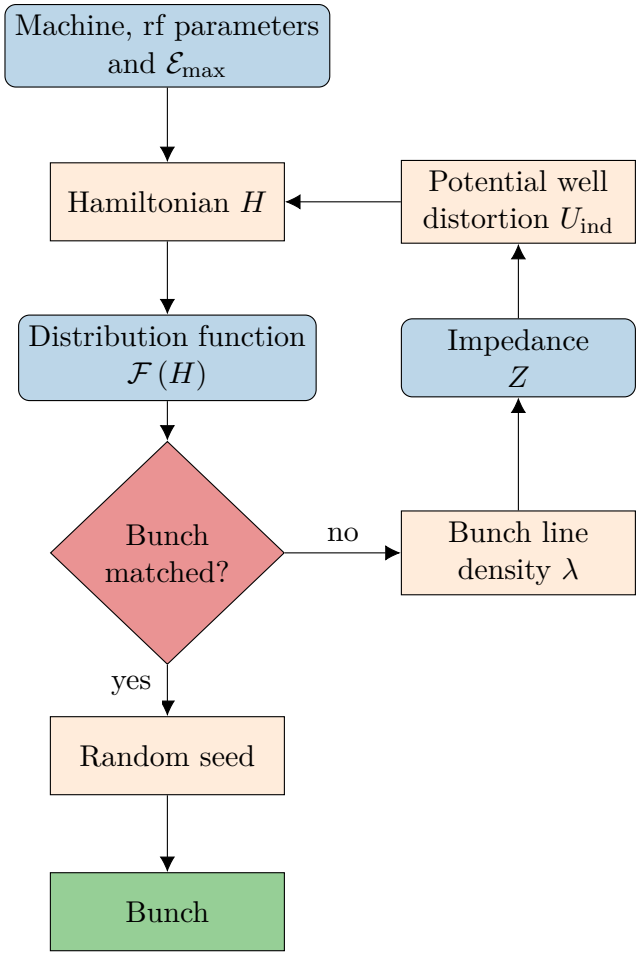

Figure 4.3. Flowcharts of the routines implemented in BLonD to generate bunches matched to the RF bucket with intensity effects. The blue boxes represent the user input; the sharp rectangular boxes are the states after parameters were processed with the respective functions, and the diamond box is the decision point between the loop and the output. The output is highlighted in green.

4.2.2 Tracking algorithm

BLonD describes the evolution of the particles and RF parameters with respect to a reference time, $t_{d,(n)}$, defined as

$$t_{d,(n)} = \sum_{i=1}^{n} T_{\mathrm{rev},(i)}\,, \quad n = 0, 1, 2...\,, \tag{4.9}$$

where the revolution period can change turn-by-turn in acceleration. The time coordinate of the particle is then $\Delta t_{(n)} = t_{(n)} - t_{d,(n-1)}$. The relative energy gain with respect to the designed energy $\Delta E_{(n)} = E_{(n)} - E_{d,(n)}$ is basically an implementation of Eq. (2.23).

Firstly, a given particle's energy ΔE is updated from turn n to $n+1$, based on the particle's arrival time and the RF voltage kicks received. Subsequently, the time coordinate of the particle is updated with the new energy of the particle. Thus, the discrete equations of motion, used for tracking simulation, become

$$\begin{aligned}
\Delta E_{(n+1)} &= \Delta E_{(n)} + \sum_{i=1}^{n_{\mathrm{rf}}} qV_{i,(n)} \sin(\omega_{\mathrm{rf},i,(n)} \Delta t_{(n)} + \phi_{\mathrm{rf},i,(n)}) + E_{\mathrm{other},(n)}\,, \\
\Delta t_{(n+1)} &= \Delta t_{(n)} + T_{\mathrm{rev},(n+1)} \left[\left(1 + \alpha_{(n+1)} \frac{\Delta p_{(n+1)}}{p_{(n+1)}} \right) \frac{1 + \frac{\Delta E_{(n+1)}}{E_{(n+1)}}}{1 + \frac{\Delta p_{(n+1)}}{p_{(n+1)}}} - 1 \right]\,,
\end{aligned} \tag{4.10}$$

where V_i is the voltage amplitude, $\omega_{\mathrm{rf},i}$ the angular RF frequency, and $\phi_{\mathrm{rf},i}$ the phase of the RF system i. The term $E_{\mathrm{other},(n)}$ represents additional contributions such as induced voltage, etc. Note that Eq. (4.10) represents a simplified equation of motion where the first-order of the momentum compaction factor is used. For a more detailed form of the equations, refer to [27].

4.3 Comparison of BLonD and MELODY

From the beam stability point of view, BLonD is a pure time-domain code that needs to be stopped after tracking a certain number of turns. This means that slow instabilities might be missed, which is most critical for synchrotrons with very long beam presence like the LHC. Moreover, such simulations do not always provide a direct understanding of the physics behind the tracking. Nonetheless, macroparticle simulations are very flexible and can assess stability in very complex scenarios, typically out of reach for a Vlasov solver.

On the other hand, in MELODY, the phase space distribution is modeled as a continuous function rather than a bunch of discrete particles. The Vlasov equation is then addressed utilizing the two available methods, providing a remarkable understanding of unstable modes and their mitigation parameters. Typically, it is much less computationally intensive than BLonD since it is based on analytical equations.

The two methods are, therefore, complementary approaches describing the same beam dynamics. For a consistent analysis, it is of primary importance that the studies performed on both codes come from an identical initial bunch distribution.

The LHC [84] accelerator and RF parameters, outlined in Tab. 4.1, have been considered as a reference case for the benchmark. As an example, a single proton bunch with a intensity of $N_p = 2.9 \times 10^{10}$ has been generated and matched in the RF bucket, taking into account collective effects.

Table 4.1. Main RF parameters of the LHC [84].

Parameter	**Unit**	**Value**
Circumference, $2\pi R$	m	26658.86
Main harmonic number, h		35640
Main RF frequency, f_{rf}	MHz	400.79
Beam energy, E_0	TeV	0.45
Main RF voltage V_0	MV	6
Effective impedance, $\mathrm{Im}Z/k$	Ω	0.07

Figure 4.4 illustrates the comparison of the line density $\lambda(\phi)$ computed in BLonD (blue) and in MELODY (orange, dashed) for three different configurations, i.e., single RF, BSM, and BLM. The BSM and BLM are depicted on top considering a fourth harmonic RF system ($r_h = 4$) with a voltage ratio $r_{_V} = 0.25$. For completeness, the single RF system case is also provided (bottom). BLonD shows some noise on the line density peak due to the macroparticle binning in the discretized line density. An excellent agreement between the codes is reached.

We confirmed the consistency of the two tools generating an identical bunch. In the upcoming chapters, we will compare MELODY and BLonD for more complex cases of beam stability.

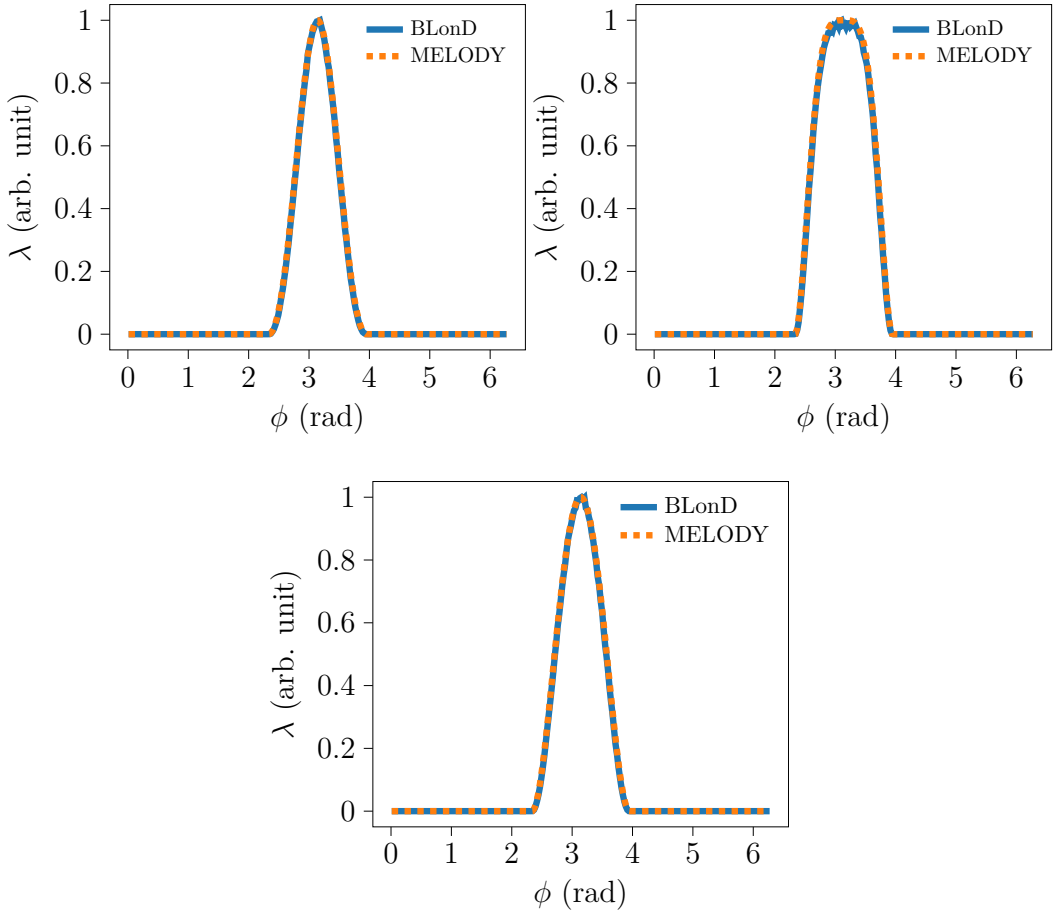

Figure 4.4. Comparison between the line density of a bunch generated using the BLonD (blue) and MELODY code (orange). Collective effects have been included considering number of particles $N_p = 2.9 \times 10^{10}$ with $\phi_{\max} = 0.8$ rad and $f_c/f_{\mathrm{rf}} = 10$. The cases of BSM (top left) and BLM (top right) are considered with both $\mu = 1.5$, $r_v = 0.25$ and $r_H = 4$. The single RF case is shown at the bottom.

Chapter 5

Analytical and numerical results for purely inductive impedances

The analytical equation (3.20) of the longitudinal LLD threshold in BSM, derived in Chapter 3, is benchmarked and compared with the semi-analytical code MELODY for constant inductive impedance above transition energy. Furthermore, a method based on bunch centroid evolution in macroparticle tracking simulations in BLonD is provided. In the frequency domain, this technique allows the observation of coherent modes emerging from the incoherent band above the LLD threshold. The findings are then compared with results from MELODY, computing the van Kampen modes through the Oide-Yokoya method (Chapter 4) in DRF.

The BLM is further analyzed numerically, showing its limitations caused by the presence of zero derivatives of the synchrotron frequency distribution $df_s/d\phi = 0$ in the bunch, which leads to a LLD at any intensity. In addition, the impact of a relative phase error of the two RF systems on the LLD threshold is investigated, highlighting the main critical issues in BLM and BSM.

Below transition energy (more generally $\eta \mathrm{Im}Z/k < 0$), the additional focusing force due to beam-induced voltage distorts the potential well, ultimately collapsing the bucket when increasing the intensity. This can occur before the LLD damping threshold for a relatively short bunch length. Therefore, the limiting conditions for a binomial particle distribution calculated in Chapter 3 are used and benchmarked with MELODY. In BSM, the LLD threshold behaves very differently compared to the above-transition-energy case, showing a non-monotonic behavior with a zero threshold where the derivative of the synchrotron frequency distribution is positive. The study is conducted with the semi-analytical code MELODY.

5.1 Above transition energy

5.1.1 LLD threshold in BSM: Analytical estimates and numerical solutions

To validate the analytical equation of the LLD threhsold (Chapter 3), Eq. (3.20) is compared with semianalytical results obtained using MELODY. In order to facilitate a direct and comprehensive comparison with the analysis conducted for the single

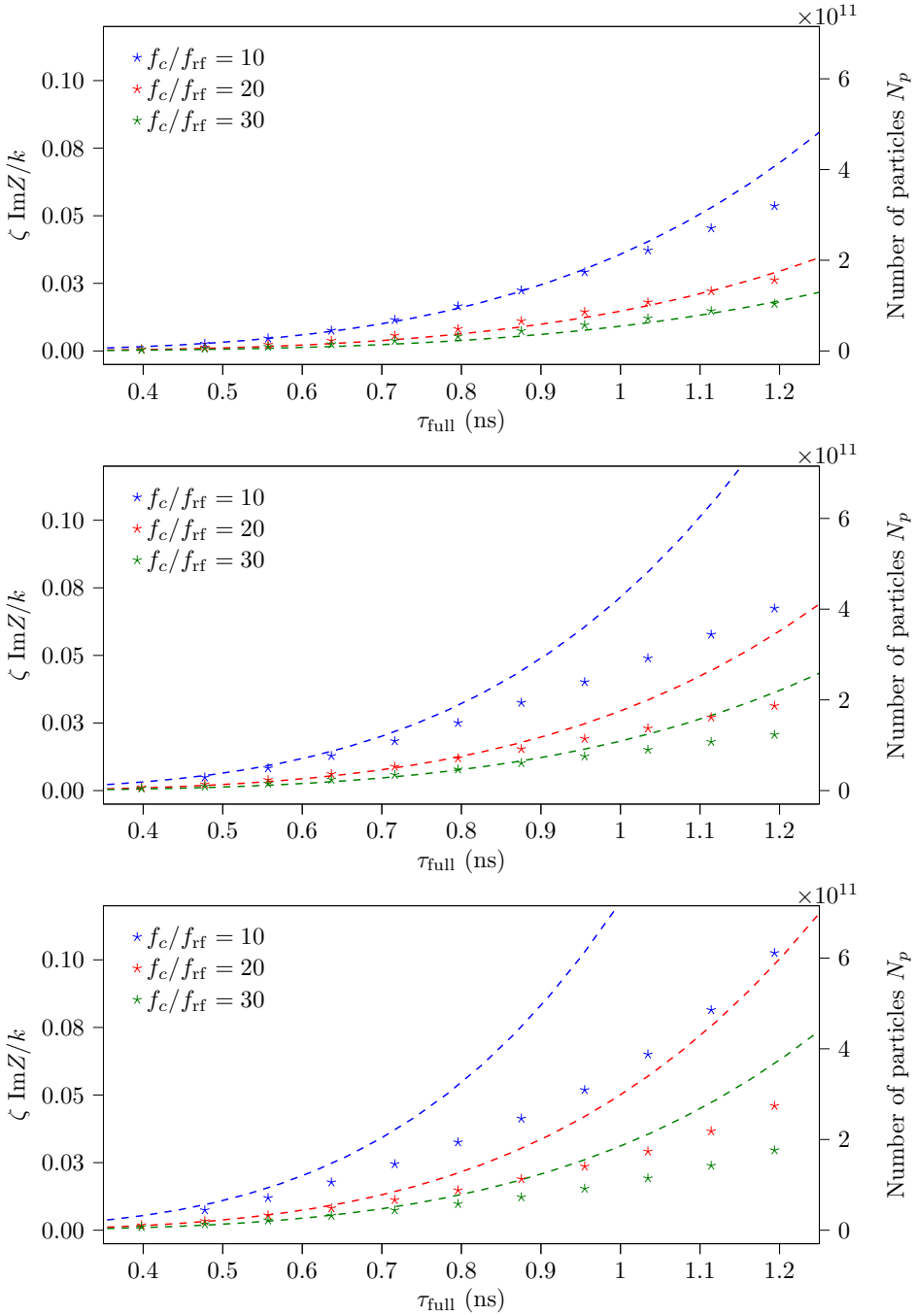

Figure 5.1. The LLD threshold, for the second (top; $r_h = 2$), third (center; $r_h = 3$) and the fourth (bottom; $r_h = 4$) harmonic RF system case, as a function of the full bunch length τ_{full} and considering only the first azimuthal mode $m = 1$. The thresholds are calculated in MELODY and compared with the analytical equation (dashed lines) for different impedance cutoff frequencies. The computation is performed based on inductive impedance, $\mathrm{Im}Z/k = 0.07\ \Omega$, voltage ratio, $r_V = 1/r_h$, and binomial coefficient, $\mu = 1.5$.

RF [45], the accelerator parameters given in Tab. 4.1 have again been assumed as a reference case.

Figure 5.1 summaries the comparison between the threshold in Eq. (3.20) (dashed) and MELODY (stars) as a function of the full bunch length for different cutoff frequencies. It has been repeated for three different DRF configurations with a the second ($r_h = 2$; top), third ($r_h = 3$; center), and fourth ($r_h = 4$; bottom) harmonic RF system. The analytical equation agrees very well with the MELODY results, in particular for short bunches, and increases monotonically along the bunch length. The threshold scales inversely with the cutoff frequency, as predicted by Eq. (3.22). Some discrepancies arise for larger bunch lengths due to the short-bunch approximation taken into account during the derivation of the equation. Moreover, for $r_h = 4$ the threshold equation can diverge earlier from the semi-analytical calculation as for the impedance cutoff frequency $f_c/f_{\mathrm{rf}} = 10$ (blue, dashed).

Computing the threshold along the full bucket ($\phi_{\max} = \pi$), Fig. 5.2 shows that the LLD threshold preserves its monotonic behavior. This result does not agree with observations in [25], where the LLD threshold decreases once crossing the zero derivatives of the frequency distribution (Fig. 2.11). The discrepancy arises from the fact that in [25], a different definition of LLD threshold has been applied based on the decoherence of the particles after a longitudinal phase kick.

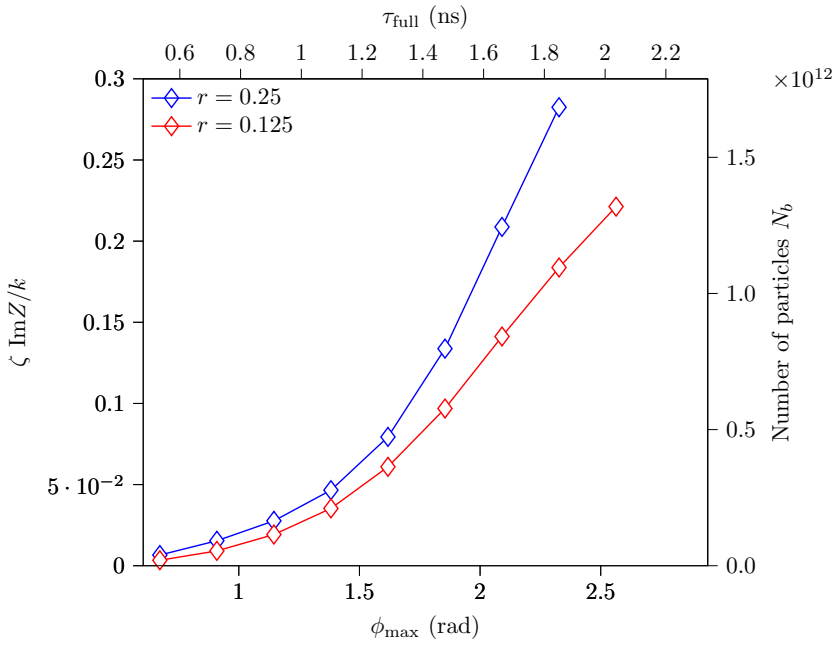

Figure 5.2. LLD threshold as a function of the bunch length. The thresholds are computed with MELODY for the voltage ratio $r = 0.25$ (blue) and $r = 0.125$ (red) by considering Im$Z/k = 0.07\ \Omega$ with a cutoff frequency $f_c/f_{\mathrm{rf}} = 10$ and binomial coefficient, μ=2.

It should be pointed out that the computation of the LLD threshold cannot be performed above a certain intensity (see Fig. 5.2). This limitation is due to the defocusing force caused by the induced voltage of the inductive impedance. The additional force deforms the total potential, limiting the bunch intensity by the bucket acceptance. It aligns well with BLonD simulations for which generating matched bunches with the RF bucket beyond these intensity limits was also not possible.

An alternative technique to study the loss of Landau damping is through the longitudinal beam spectrum in the frequency domain. In particle tracking simulations, we exploit the bunch centroid evolution to analyze at which intensity the LLD occurs. As the azimuthal modes correspond to specific frequencies arising from the incoherent band of synchrotron frequencies, we study the spectrum of the bunch phase offset evolution as an observable for the dipole mode.

To perform the simulation in BLonD, a bunch with 10^6 macroparticles was generated, matched with intensity effects, and then tracked for 10^6 turns with a double harmonic RF system with harmonic ratio of $r_h = 4$ in BSM and a voltage ratio, $r_V = 0.25$. The large number of turns ensures a good frequency resolution of the spectrum and covers a sufficient number of synchrotron oscillations. Thereafter, a fast Fourier transform (FFT) [85] of the bunch center of mass has been performed.

Figure 5.3 shows two example of normalized spectra for intensities of $N_p = 1.26 \times 10^{11}$ (left), and $N_p = 2.98 \times 10^{11}$ (right) based on the accelerator parameters in Tab. 4.1. Very good agreements between the beam spectra bandwidth and the boundaries of the incoherent band calculated in MELODY (red dashed lines) are achieved. Below the LLD threshold (Fig. 5.3; left), no coherent modes are observed outside the incoherent band. However, above the threshold (Fig. 5.3; right), for a sufficiently large resolution, a well-defined peak caused by a specific mode is visible beyond the maximum of the incoherent band. The black dashed line indicates the frequency of the van Kampen mode computed by means of the Oide-Yokoya method, establishing once again the excellent agreement between MELODY and BLonD.

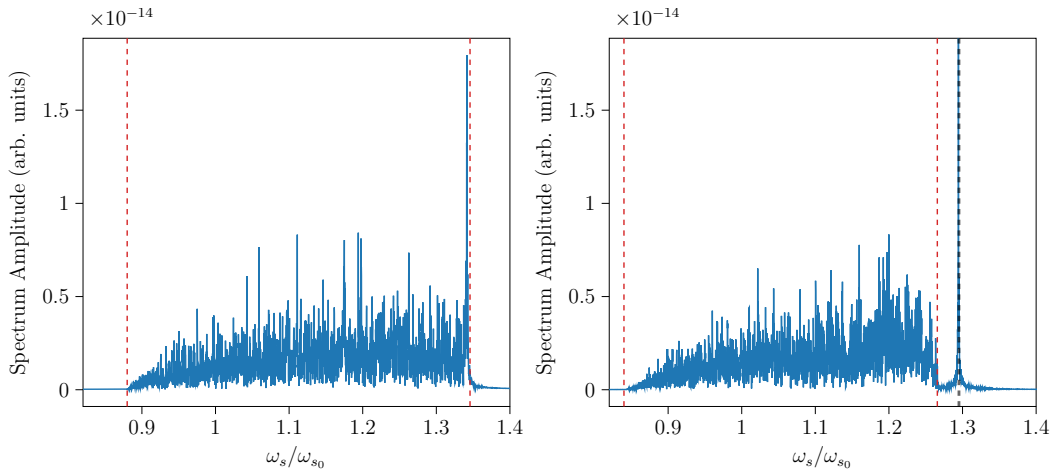

Figure 5.3. Normalized spectra of the bunch center of mass evolution computed in BLonD in BSM for intensities $N_p = 1.2 \times 10^{11}$ (left) and $N_p = 3.0 \times 10^{11}$ (right). The tracking was performed with 10^6 macroparticles with 10^6 turns, for $r_h = 4$, $r_V = 0.25$, $\mathrm{Im}Z/k = 0.07\ \Omega$, $\phi_{\max} = 1$ rad, $f_c/f_{\mathrm{rf}} = 10$ and accelerator parameters from Tab. 4.1. The red dashed lines indicate the minimum and maximum of the incoherent frequency band together with the van Kampen mode (black, dashed) computed in MELODY.

The study has been extended by an intensity scan to observe the coherent mode behavior. Again a bunch with 10^6 macroparticles is generated in BLonD, matched with intensity effects, and then tracked for 10^6 turns. The tracking process

is moreover run for different bunch lengths, thereby covering several parts of the synchrotron frequency distribution (Fig. 2.11, green). In order to better show the coherent frequencies in the spectrum, a Hanning filter is applied to the signal. This type of filter is commonly applied in statistics for smoothing [86].

Figure 5.4 summarizes the normalized mode frequencies versus bunch in BLonD (color coding) and the emerging Van Kampen modes computed in MELODY (red) using the Oide-Yokoya method. For each intensity, the vertical slice of the plot represents the normalized spectra of the bunch offset as introduced in Fig. 5.3. At the LLD threshold (red, dashed), the van Kampen mode, which represents an undamped mode, coincides with the maximum frequency of the incoherent synchrotron frequency band (black). With this technique in tracking simulation alone, it is difficult to discriminate properly the coherent mode from the continuous spectrum when the intensity is close to the LLD threshold. An excellent agreement is shown between BLonD and MELODY, even in the case of a higher-order mode than the dipole mode seen as the second emerged mode at $\phi_{\max} = 1.0$ rad in Fig. 5.4 (left).

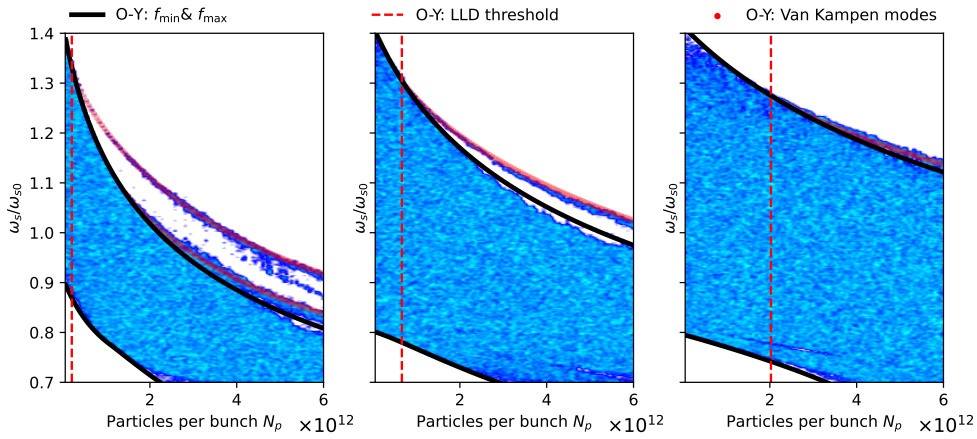

Figure 5.4. Absolute value of the normalized mode frequency found from macro-particle simulations using BLonD (blue color scale) and from MELODY (red dotted line) as a function of bunch intensity for a constant impedance $\mathrm{Im}Z/k = 0.07\ \Omega$ and $f_c/f_{\mathrm{rf}} = 10$. The minimum and maximum incoherent frequencies are obtained with MELODY and are shown as solid black lines. The dashed red lines indicate the LLD intensity thresholds obtained from calculations performed for three different bunch lengths, $\phi_{\max} = 1.0$ rad (left), $\phi_{\max} = 1.5$ rad (centre) and $\phi_{\max} = 2.0$ rad (right) by assuming $r_h = 4$, $r_v = 0.25$, $\mu = 1.5$ and number of azimuthal modes, $m = 15$.

5.1.2 Semi-analytical studies in BLM

We consider now the case of DRF when both RF systems are perfectly in counter phase at the bunch position (BLM). Note that the case of a relative phase error between the RF systems will be studied in the next section. In the context of BLM, it becomes nontrivial to determine an analytical closed solution for the LLD threshold since the maximum incoherent frequency, in most cases, varies depending on the bunch length. Nonetheless, we can still derive the threshold by solving the generally valid Eq. (4.7) semi-analytically with MELODY.

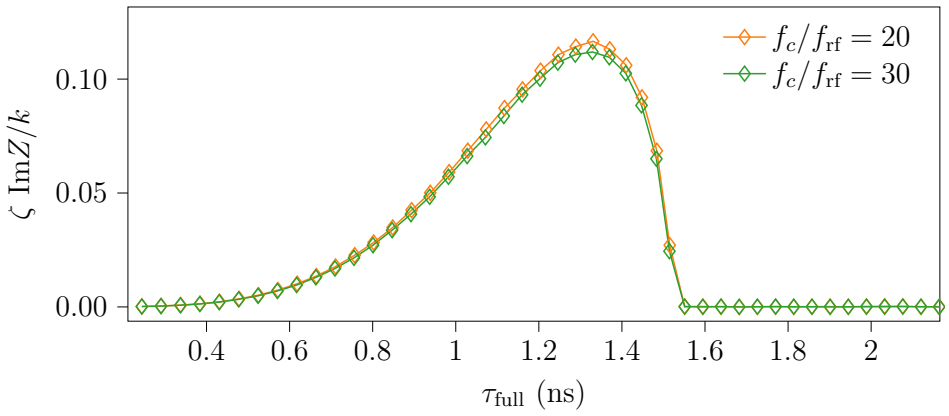

(a) $r_h = 2;\ r_V = 0.4.$

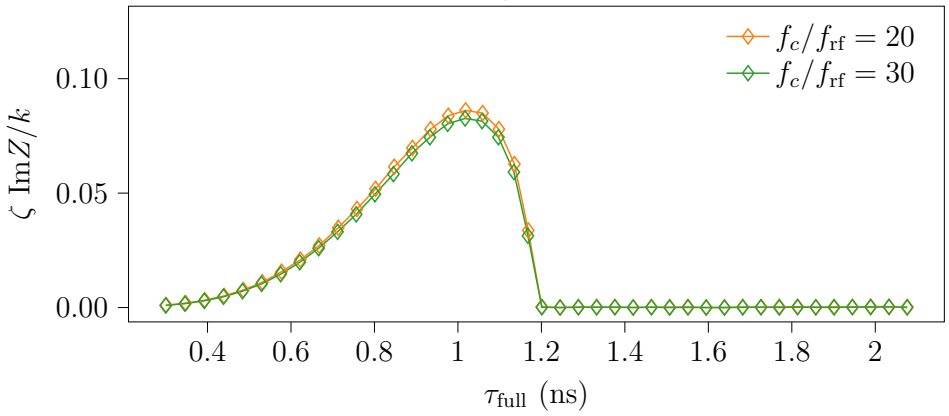

(b) $r_h = 3;\ r_V = 0.3.$

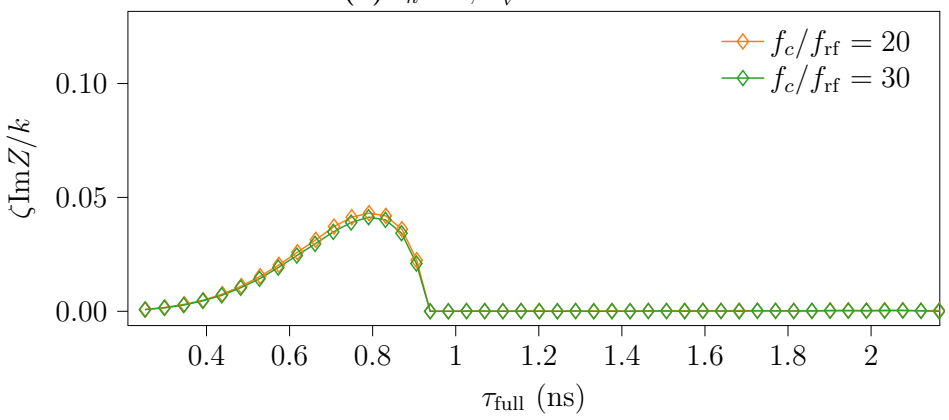

(c) $r_h = 4;\ r_V = 0.2.$

Figure 5.5. LLD thresholds, computed with the MELODY code, in BLM for three cases of double harmonic RF systems; the second harmonic (left; $r_h = 2$), the third harmonic (center; $r_h = 3$), and the fourth harmonic (right; $r_h = 4$) of the principal RF system. The thresholds are plotted as a function of the full bunch length. The thresholds are calculated using different impedance cutoff frequencies and parameters set as $\mathrm{Im}Z/k = 0.07\ \Omega$, and $\mu = 1.5$.

Figure 5.5 illustrates the LLD threshold in BLM as a function of the full bunch length for harmonic number ratios of $r_h = 2$ (top), $r_h = 3$ (center) and $r_h = 4$ (bottom) respectively. Contrary to the BSM, a non-monotonic threshold is observed. Previous studies [26] highlighted the impact of the zero derivatives of the synchrotron frequency distribution, observing that once the bunch length exceeds the critical point where $d\omega_s/d\phi$ vanishes, Landau damping is lost even at zero intensity. In the given configuration, the presence of the discrete mode is highly influenced by the tails of the distribution. When the bunch length exceeds the point where $d\omega_s/d\phi = 0$, a van Kampen mode is already located at the maximum of the frequency distribution at zero intensity (Fig. 5.6). Therefore, the tiniest collective effect pushes the mode outside the incoherent frequency band, causing the LLD. As a result, any type of perturbation of the distribution function is insufficient to restore Landau damping. In BLM, contrary to the BMS, the positioning of the maximum

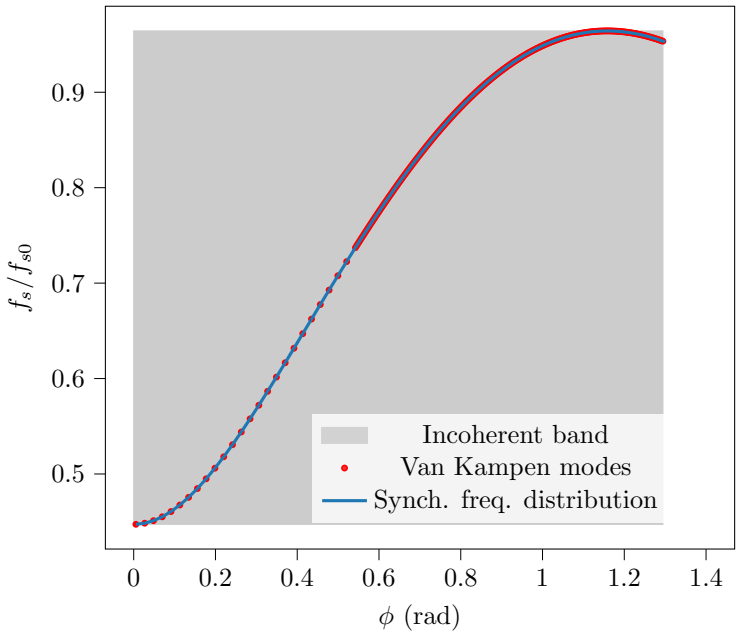

Figure 5.6. Van Kampen modes (red) and synchrotron frequency distribution (blue) in BLM for harmonic ratio, $r_h = 4$, voltage ratio, $r_v = 0.2$, and binomial factor, $\mu = 1.5$, at zero intensity. The incoherent band is illustrated in grey.

synchrotron frequency on the edge of the synchrotron frequency distribution results in the independence of the LLD threshold from the impedance cutoff frequency, f_c. This observation is consistent with the findings of [45] where, for single RF with $\eta \mathrm{Im}Z/k < 0$, no dependency on the cutoff frequency, f_c was observed. In addition, the van Kampen mode spectra confirm their sensitivity to f_c only in the proximity of the bunch center.

Although the ideal BLM provides a larger synchrotron frequency spread (as illustrated in Fig. 2.11), leading to higher LLD thresholds compared to BSM (Fig. 5.1), it is limited by the presence of zero derivatives in the synchrotron frequency distribution. This represents a constraint on the bunch length that progressively becomes more restrictive as we increase the order, r_h, of the harmonic RF system.

5.1.3 The LLD threshold in the presence of relative phase shift between the RF systems

In Sec. 2.1.6, it is shown that an additional limitation might come from an unavoidable relative phase shift between the RF systems. Since the LLD threshold strictly depends on the maximum incoherent frequency, the relative phase shift can represent a limitation. To analyze its impact, we computed the LLD threshold along two degrees of freedom in MELODY: relative phase between both RF systems and maximum synchrotron oscillation energy $\mathcal{E}_{\max}$ considering only the first azimuthal mode $m = 1$. Different voltage ratios, namely $r_V = 0.1$ (Fig. 5.7, left), and $r_V = 0.2$ (Fig. 5.7, right) have been considered for the case of a harmonic number ratio of $r_h = 4$. As expected, the threshold is symmetric along Φ_2, showing very interesting hybrid configurations with higher LLD thresholds than the conventional BSM and BLM. Similarly to Fig. 5.5, for high synchrotron energy oscillation (e.g. $\mathcal{E}_{\max} > 0.6$), moving from $\Phi_2 = \pi$ (white) towards $\Phi_2 = 0$ and $\Phi_2 = 2\pi$, the threshold drops down to zero intensity due to the zero derivative of the synchrotron frequency distribution, $df_s/d\phi = 0$.

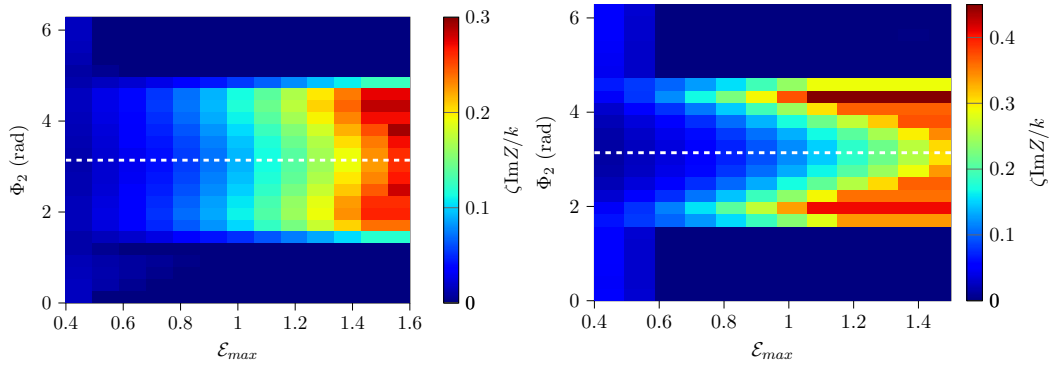

(a) $r_V = 0.1$. **(b)** $r_V = 0.2$.

Figure 5.7. Threshold of LLD (color coding) computed in MELODY as a function of the maximum synchrotron oscillation energy and relative phase, Φ_2. Based on the parameters in Tab. 4.1, two voltage ratios are considered as representative examples, i.e., $r_V = 0.1$ (left) and $r_V = 0.2$ (right) with a harmonic number ratio $r_h = 4$. The ideal BSM case is highlighted in white.

To better visualize the effect of the relative phase on the LLD threshold, two-dimensional slices of Fig. 5.7 have been considered. As long as the bunch length is small enough the ideal BLM has a higher LLD threshold (Fig. 5.8; blue circles). However, higher LLD thresholds are predicted for $\Phi_2 \approx 2$ rad and $\Phi_2 \approx 4.4$ rad. In particular, we observe threshold increase of a factor ~ 3 ($\mathcal{E}_{\max} = 1$) and ~ 4 ($\mathcal{E}_{\max} = 0.4$) with respect to the BSM and a factor 1.3 to BLM. This interesting result agrees with the past studies [25], as well as measurements [87]. Nonetheless, the margin of error in the relative phase is very narrow. Therefore, it is extremely challenging to work precisely in these configurations.

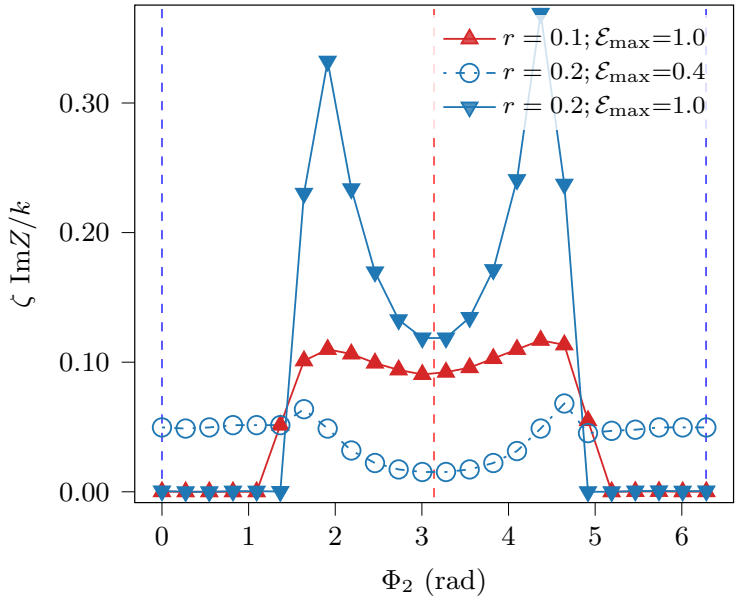

Figure 5.8. The LLD threshold computed in MELODY as a function of the relative phase for harmonic number ratios $r_h = 4$ for selected cases from Fig. 5.7, namely $\mathcal{E}_{\max} = 0.4$ (circles) and $\mathcal{E}_{\max} = 1.0$ (triangles). The BLM working point is highlighted in blue, while the BSM one is shown in red.

5.2 Constant inductive impedance below transition energy

Until now, we have focused on the case of $\eta \mathrm{Im}Z/k > 0$, which covers the configuration of most accelerators at CERN, including PS, SPS, and LHC. We will now study the less common case of inductive impedance below transition energy (or capacitive above), which represents, for instance, the case of the PSB at flattop. In this regime, we show that the critical intensity that induces the bucket to collapse often occurs before the LLD threshold.

5.2.1 Upper limit intensity due to the induced focusing force

For a purely inductive impedance below transition energy (or capacitive above), the induced voltage acts as an additional focusing force, shrinking the bucket. For a binomial distribution (2.62), we derived in Chapter 3 the maximum intensity ζ_{cc} before the collapse of the buckets occurs. Results obtained by the iterative procedure according to Eq. (4.3) confirm the analytic predictions given by Eq. (3.27) for both BSM (Fig. 5.9, top) and BLM (Fig. 5.9, bottom) with harmonic number ratio of $r_h = 4$ and voltage ratio of $r_V = 0.25$. In particular, the results from Eq. (3.27) (black) perfectly match the upper-intensity limit computed with MELODY (iterative algorithm, dots). In the case of $\mu \neq 0.5$, only empirically fit functions can be proposed to complement the iterative algorithm for the moment, and it will be subject for further study.

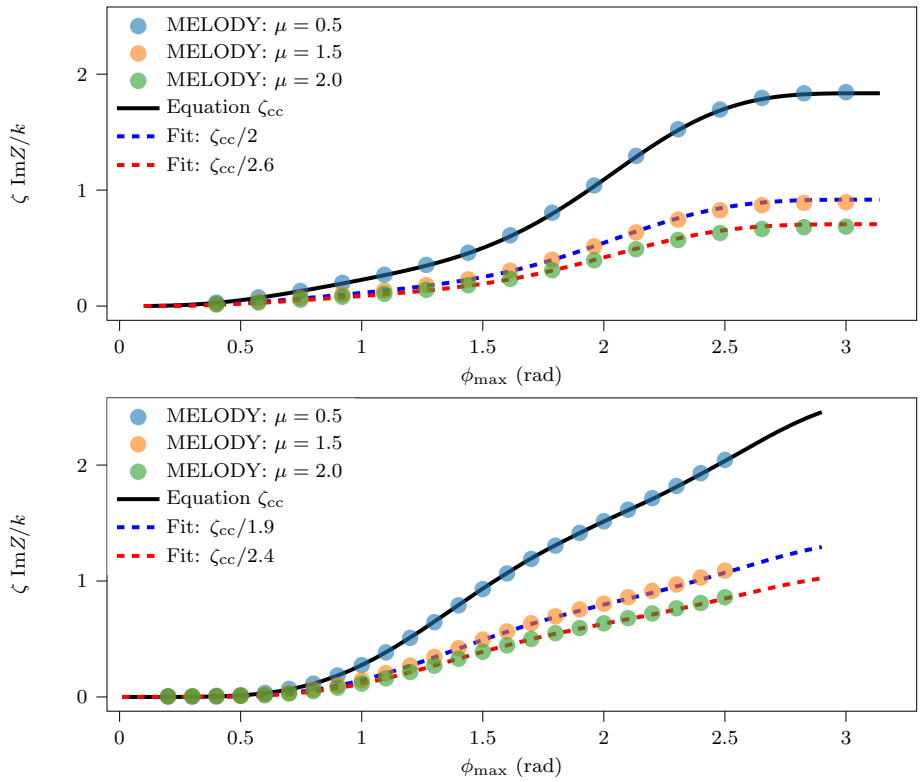

Figure 5.9. Comparison of the critical curve according to Eq. (3.27) (black) and MELODY (dots) in the BSM (top) and BLM (bottom) configurations, for harmonic and voltage ratios $r_h = 4$ and $r_V = 0.25$. For distribution functions with $\mu = 1.5$ and $\mu = 2.0$, fitted functions (dashed lines) are proposed.

5.2.2 The LLD damping threshold: semi-analytical approach

For $\eta \mathrm{Im}Z/k < 0$, which refers to inductive impedance below transition energy, coherent modes emerge below the minimum incoherent synchrotron frequency band. Hence, the LLD threshold is reached when $\Omega \equiv \min[f_s(\phi)]$. In configurations where this minimum falls on the tail of the frequency distribution, such as BSM (or BLM in specific cases), we expect that the LLD becomes independent of the cutoff frequency, as seen in single RF case [45].

Figure 5.10 summarizes the LLD threshold, computed with MELODY, as a function of the particle maximum phase deviation in BSM. For a harmonic number ratio of $r_h = 2$ Fig. 5.10 (top) confirms that the LLD threshold is indeed independent of the cutoff frequency for $\mu = 1.5$ (diamonds) and in agreement with the single RF system case [45]. Furthermore, the threshold disappears beyond the critical curve for larger bunch lengths as the bunch collapses. Also for particle distributions with $\mu = 0.5$, this dependence persists.

In the fourth harmonic configuration (Fig. 5.10; bottom), the LLD is no longer a monotonic function [68] caused by the presence of a positive derivative in the synchrotron frequency distribution within the bunch. In this grey zone where $df_s/d\phi > 0$, the minimum of the synchrotron frequency distribution is no longer in the tail of the bunch. Similar to the BLM case above transition energy (Fig. 5.5),

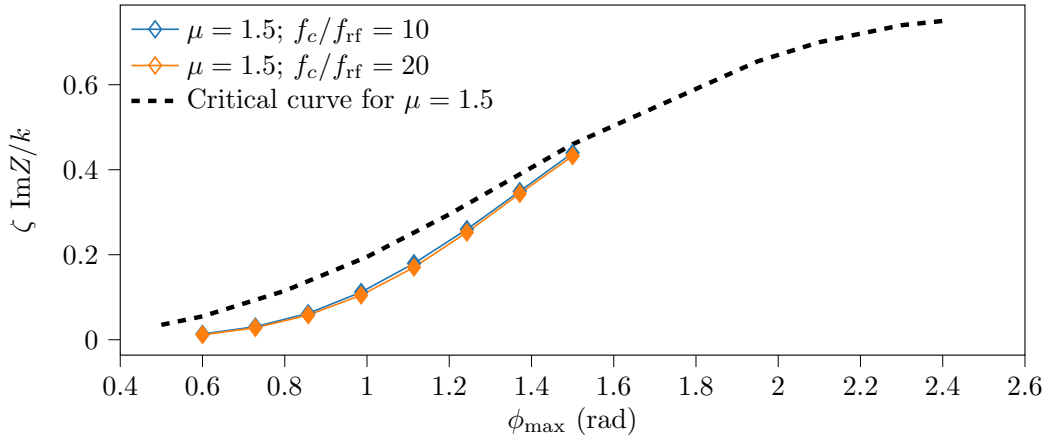

(a) $h_r = 2$; $r = 0.5$.

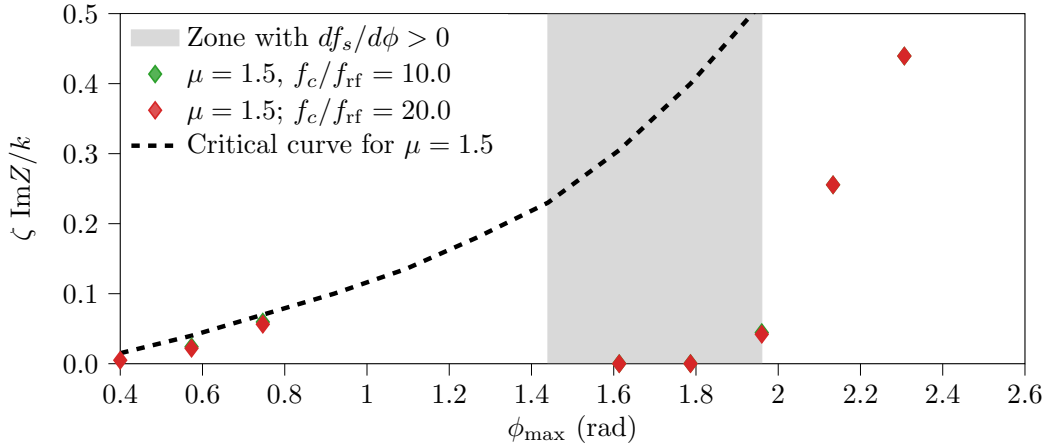

(b) $h_r = 4$; $r = 0.25$.

Figure 5.10. The LLD threshold, computed using MELODY, as a function of the maximum phase deviation of the particle in BSM. The second harmonic case (top) is illustrated for different cutoff frequencies, f_c. The fourth harmonic case is shown at the bottom for $\mu = 0.5$ and $\mu = 1.5$. A forbidden zone with zero intensity LLD threshold is highlighted in grey where $df_s/d\phi > 0$.

at zero intensity, there are van Kampen modes already located at $\Omega = \min[f_s(\phi)]$. Therefore, the LLD occurs for any intensity, and coherent instabilities can easily be triggered. Beyond the grey zone, the derivative of the synchrotron frequency distribution versus phase is negative, $df_s/d\phi < 0$, and the minimum of the frequency distribution is again in the tail of the bunch. Similarly to the $r_h = 2$ case, a dependence on the cutoff frequency is not observed for a binomial particle distribution with $\mu = 1.5$ (diamonds), while being present for $\mu = 0.5$. Moreover, the LLD threshold exceeds the critical curve around $\phi_{\mathrm{max}} = 0.8$ rad.

When the RF systems are in counter phase at the bunch position (BLM), the LLD threshold is monotonic [26, 38, 72]. This is also confirmed by Fig. 5.11, where the LLD threshold calculated with MELODY monotonically increases with the maximum phase deviation of the particle. Note that in Fig. 5.11 (bottom), there

are phases where a jump of the LLD threshold derivative, $d\zeta/d\phi$, occurs. This is linked to the fact that upon a certain bunch length, the minimum of the synchrotron frequency distribution moves from the center to the tail of the bunch and, hence, is no longer being dependent on the cutoff frequency, as already seen for the BSM. Beyond, the LLD thresholds converge to the single RF case (brown).

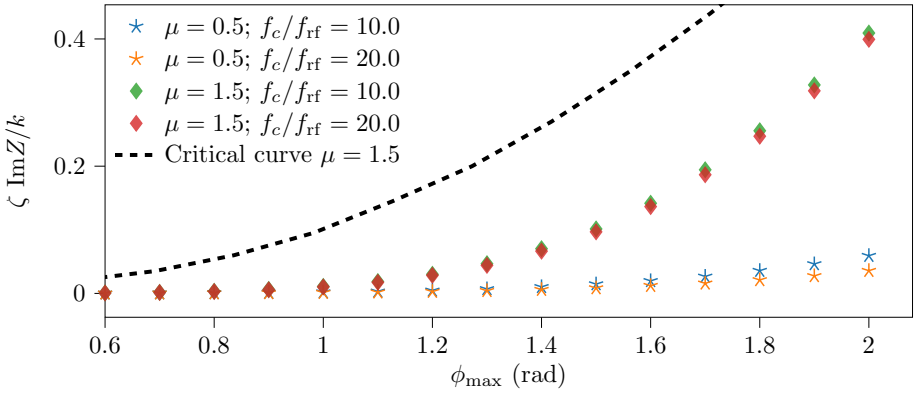

(a) $r_h = 2;\ r_V = 0.1$.

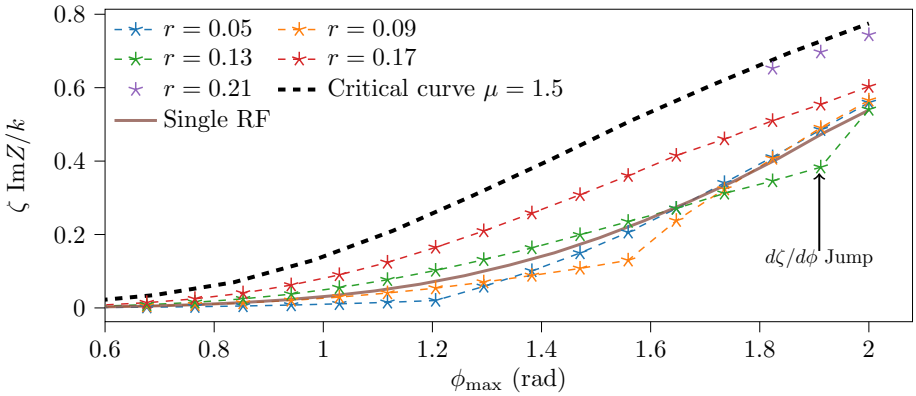

(b) $r_h = 4;\ \mu = 1.5$.

Figure 5.11. LLD threshold in BLM computed semi-analytically with the MELODY code. The case of $r_h = 2$ is illustrated for different distributions and cutoff frequencies (top). The fourth harmonic RF system, $r_h = 4$, is considered (bottom) and compared with the single RF case (solid). The black dashed line represents the critical curve for $\mu = 1.5$.

5.3 Conclusion

The chapter presented the results of the LLD threshold for all the relevant configurations of BSM and BLM when inductive impedances are involved.

In the first part, we focused on the above-transition regime (equivalent to capacitive impedance below transition), where the proposed analytical LLD threshold equation has been successfully benchmarked with the code MELODY. Further confirmation has been achieved by comparing MELODY with a macroparticle tracking simulation code in BLonD. The results of both complementary approaches agree extremely well. In particular, it has been proven that the threshold is a

monotonic function of the bunch length and that it is inversely proportional to the cutoff frequency, f_c, similarly to the single RF case [45]. Interestingly, this differs from the results of previous studies [25], where a different definition of LLD threshold, based on kick, has been applied. On the contrary, the BLM suffers from the presence of regions where $df_s/d\phi > 0$, leading to the LLD at any intensity. Furthermore, unavoidable imperfections of the relative phase represent an additional limitation, showing weak robustness with respect to relative phase shift, which can drastically reduce the threshold and make the BLM practically irrelevant.

The second part focused on the case of an inductive impedance below the transition energy (or capacitive above). The analytical upper-intensity limit (critical curve) for a binomial particle distribution was benchmarked with the semi-analytical code MELODY, reaching a very good agreement. In BSM, we observed that the LLD threshold is no longer dependent on the cutoff frequency for binomial particle distributions with binomial coefficient $\mu > 1$. This agrees with the prediction showing a non-monotonic behavior. As expected, the regions where $df_s/d\phi > 0$ led to zero thresholds. The vanishing dependency on the cutoff frequency was also observed in BLM. In addition, the monotonic behavior with respect to the bunch length is limited only by the crossing with the critical curve.

In this chapter, we provided an extensive analysis of the LLD threshold in DRF systems and its numerical evaluation, covering the most important scenario, including $\eta \mathrm{Im}Z/k > 0$ (PS, SPS, and LHC) and $\eta \mathrm{Im}Z/k < 0$ (PSB at flattop). The study can be explored individually for each accelerator using their respective impedance model, introducing the concept of effective impedance [88].

Chapter 6

Beam response from a rigid dipole kick

6.1 Introduction

The occurrence of a rigid-bunch dipole perturbation in the beam, usually referred to as a longitudinal phase kick, can be attributed to various sources, including injection phase discrepancies and energy errors, as well as fluctuations in the phase of the RF system. Investigating the beam response to a longitudinal kick is a well-established method for studying LLD through experimental measurements and simulations. It moreover allows probing effective impedance sources in an accelerator [51, 58, 89].

This section studies the impact of a dipole excitation on a single bunch for a constant inductive impedance. Furthermore, an expansion of the rigid-dipole perturbation as a superposition of van Kampen modes is used to obtain its time evolution analytically [45]. This technique is then applied to conduct beam-based measurements in the SPS and PS to estimate the LLD threshold at very different conditions in terms of bucket filling factor. The findings are compared with calculations using the MELODY code as well as macroparticle tracking simulations with BLonD.

6.2 Evolution of the bunch offset for constant inductive impedance

The bunch offset evolution after a longitudinal phase kick is simulated and tracked in time. To emulate a rigid-dipole kick, an instant shift of the bunch position by 1° is opted to avoid modification on the initial distribution. The shift was introduced at the beginning of the BLonD simulation after generating the bunch and matching it to the RF system with intensity effects (Chapter 4), assuming the accelerator parameters in Tab. 4.1. Subsequently, the evolution of the bunch is tracked for 5×10^4 turns. The simulation is performed in BSM configuration with $r_{_V} = 0.25$, $r_h = 4$ and 2×10^6 macroparticles.

Figure 6.1 illustrates the bunch centroid evolution following an initial 1° phase kick for three different bunch lengths, expressed as maximum phase deviations, i.e.,

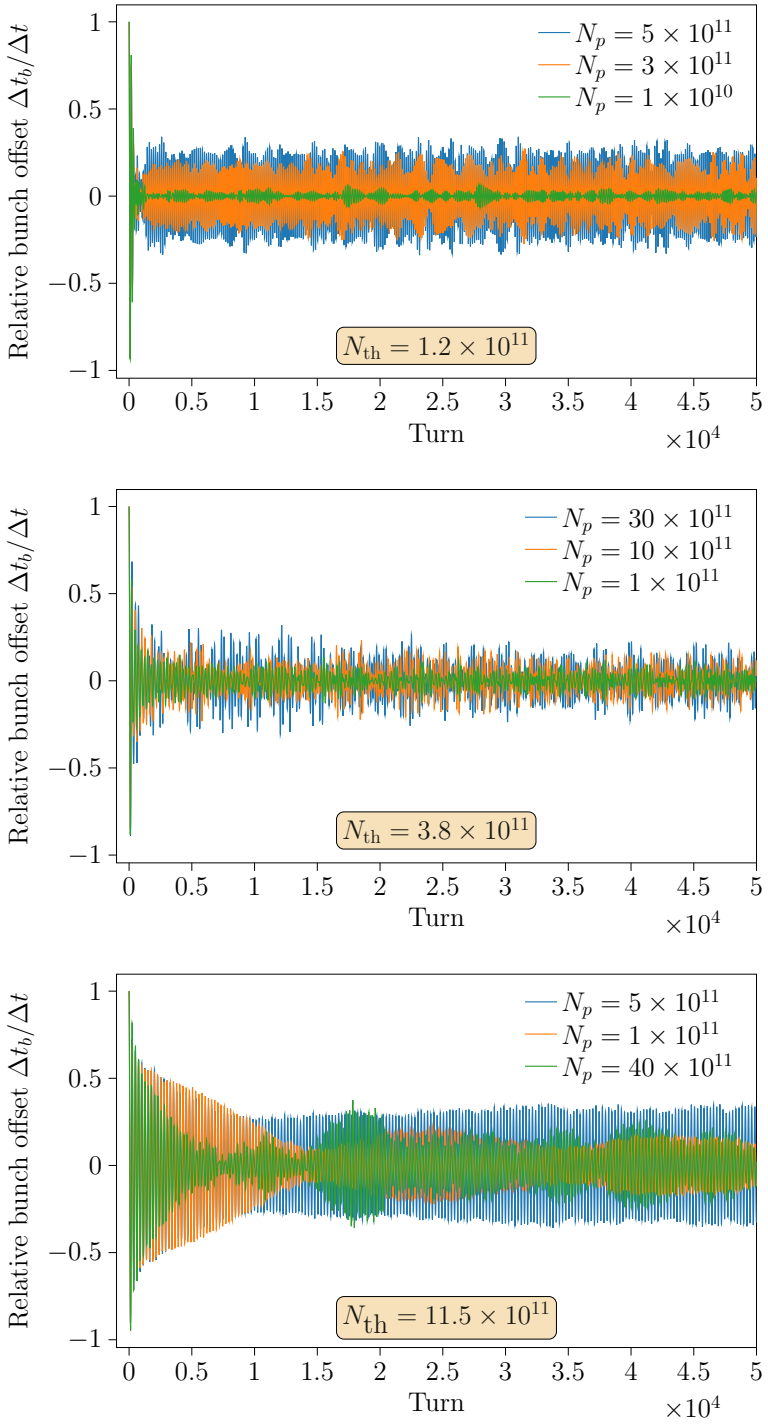

Figure 6.1. Example of the bunch offset evolution in BSM, for different intensities, following an initial dipole kick of one degree. The BLonD simulation uses $\mathrm{Im}Z/k = 0.07$ Ω, $f_c = 4$ GHz, $r_h = 4$ and $r_v = 0.25$. Three different bunch lengths, respectively for $\phi_{\mathrm{max}} = 1.0$ rad (top), $\phi_{\mathrm{max}} = 1.5$ rad (centre) and $\phi_{\mathrm{max}} = 2.0$ rad (bottom) have been considered. The LLD thresholds predicted by MELODY are displayed in the insets.

$\phi_{\max} = 1$ rad (top), $\phi_{\max} = 1.5$ rad (center) and $\phi_{\max} = 2.0$ rad (bottom). For $\phi_{\max} = 1$ rad (short bunch), the initial rapid decoherence of bunch oscillations due to the phase kick is followed by subsequent decoherence (or phase mixing), damping the amplitude oscillation of the bunch centroid when the intensity is below the LLD threshold. As explained in Chapter 2, the decoherence has the side effect of leading to emittance growth. Above the threshold, the amplitude of the bunch offset oscillation persists. However, when the bunch length is relatively large ($\phi_{\max} = 2.0$ in Fig. 6.1, bottom), the simulations reveal a counter-intuitive behavior. In particular, we observe that the damping time can be very long at low intensity (blue). The initial damping becomes faster at higher intensities, but the residual oscillation amplitude remains small (green).

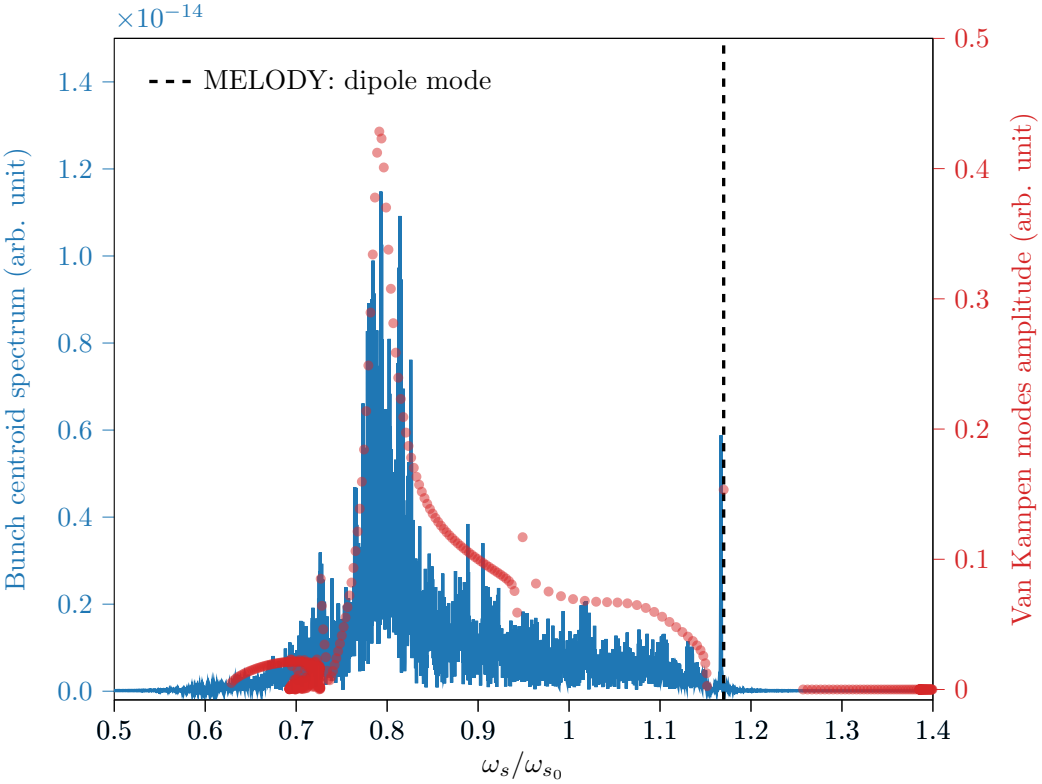

Figure 6.2. Bunch position spectrum in BLonD (blue) and Van Kampen modes in MELODY (red dots). The computations are based on Tab. 4.1 in BSM with $r_h = 4$, $r_V = 0.25$, $N_p = 4 \times 10^{12}$, $\phi_{\max} = 2$ rad, $\mu = 1.5$, and $f_c/f_{\mathrm{rf}} = 10$. The frequency of the dipole mode is highlighted in black.

This behavior can be explained in the frequency domain by analyzing the spectrum of the dipolar synchrotron frequency distribution derived from the spectrum of the bunch centroid. Taking into account the parameters in Tab. 4.1, the intensity $N_p = 4 \times 10^{12}$ and maximum phase deviation $\phi_{\max} = 2.0$ rad is beyond the flat zone (where $df/d\phi > 0$) of the synchrotron frequency distribution (Fig. 2.11) and also well above the LLD threshold. Similarly to Fig. 5.3, 2×10^6 macroparticles for 10^6 turns were tracked for a sufficiently high resolution in the frequency domain. The spectrum of the bunch centroid motion, plotted in Fig. 6.2, confirms that LLD is lost since

a coherent mode lies outside the incoherent frequency band (blue). This is also in agreement with the prediction of MELODY (black). Solving Eq. (4.7) with the same parameter as assumed for the simulation shows that the van Kampen modes (red dots) behave similarly to the bunch centroid spectrum. The amplitude of the van Kampen modes indicates the strength of the response to a phase kick. Furthermore, note a cluster of modes displaying relatively high amplitudes, around $\omega_s/\omega_{s0} = 0.8$ (flat zone of the synchrotron frequency distribution; Fig. 2.11), with respect to the coherent mode. This implies that when a perturbation is present, these van Kampen modes inside the incoherent spectrum absorb a significant portion of the energy. As a result, this contributes to reducing the residual amplitude oscillation, as seen in Fig. 6.1.

6.3 Rigid-dipole kick as a superposition of van Kampen modes

Van Kampen demonstrated that an arbitrary perturbation of the distribution in a plasma can be described as a superposition of waves [42]. Equation (2.95) is equivalent to the expression describing collective modes in plasma physics [9, 42]. In the present section, the expansion of a rigid-dipole perturbation on the basis of van Kampen modes to analytically derive its time evolution is applied. It is worth noting that the same method has also found applications in characterizing the transverse oscillations of colliding bunches [90]. This versatile approach can also be adapted for the analysis of higher-order perturbations such as quadrupolar oscillations and beyond.

Once the eigenvectors and eigenvalues of Eq. (4.8) have been founded, we can express the bunch offset evolution as follows (the detailed derivation in [41, 45]):

$$\Delta\phi_b(t) = \kappa \sum_{m=1}^{m_{\max}} \sum_{n=1}^{N_{\mathcal{E}}} \alpha_{mn} \int_{-\phi_{\min}(\mathcal{E}_{\max})}^{\phi_{\max}(\mathcal{E}_{\max})} \phi \tilde{\lambda}\left(\phi, \Omega_{mn}\right) \cos\left(\Omega_{mn} t\right) d\phi \,, \tag{6.1}$$

where α_{mn} is a coefficient expansion defined as

$$\alpha_{mn} = \sum_{m'=1}^{m_{\max}} \sum_{n'=1}^{N_{\mathcal{E}}} K^{-1}_{nmn'm'} C^{\mathrm{rd}}_{m'}\left(\mathcal{E}_{n'}\right) \,, \tag{6.2}$$

and the normalization factor κ is proportional to the initial phase offset $\Delta\phi$. The matrix K^{-1} in Eq. (6.2), is the inverse matrix constructed with the eigenvectors $C_m(\mathcal{E}_n, \Omega_{m'n'})$ computed in Eq. (4.8). Furthermore, assuming only the dipole mode ($m = 1$), the following approximation holds: $C^{\mathrm{rd}}_m(\mathcal{E}) \approx \sqrt{\mathcal{E}}\mathcal{F}'(\mathcal{E})$ [45].

In Fig. 6.3, we compare the results of Eq. (6.1) (red) and the bunch offset evolution simulated in BLonD (blue) for 10^6 macroparticle and kick strength of one degree. Results obtained from Eq. (6.1) match very well those obtained with the tracking code. This approach was also adopted in [45], reaching the same level of agreement for different configurations.

In the following Chapters, we will use this approach to benchmark beam-based measurements in the SPS and PS to estimate the LLD threshold at very different conditions in terms of bucket filling factor. The measurements are again compared with calculations using the MELODY code and macroparticle tracking in BLonD.

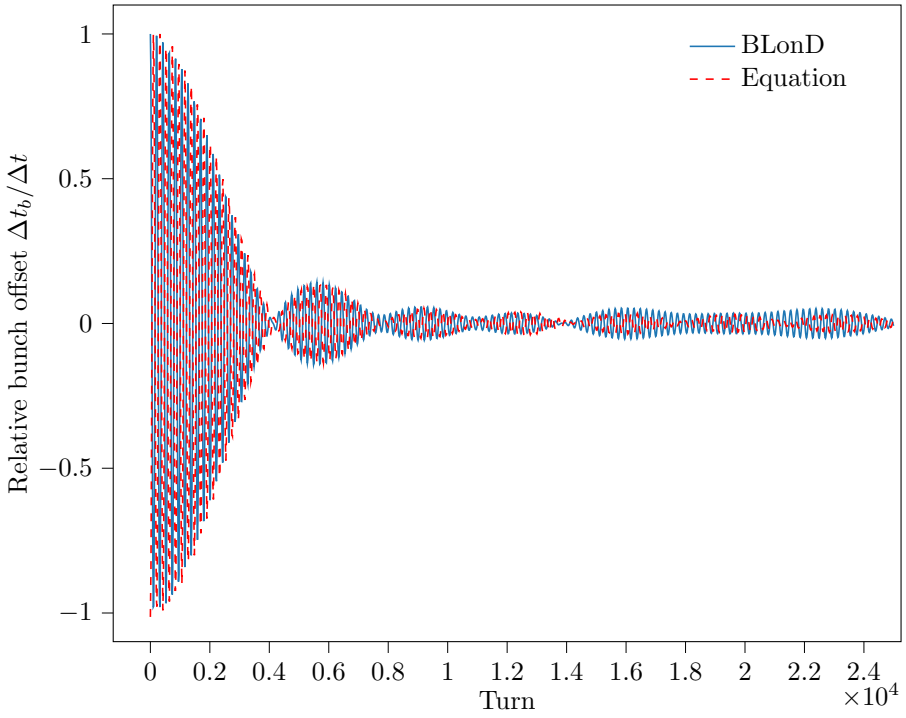

Figure 6.3. Comparison between the bunch offset evolution simulated in BLonD and calculated with Eq. (6.1), for a single RF system considering $\phi_{\max} = 1$ rad, $\mu = 1.5$, intensity $N_p = 2 \times 10^6$ and accelerator parameters illustrated in Tab. 4.1.

6.4 Conclusion

A crucial aspect of understanding LLD involves evaluating how the beam responds to the rigid-dipole perturbation (longitudinal kick), potentially resulting in undamped bunch oscillations. In order to reconstruct the evolution of the bunch offset, the perturbation was expanded using van Kampen modes as a basis and, subsequently, traced in the time domain. Our findings demonstrate that this method agrees very well with the macroparticle tracking code BLonD.

Simulations that required a large number of macroparticles, 2×10^6, and sufficient slicing in the induced voltage calculations to cope with the numerical noise show that bunches below the LLD threshold are quickly damped as predicted. Exceptions for long bunches have been observed, for which, counter-intuitively, bunches with a higher intensity above the LLD threshold are damped more than those below the threshold. This behavior is understood by expanding the perturbations on the basis of van Kampen modes, indicating the strength of response to a rigid-dipole kick is larger inside the incoherent band. Thus, modes belonging inside the incoherent mode can decohere and reduce the oscillation amplitude of the bunch centroid.

Chapter 7

Beam measurements in the Super Proton Synchrotron at 200 GeV

With a circumference of 6.9 km, the SPS is the largest injector synchrotron at CERN, which operates with four traveling wave 200 MHz cavities structures as the primary RF system and two traveling wave cavities at 800 MHz, four times the fundamental RF frequency. The high harmonic RF system plays a crucial role as a Landau RF system in the SPS to counteract longitudinal instabilities and stabilize the high-intensity proton beam for the LHC.

Before the LS2, for the original nominal LHC beam intensity of 1.15×10^{11} p/b, the beam in the SPS was affected by longitudinal instabilities occurring during the acceleration ramp, already with a single bunch and small longitudinal emittance [15]. Extensive studies have confirmed that both RF systems must operate in the BSM throughout the entire cycle to ensure a high-quality beam for extraction to the LHC [20, 25]. Furthermore, in view of the HL-LHC, SPS has to reach the intensity target of $N_p = 2.3 \times 10^{11}$ p/b at extraction. In this intensity range, the LLD can pose an important performance limitation.

This chapter presents measurements for a single bunch at 200 GeV in a single harmonic RF system. Through exciting the bunch with a longitudinal dipole kick and after the initial decoherence, we observe at what intensity the bunch offset oscillations in the rigid bucket are undamped due to the LLD. We will moreover analyze the configuration with the fourth-harmonic RF system employed (800 MHz) in BSM to prove the benefit of a higher-harmonic RF system in terms of beam stability. Based on the latest SPS impedance model, the findings are compared to calculations using the semi-analytical code MELODY and macroparticle tracking with BLonD.

7.1 Longitudinal coupling impedance model

In the framework of the LHC Injectors Upgrade (LIU) project [91], the SPS has undergone massive improvements, including impedance reduction [92, 93], new beam and cavity control as well as feedback systems [94, 95]. Refined electromagnetic sim-

ulations and measurements provided an updated longitudinal impedance model [96]. A realistic simulation model of the beam-based low-level RF (LLRF) loops was developed and implemented in BLonD, allowing the study of the longitudinal stability for high-intensity LHC-type beams in the SPS with high accuracy [78].

The present SPS impedance model used for the calculations and beam dynamics simulations is illustrated in Fig. 7.1 with its real (top) and imaginary (bottom) parts. The bunch length in the SPS ranges typically from 1.5 ns to 3 ns. Consequently, the frequency range of the stable bunch spectrum is within 1 GHz. Nonetheless, the frequency range of up to 5 GHz was considered to take into account the effects of high-frequency impedance. The impedance is composed of narrow and broad resonances. The most relevant contributions come from the 200 MHz and 800 MHz traveling wave structures [98, 99], the injection/extraction kickers [100, 101], and the vacuum flanges [102].

7.2 Experiment setup and main parameters of the SPS

Table 7.1 summarizes the principal accelerator parameters used for the measurements.

Table 7.1. Accelerator parameters of the SPS at flat-top.

Parameter	**Unit**	**Value**
Circumference, $2\pi R$	m	6911.55
Beam energy, E	GeV	200
Main harmonic number, h		4620
Main RF frequency, f_{rf}	MHz	200.39
RF voltage at main harmonic, V_{rf}	MV	4.5
Frequency of the 4^{th} harmonic RF system	MHz	800
RF voltage of the 4^{th} harmonic RF system	kV	450

LHC-type beams, including single bunches, are accelerated in the SPS from 26 GeV to 450 GeV. At flat bottom, the longitudinal space charge impedance is $(\mathrm{Im}Z/k)_{\mathrm{sc}} \approx -1\ \Omega$ scaling as $(\mathrm{Im}Z/k)_{\mathrm{sc}} \propto 1/\gamma^2$. Thus, its amplitude decreases during acceleration, reaching the minimum at flattop. In particular, it has been shown that above an energy of 80 GeV, the space charge becomes negligible [14].

Therefore, to minimize the space charge contributions of the impedance and to allow a wider acquisition window due to the longer plateau, after injecting a single bunch from the PS at a total energy of 26 GeV, the beam is accelerated to an energy of 200 GeV (Fig. 7.2) A few milliseconds after arrival at flat-top energy, the bunch is excited by a dipole kick (green line), allowing it to oscillate in a rigid bucket. The beam phase loop [103] was disabled right before the kick as it would correct the RF phase after the dipole excitation, damping rapidly the phase offset oscillation. The grey zone in Fig. 7.2 highlights the time windows in which the main acquisitions have been performed.

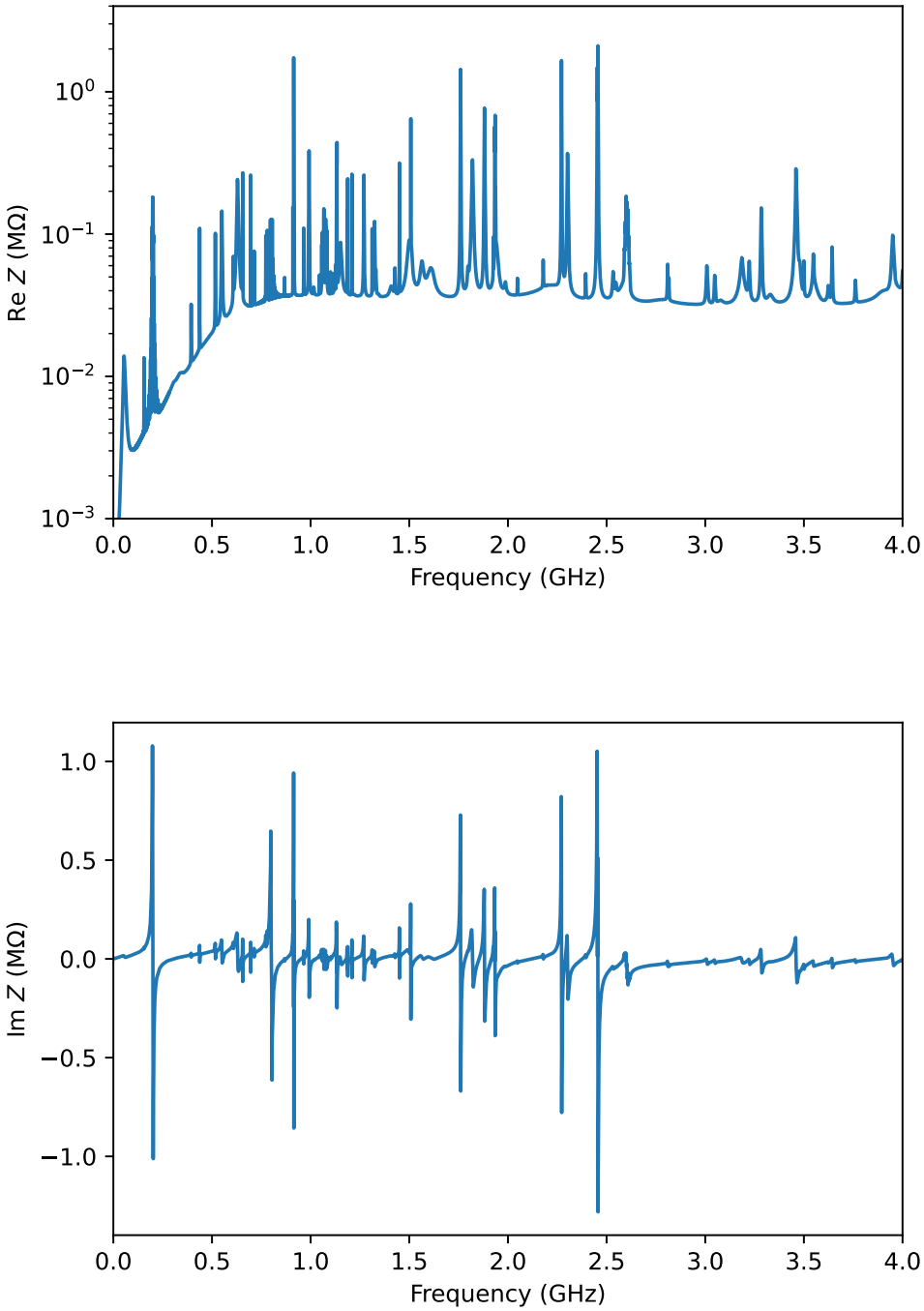

Figure 7.1. Real (top) and imaginary (bottom) part of the SPS impedance model after the impedance reduction campaign during the 2019 – 2021 long shutdown (LS2) [97].

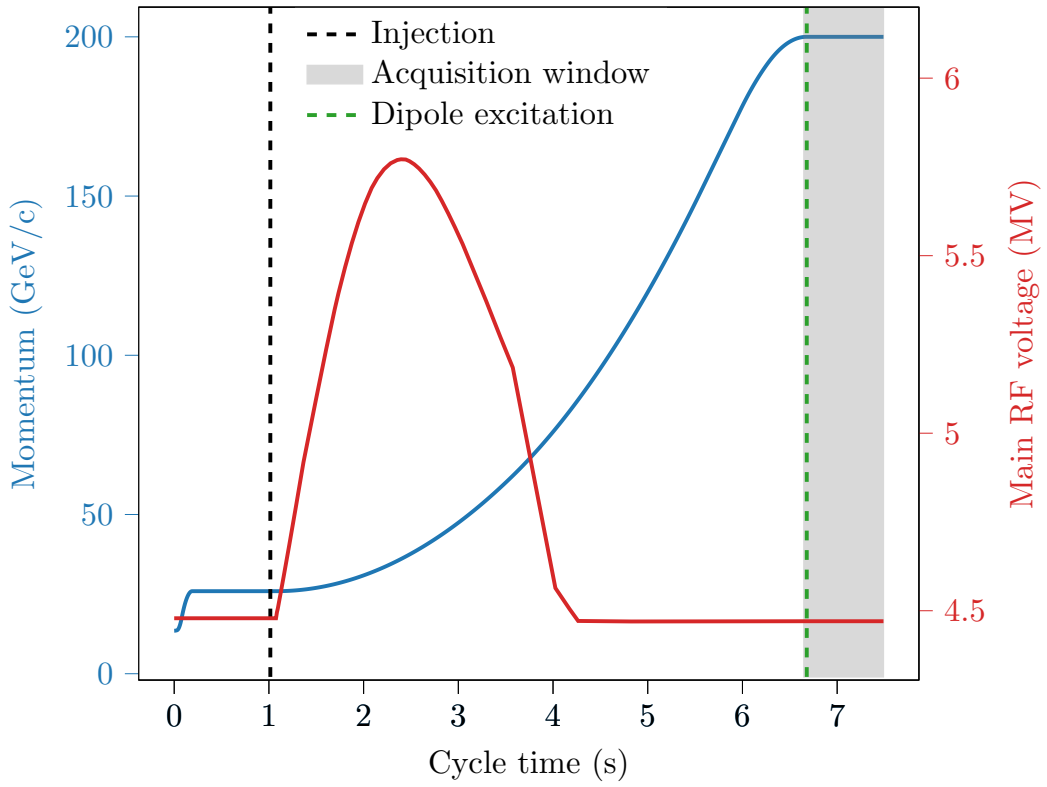

Figure 7.2. Momentum ramp (blue) and voltage program of the main RF system (red) in the SPS cycle used for the beam measurements. The dashed lines indicate the injection (black) and the phase kick (green). The acquisition time window is highlighted in grey.

7.3 Beam-based measurement in single RF

As a reference case, the main RF system (200 MHz) is considered, neglecting for the moment the voltage contribution due to the 800 MHz RF system. The evolution of the bunch offset is obtained by measuring the relative phase difference between the beam pickup signal and the sum of the cavity voltages (i.e., phase-loop error [95]). Figure 7.3 illustrates that after the phase excitation, beams with low intensity (blue line), the bunch phase oscillations rapidly lose their coherence, followed by subsequent slower decoherence. This means we are below the LLD threshold. Above the threshold, the phase oscillations persist (orange line), with their amplitudes dependent on the intensity of the bunch. This dependence of the residual oscillation with the intensity is attributed to crossing the LLD threshold. Below this intensity threshold, damping is dominant.

The measurements cover many bunch intensities ranging from 3.0×10^{10} to 7.0×10^{10}, in increments of $\sim 0.5 \times 10^{10}$. Figure 7.4a shows the measured time evolution of the bunch phase oscillation amplitudes (color coding), following a dipole excitation (at 0 s), and kick amplitude of 5°, for different intensities. A Hilbert transform [104] has been performed for each acquisition to obtain the amplitude of the phase oscillations (Fig. 7.3). Note that below $N_p = 5 \times 10^{10}$ (white region), the amplitude is rapidly damped, indicating that the intensity is below the threshold of

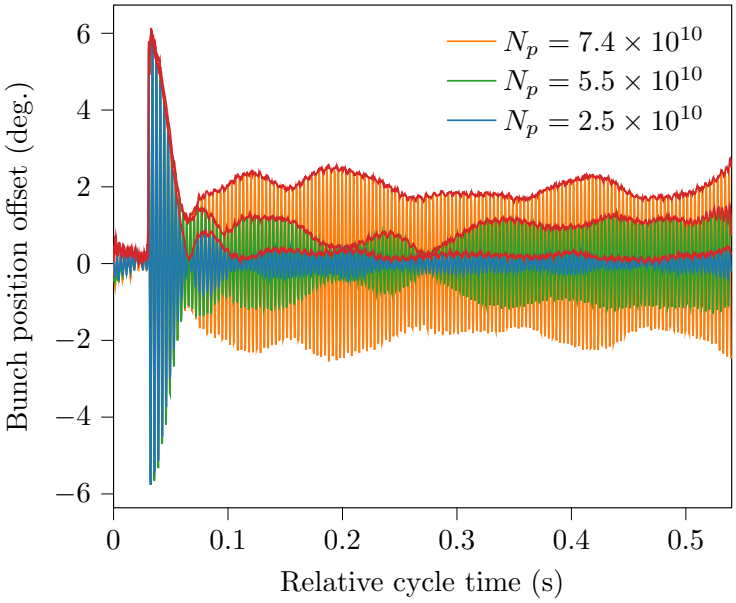

Figure 7.3. Bunch phase offset evolution with different intensities obtained measuring the phase-loop error in single RF. The envelopes of the traces (red) have been computed using a Hilbert transform [104].

LLD.

To simulate the bunch offset oscillation in the SPS under the same measured beam conditions, we developed a fitting algorithm. The code generates a matched bunch with the RF system, including collective effect, from a binomial distribution according to Eq. (2.62) using as a first guess an arbitrary full bunch length, τ_{full} and μ. The line density λ^{fit}, is then compared with the measured bunch profile,λ^{SPS}, by computing the following loss function:

$$\mathcal{L} = \frac{1}{n} \sum_{i=0}^{n} \left(\lambda_i^{\text{SPS}} - \lambda_i^{\text{fit}} \right)^2 , \tag{7.1}$$

where n is the array total length of the line densities. The procedure is iteratively repeated in order to identify the binomial parameters, τ_{full} and μ, that minimize the loss function in Eq. (7.1). We opted for Powell's method [105] as an algorithm to find loss function minima in two dimensions. From our observation, it provides a reasonable compromise between time consumption and precision. Figure 7.5 demonstrates the good performance of the algorithm, displaying a very good agreement between the measured line density and the fit (intensity effects included).

The fitted profile is subsequently provided as input to BLonD, simulating the evolution of 10^6 macroparticles after a phase kick of 5°. The fitting and simulations were repeated to cover the same intensity range as in measurement. A Hilbert transform has been performed to obtain the bunch offset amplitude oscillation, as illustrated in Fig. 7.4b.

In the MELODY code, we use the identical fitted lined density as used in BLonD. Using the Oide-Yokoya method, we found the eigenvalues and eigenvectors of the matrices (4.8). This allows us to reconstruct the bunch offset evolution using Eq. (6.1)

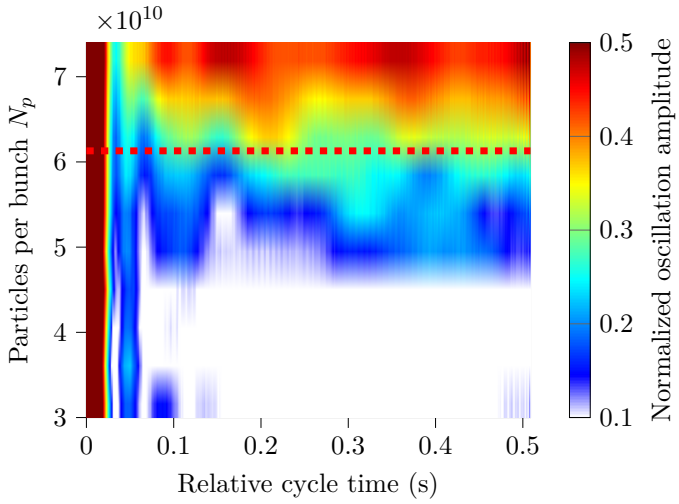

(a) Measurement.

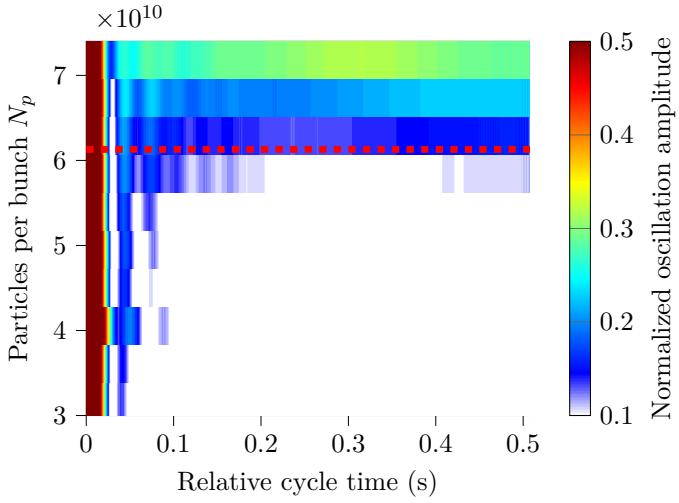

(b) BLonD.

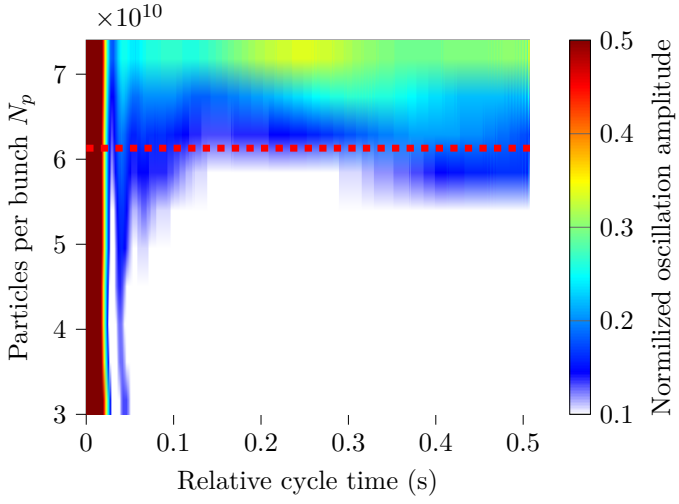

(c) MELODY.

Figure 7.4. Time evolution of the normalized bunch phase oscillation amplitude (color coding) after a dipole excitation in the single RF. The measurement results (top) are compared with the outcome of BLonD (middle) and MELODY (bottom) analysis for different intensities. The MELODY prediction of the LLD threshold at $N_{\mathrm{th}} \approx 6.1 \times 10^{10}$ is shown in a red dashed line.

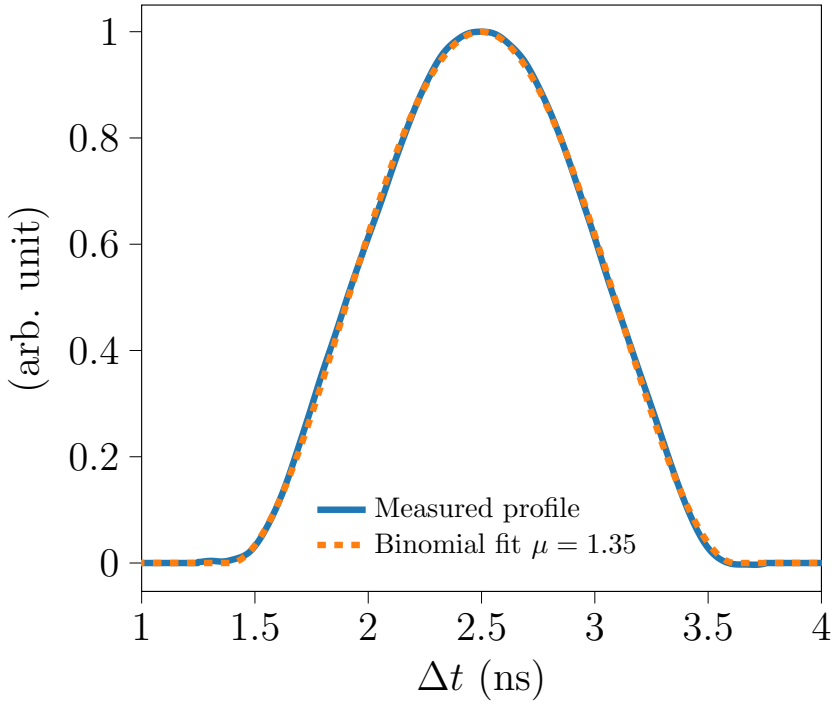

Figure 7.5. Comparison between measured line density in the SPS and the binomial fit (2.64) (orange) in single RF for an intensity of $N_p = 4 \times 10^{10}$.

and displayed in Fig. 7.4c. Both numerical methods assume accelerator parameters according to Table 7.1, including the SPS impedance model illustrated in Fig. 7.1. The two approaches exhibit similar behavior and agree well with the LLD threshold predicted by MELODY (red dashed line). However, the residual oscillation amplitude depicted by measurement in Fig.7.4a results in being larger than from the simulations. The resulting LLD threshold predictions of $N_{\text{th}}^{\text{SRF}} = 6.13 \times 10^{10}$, computed in MELODY using the Oide-Yokoya method, overestimates the measurements. Overall, it agrees well.

The SPS impedance model was developed for many years based on measurements and simulations of accelerator components [106, 107]. Nevertheless, obtaining accurate impedance behavior at high frequencies presents significant challenges. As illustrated by Eq. (3.20), the LLD threshold highly depends on the cutoff frequency f_c. Consequently, inaccuracies in the impedance model or in its cutoff frequency have a significant impact on the computed LLD threshold.

7.4 Measurements in bunch shortening mode

Let us include the voltage contribution coming from the 800 MHz in BSM (200 MHz and 800 MHz in phase). This represents the operational configuration used for LHC-type and fixed target beams. Therefore, it represents a more relevant case of study with respect to the single RF.

We evaluate the relative change of the LLD threshold when transitioning from a single to a double-harmonic RF system, considering the voltage ratio of $r_V = 0.1$.

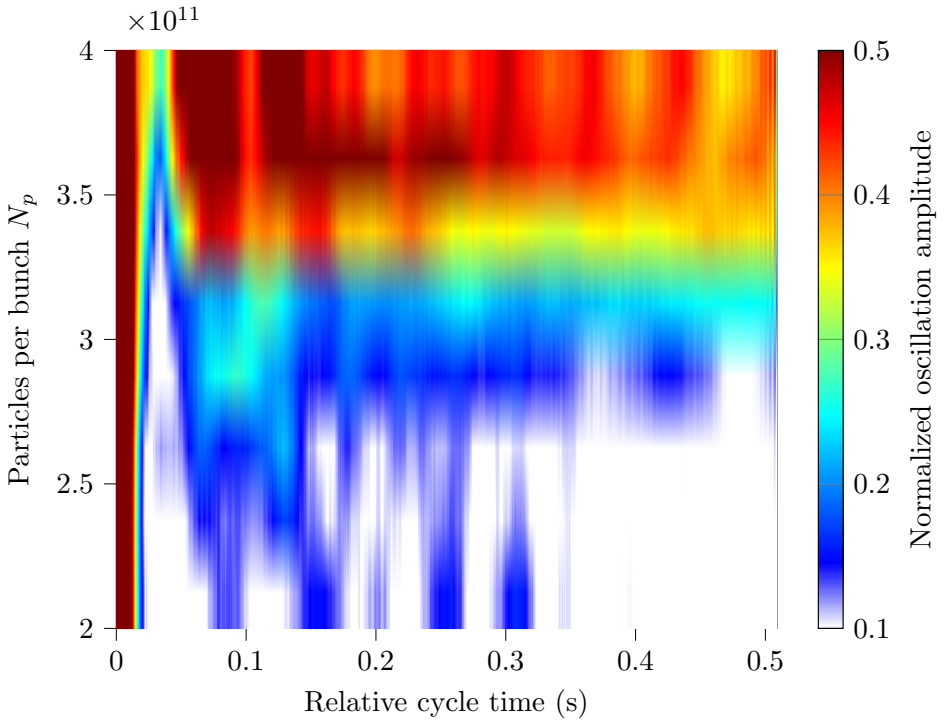

Figure 7.6. Measured time evolution of the bunch phase oscillation, normalized by the kick strength, in BSM ($r_h = 4$) for different intensities with voltage ratio $r = 0.1$.

This ensures the monotonicity of the synchrotron frequency distribution, avoiding issues coming from the inflection points $df_s(\phi)/d\phi = 0$ (see Chapter 5). We conduct similar measurements as illustrated in the preceding section.

The result is presented in Fig. 7.6, where the time evolution of the normalized bunch phase oscillation amplitude, relative to the kick strength, is measured. A strong enhancement can be observed when employing the 800 MHz RF system. The bunch offset oscillations are damped at a much higher intensity than the single RF case shown in Fig. 7.4a. In particular, employing BSM leads to an increase of approximately ~ 6 in terms of the LLD threshold. However, it must be pointed out that direct comparison is not straightforward since emittance and bunch distribution at significantly higher intensities differ. This is confirmed by the measured bunch profile in Fig 7.7 which is plotted together with its corresponding binomial fit (2.64) in orange. In particular, moving from the single RF scenario (left) to the BSM case (right), it is visible a reduction in bunch length and a noticeable change in bunch shape (lower μ). Furthermore, in BSM, we observe a discrepancy on the tail of the line density, suggesting the distribution is not entirely binomial.

We computed the LLD in MELODY based on the fitting performed on the measured line density. The predicted threshold in BSM is, similarly to the single RF case, overestimated, and it corresponds to $N_{\text{th}}^{\text{BSM}} \approx 77 \times 10^{10}$. Compared to single RF, it is a gain factor of ~ 12.

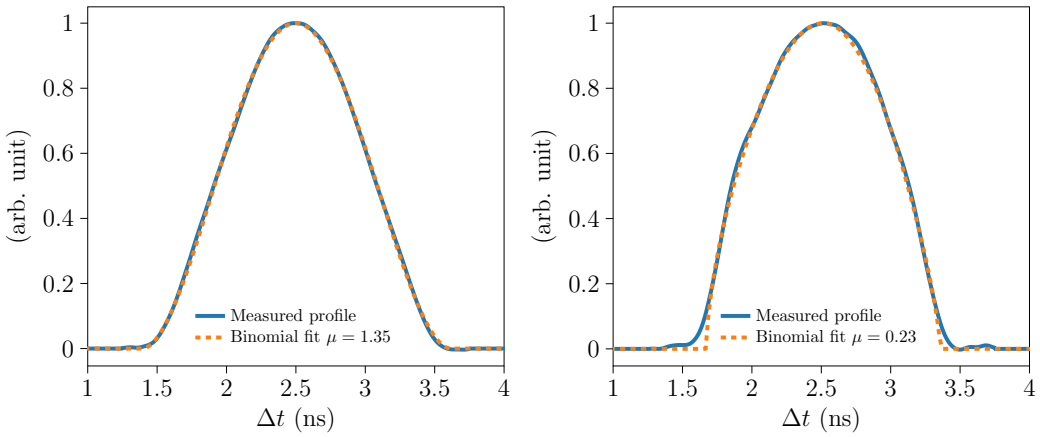

Figure 7.7. Comparison between measured line density in single RF (left) and BSM (right). The binomial fit (2.64) of the profile is depicted in orange.

7.5 Conclusion

The kick-response technique was applied during an extensive campaign of beam measurement in the SPS for the LLD threshold study. The findings demonstrate that the theoretical approach outlined in the previous chapter remains applicable for beam-based measurements. We study as a reference the single RF case neglecting the voltage contribution due to the 800 MHz RF system. In particular, we accelerated a single bunch up to 200 GeV, minimizing space charge contribution in the impedance. We injected a dipole excitation and let the bunch free to oscillate, deactivating the phase-loop. Following the initial decoherence, the amplitude oscillation of the phase offset was extracted by means of a Hilbert transform and then compared across a broad spectrum of intensities. We observed that the oscillations are not damped beyond a certain intensity, meaning the LLD occurred.

A refined algorithm, based on Powell's method, allowed to find a binomial fit for the measured line density with intensity effect included. The fitted line density, together with the SPS impedance model, was used as an input for the semi-analytical code MELODY and macroparticle simulation BLonD. Both methods exhibit excellent agreement. However, discrepancies between the measurements and simulations may indicate imperfections in the SPS beam coupling impedance model. Overall, the predictions are extremely close.

We extended the study to the most relevant case by including in the measurement the voltage contribution coming from the 800 MHz RF system in BSM. We performed a complete intensity scan in measurement, proving the threshold increases for double-harmonic RF configurations with a gain factor of 6. We performed the binomial fitting, showing that direct comparison with the single RF was not possible due to the different distributions and longitudinal emittance. The semi-analytical prediction overestimates the measurement similarly to the single RF case. Overall, the fourth harmonic RF system showed an enormous improvement with respect to the single RF case damping coherent oscillation at much higher intensities.

Chapter 8

Measurements of loss of Landau damping in the CERN Proton Synchrotron

The Proton Synchrotron (PS) is the second largest injector synchrotron at CERN with a circumference of 628 metres, accelerating proton beams up to energy of 26 GeV. It is equipped with several RF systems, operating at frequencies 2.8 MHz-10 MHz, 20 MHz, 40 MHz, 80 MHz, and 200 MHz, dedicated to both accelerating and performing the necessary RF manipulations required for the production of LHC-type beam.

The large number of RF systems makes the PS an ideal accelerator for LLD studies at different beam and RF configurations. Following the same technique performed in the SPS (Chapter 7), beam-based measurements are presented with accelerator parameters specified in Table 8.1. Special attention to the DRF case is paid by studying the cases of harmonic number ratio $r_h = 2$ and $r_h = 4$, in BLM and BSM. The low frequency of the RF systems allows the reproducibility and good control of both RF and beam parameters. We examine the scaling factor in the LLD threshold expression Eq. (3.22), which we provide below for convenience:

$$N_{\mathrm{th}} \propto \frac{1 + r_{_V} r_h^3}{(1 + r_{_V} r_h)^{1/2}} \tau_{\mathrm{full}}^4 \,. \tag{8.1}$$

In what follows, we will illustrate how Eq. (8.1) can be employed to evaluate the relative change of the LLD threshold moving from a single RF to a DRF system for the case of the BSM.

Following the injection of a single bunch from the PS Booster at a kinetic energy of 2 GeV, the beam was accelerated to the maximum energy of 26 GeV. The flat-top energy was chosen to minimize any contribution of space charge. Few milliseconds after reaching the flat-top energy, the second RF system (20 MHz or 40 MHz) was activated (Fig. 8.1). The bunch was then excited by a dipole kick (phase jump) with all beam control loops disabled. Thereafter, the bunch oscillates in a rigid bucket. The evolution of the bunch profile with respect to a beam synchronous trigger is obtained. A bunch of trigger pulses is generated each of them separated by an integer number of turns, starting just before the excitation. The bunch position

Table 8.1. Main PS parameters for LHC-type beams [11] at flat-top.

Parameter	Unit	Value
Circumference, $2\pi R$	m	628.32
Beam energy, E_0	GeV	26
Fundamental harmonic number, h		21
Fundamental RF frequency, f_{rf}	MHz	10
RF voltage at fundamental harmonic, V_0	kV	200
RF voltage at 2^{nd} harmonic (20 MHz)	kV	(up to) 40
RF voltage at 4^{th} harmonic (40 MHz)	kV	(up to) 200

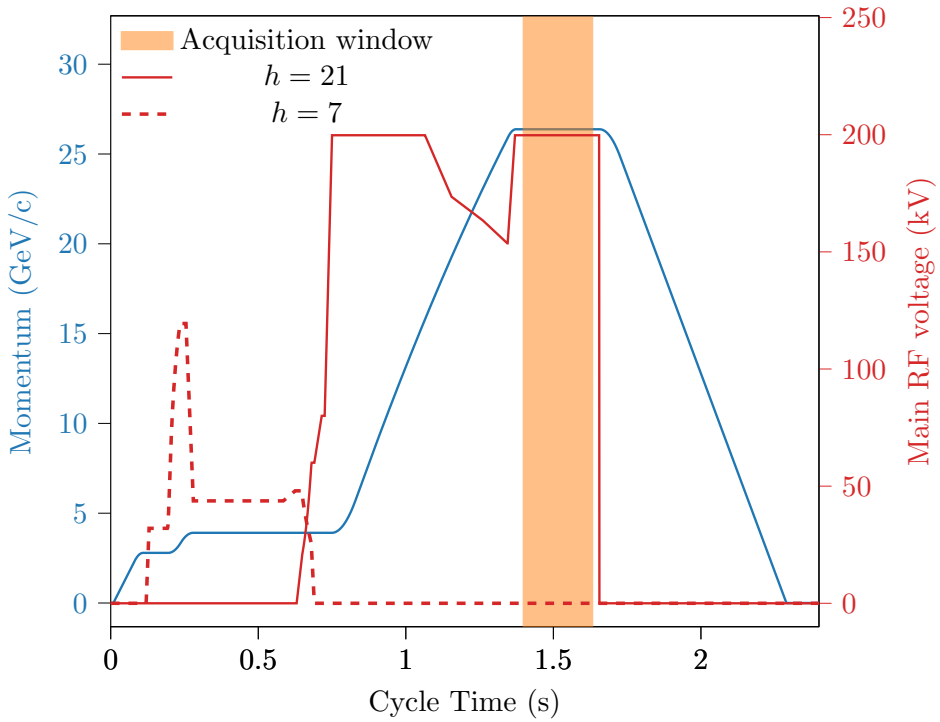

Figure 8.1. PS momentum ramp (blue) and voltage program of the fundamental RF system (red). The voltage of the cavities operating on the harmonic numbers of $h = 7$ and $h = 21$ are highlighted in dashed and solid lines, respectively. The acquisition time window is indicated in orange.

evolution can be extracted by computing the centroid of the acquired profiles with respect to the trigger, as illustrated in Fig. 8.2.

Again, we observed that when the beam intensity remains below the LLD threshold, the bunch offset oscillation slowly damps due to decoherence. However, residual phase oscillations persist above this threshold, and their amplitudes are directly proportional to the bunch intensity.

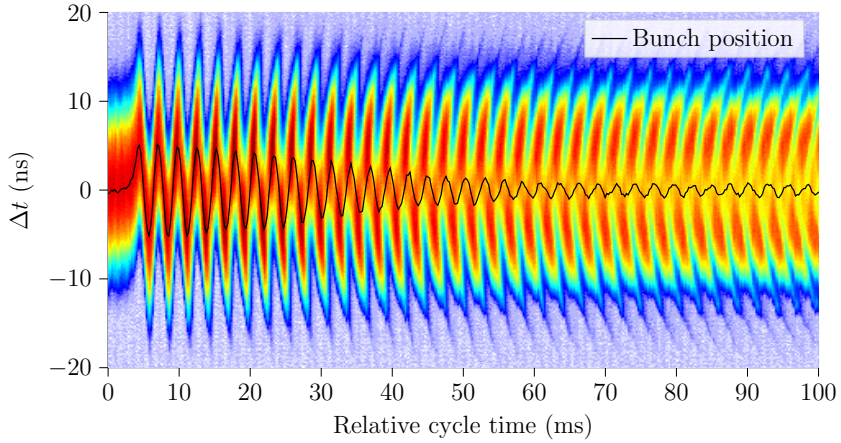

Figure 8.2. Typical line density waterfall obtained from an RF-synchronous multi-trigger acquisition in the PS for the single RF configuration at an intensity of $N_p = 0.35 \times 10^{12}$. The solid black line indicates the bunch position evolution. One frame is recorded every 110 turns.

8.1 Second harmonic RF system

The PS is equipped with two 20 MHz cavities, out of which only one is actively used during operation (the second being a spare) when required. Each cavity comprises two RF gaps, allowing for a maximum total of 20 kV [108]. To reach a sufficient voltage ratio of $r_V = 0.2$, both cavities were pulsed simultaneously.

Employing the 20 MHz as a second harmonic RF system in BSM ($r_h = 2$), the measurements started acquiring different bunch intensities spanning from 0.27×10^{12} to 1.0×10^{12} in intensity steps of $\sim 0.1 \times 10^{12}$. Binomial fits based on Eq. (2.64) have been performed to the measured line densities in order to determine the exact full bunch length, τ_{full} before the phase kick. Furthermore, the line density centroid was calculated for each frame to obtain the bunch phase offset evolution until beam extraction.

According to Eq. (8.1), the threshold varies significantly with the bunch length, and special care was therefore taken to keep it independent of intensity. Indeed, excellent reproducibility of the bunch length versus intensity for both single RF and BSM with different voltage ratios has been reached, as illustrated in Fig. 8.3. It summarizes the mean values of the full bunch lengths and their 95% confidence intervals for each bunch intensity.

Similarly to Sec. 7.3, Figs. 8.4-8.7 show the time evolution of the bunch phase oscillation amplitude (color coding) after a dipole excitation scanning different intensities. In single harmonic RF (Fig. 8.4), we observed that for low intensity, after the dipole excitation (at time zero), the normalized amplitude oscillation gradually decreases until it is fully damped (white regions). Increasing the intensity, the oscillation amplitude persists, indicating that LLD occurred. Furthermore, note that as the intensity increases, the frequency of the crest oscillations (dark shades) amplifies.

Let us consider the voltage contribution of the 20 MHz RF system in BSM. Figures 8.5-8.7 show the normalized bunch offset oscillation for voltage ratios $r_V =$

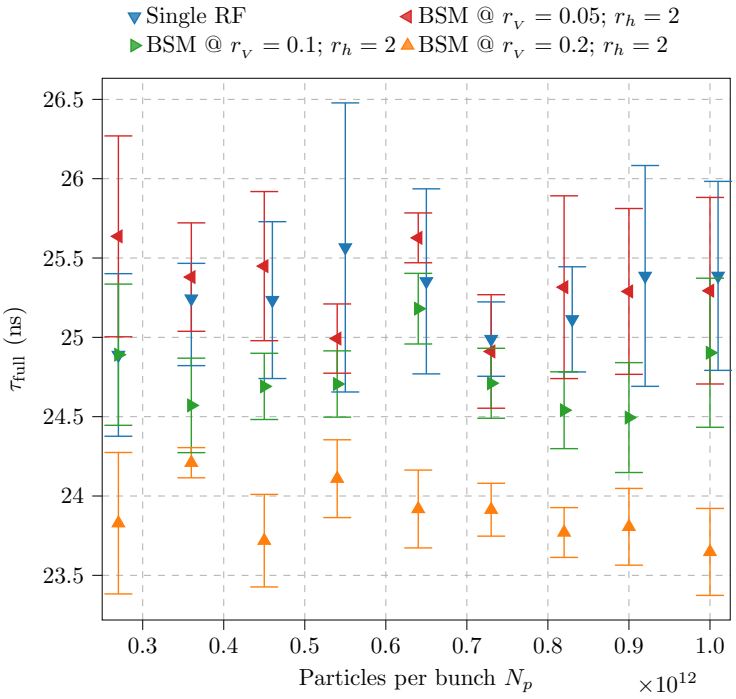

Figure 8.3. Mean values of the full bunch lengths of multiple measurements and their 95% confidence intervals for LHC-type single bunches in the PS. The experimental configuration includes single RF and BSM cases, scanning different intensities. The colors highlight the different voltage ratios.

0.05, $r_V = 0.1$ and $r_V = 0.2$ respectively, covering the same intensity range as in single RF. We observe that the oscillation amplitudes are damped at higher intensities with respect to the single RF. This enhancement scales proportionally with the voltage ratio, r_V. Moreover, also the damping time decreases accordingly. Overall, we observe an improvement of almost a factor ~ 2 transitioning from single RF (Fig. 8.4) to BSM with harmonic number ratio of $r_h = 2$ and voltage ratio of $r_V = 0.2$ (Fig. 8.7).

8.1.1 LLD threshold equation benchmarking in second harmonic RF configuration

Assuming that the LLD threshold in SRF is $N_{\text{th}} \approx 0.36 \times 10^{12}$ (black dashed line in Fig. 8.4) we can employ the Eq. (8.1) to predict the threshold of the other configurations, including the variation of the bunch length, namely: $N^{\text{BSM}}_{\text{th},r=0.05} = (0.48 \pm 0.06) \times 10^{12}$ (Fig. 8.5); $N^{\text{BSM}}_{\text{th},r=0.10} = (0.53 \pm 0.05) \times 10^{12}$ (Fig. 8.6); $N^{\text{BSM}}_{\text{th},r=0.20} = (0.63 \pm 0.08) \times 10^{12}$ (Fig. 8.7). The results, summarized in Tab. 8.2, agree very well with the measurements, demonstrating the consistency of the scaling factor of Eq. (8.1), derived in Chapter 3.

Moving to BLM, changing the relative phase to $\pm\pi$ rad, we have seen that the Landau damping is significantly affected by the lower synchrotron frequency spread modified by collective effects. As shown in Fig. 8.8 for the $r_h = 2$ case (blue),

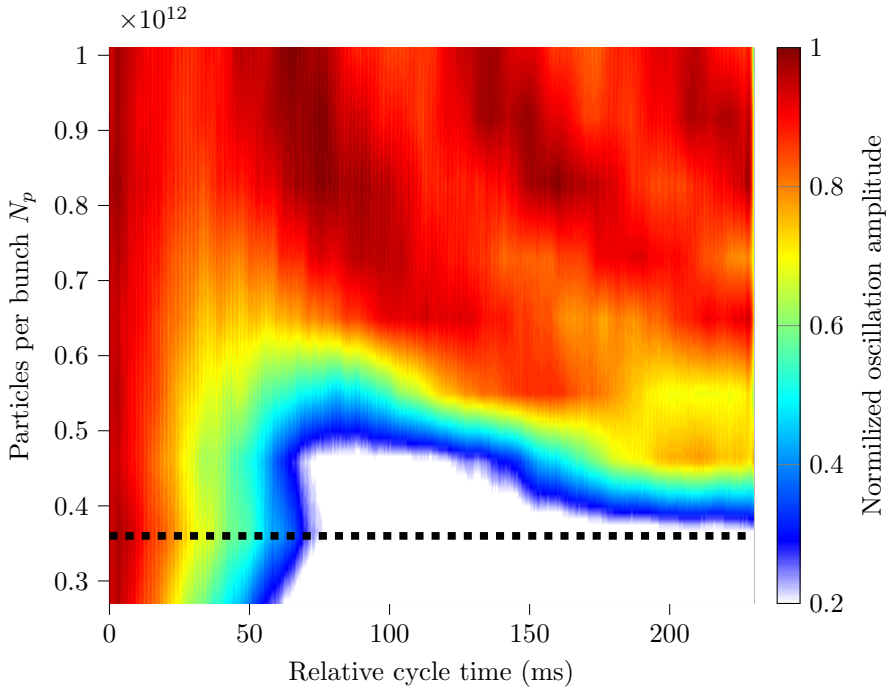

Figure 8.4. Time evolution of the normalized bunch phase oscillation amplitude (color coding) for different intensities after a dipole excitation in single harmonic RF.

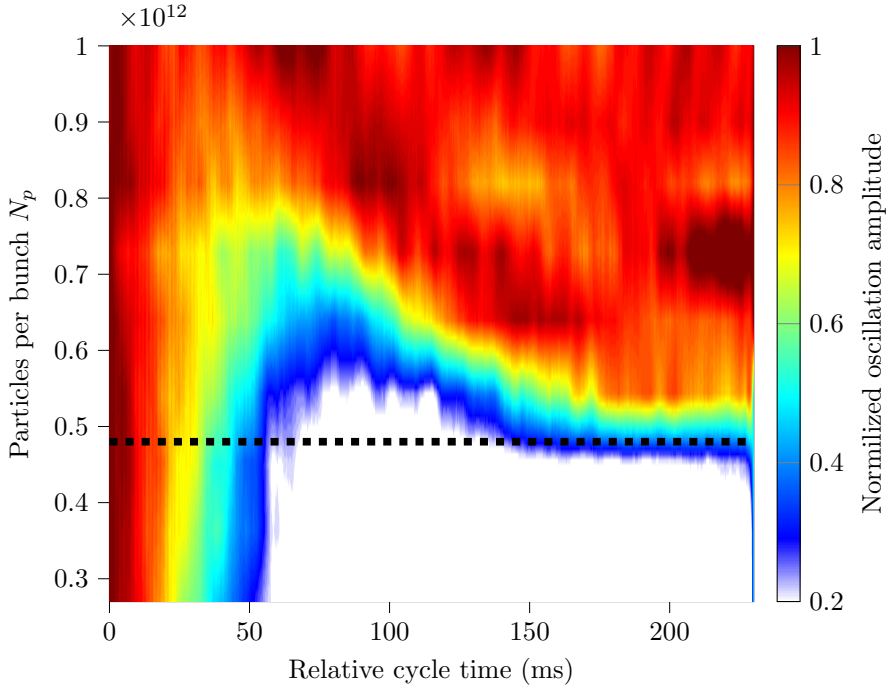

Figure 8.5. Time evolution of the normalized bunch phase oscillation amplitude (color coding) for different intensities after a dipole excitation in BSM with $r_h = 2$ and $r_v = 0.05$.

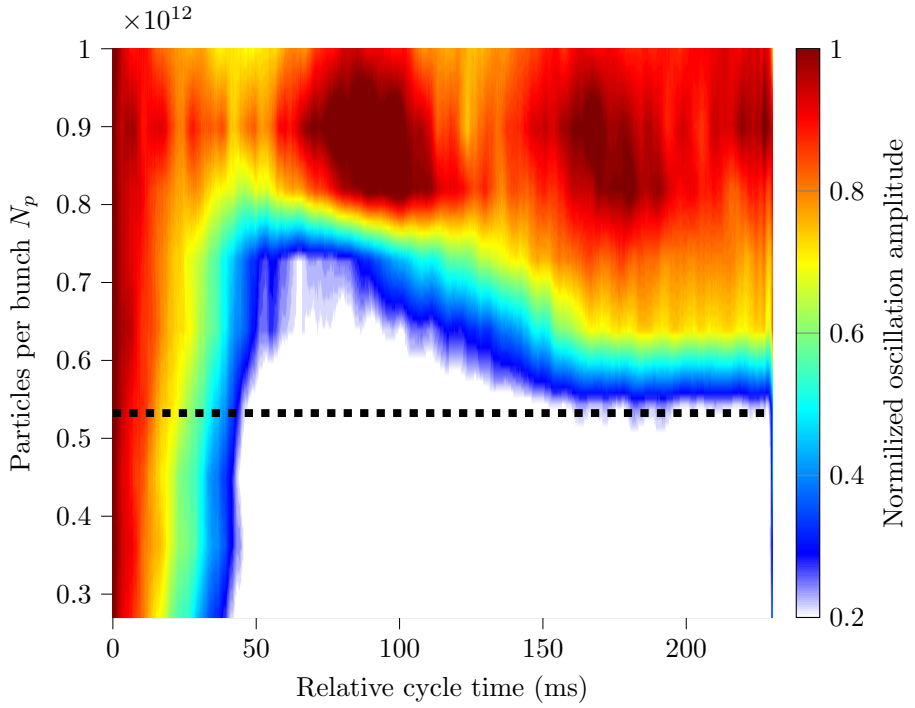

Figure 8.6. Time evolution of the normalized bunch phase oscillation amplitude (color coding) for different intensities after a dipole excitation in BSM with $r_h = 2$ and $r_v = 0.1$.

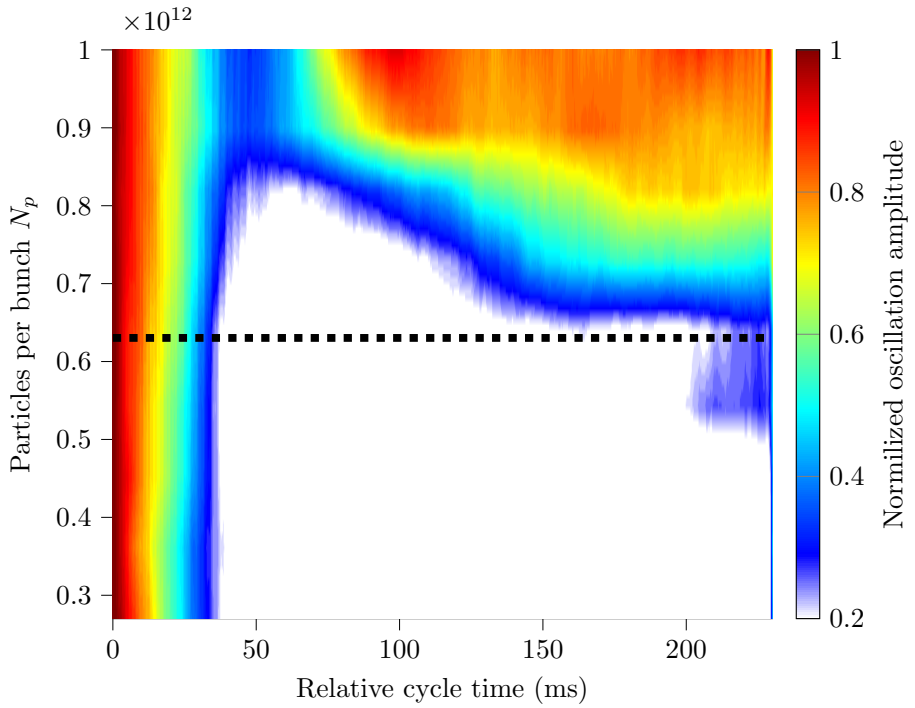

Figure 8.7. Time evolution of the normalized bunch phase oscillation amplitude (color coding) for different intensities after a dipole excitation in BSM with $r_h = 2$ and $r_v = 0.2$.

Table 8.2. The LLD threshold in BSM computed using Eq. (8.1) for different voltage ratios. The threshold of $N_{\mathrm{th}}^{\mathrm{SRF}} \approx 0.36 \times 10^{12}$ was assumed in single RF.

Voltage ratio r_V	**Threshold** $N_{\mathrm{th}} \times 10^{12}$
0.05	0.48 ± 0.06
0.1	0.53 ± 0.05
0.2	0.63 ± 0.08

the synchrotron frequency spread with intensity effects is lower than for the single harmonic RF (black) case reducing LLD threshold. This phenomenon was observed experimentally as the bunch position oscillation was persistently undamped also for the lowest possible bunch intensity of $N_p = 0.27 \times 10^{12}$ (Fig. 8.9 right). Nonetheless, for $r_h = 2$ and $r_V = 0.05$, the synchrotron frequency distribution (Fig. 8.8, blue, dash-dotted) is similar to the single harmonic RF case without any significant enhancement in synchrotron frequency spread. This observation is consistent with the result presented in Fig. 8.10 in which the application of a double-harmonic RF system is not beneficial for the LLD threshold with respect to Fig. 8.4.

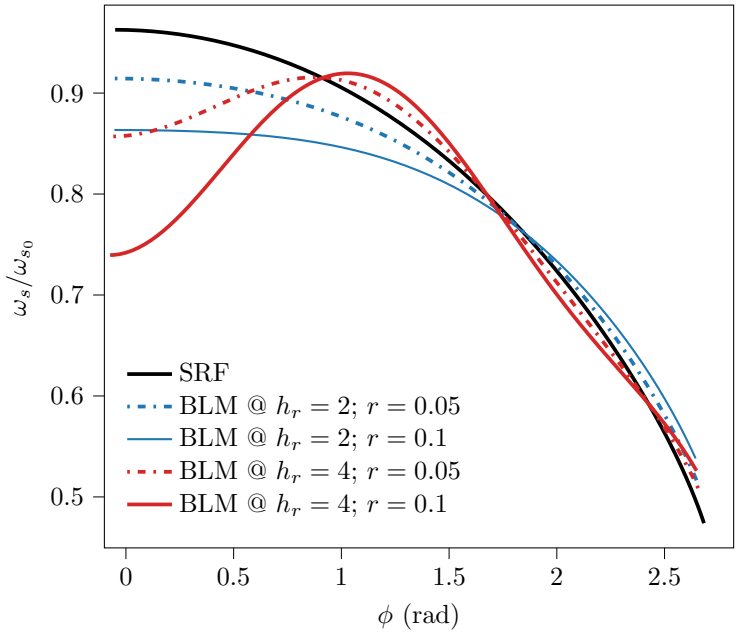

Figure 8.8. Synchrotron frequency distribution normalized to the small-amplitude synchrotron frequency, f_{s0} as a function of the maximum phase deviation of the particle. The blue lines denote the BLM for $r_h = 2$ and the red lines for $r_h = 4$, when the intensity is $N_p = 0.25 \times 10^{12}$.

8.2 Results with 10 MHz and 40 MHz cavity systems

Thanks to the extraordinary flexibility of the PS RF systems, the same experimental study has been repeated, substituting the 20 MHz with the 40 MHz cavities ($r_h = 4$).

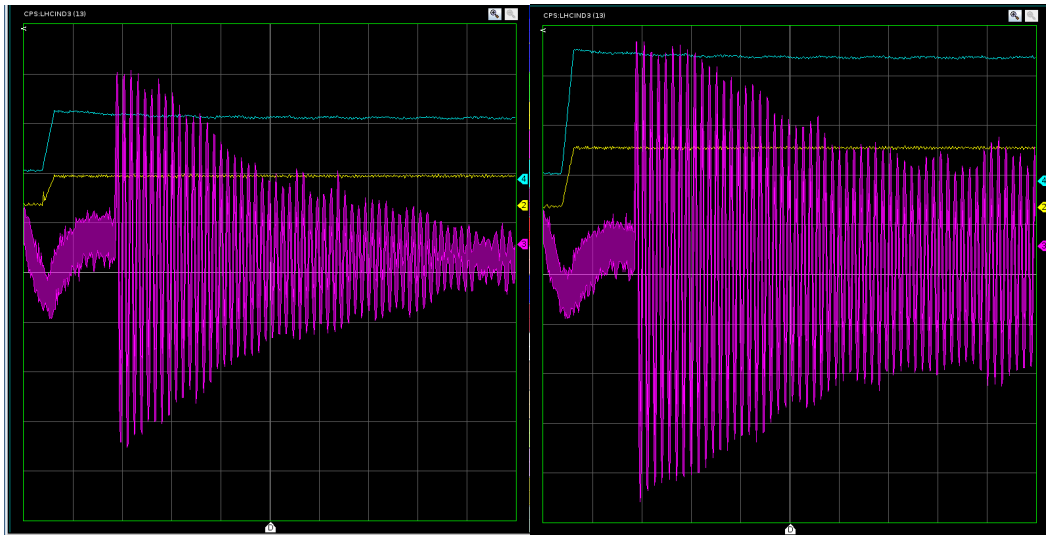

Figure 8.9. Measured phase difference between bunch and RF phase (purple) in BLM ($r_h = 2$) with voltage ratio $r_v = 0.05$ (left), and $r_v = 0.1$ (right) for intensity $N_p = 0.27 \times 10^{12}$. The scales are 100 mV/div on the vertical axis and 20 ms/div on the horizontal axis. The RF voltage amplitude of the two 20 MHz cavities is illustrated with 500 mV/div (blue) and 1 V/div respectively.

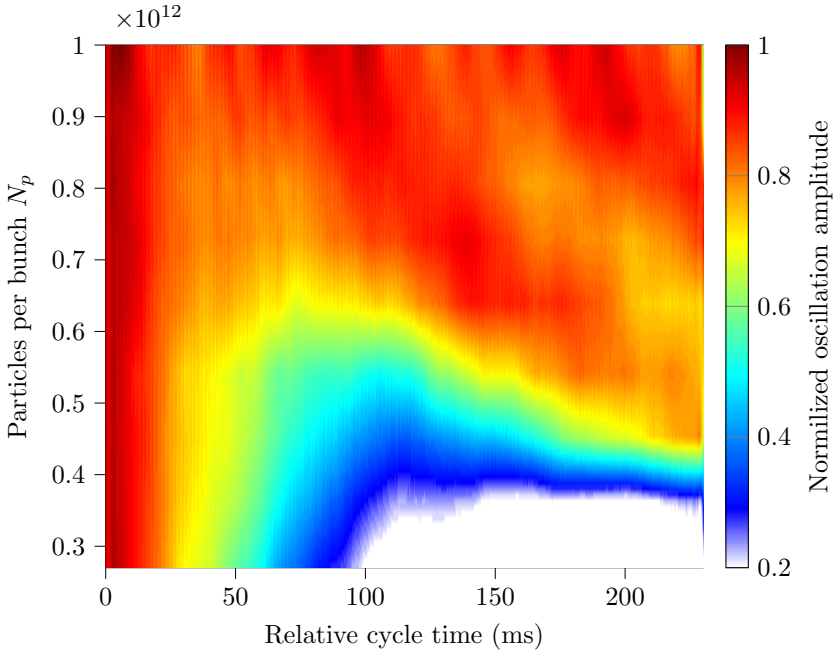

Figure 8.10. Time evolution of the normalized bunch offset amplitude (colour coding) in BLM for $r_h = 2$, $r_v = 0.05$ and $\tau_{\text{full}} = 35$ ns.

There are two cavities in total working as Landau cavities. Each consists of one RF gap providing a maximum voltage of 300 kV.

For a direct comparison, the same bunch length as with $r_h = 2$ has been maintained, covering even different voltage ratios. No LLD has been observed in

the comparable range of intensities. This behavior is expected since already for a voltage ratio of $r_V = 0.05$, using Eq. (8.1), the LLD threshold increase by a factor of almost four is predicted. The threshold would, therefore, be well beyond the accessible intensity range for the given bunch length in the PS.

In the BLM configuration, we are again limited by the region with zero derivatives of the synchrotron frequency distribution $df_s/d\phi$. As shown in Fig. 8.8 for $r_h = 4$ (red), this inflection point ($df_s/d\phi = 0$) of the synchrotron frequency distribution is well below the current bunch length ($\tau_{\text{full}} = 25$ ns), leading to the vanishing LLD threshold.

A complementary measurement is the phase difference of the RF voltage and the spectral component of the beam at the RF frequency. Figure 8.11 illustrates that for intensity $N_p = 0.17 \times 10^{10}$ (the lowest reachable with the current settings), the measured phase-loop error shows damping for both single RF and BSM, except for BLM.

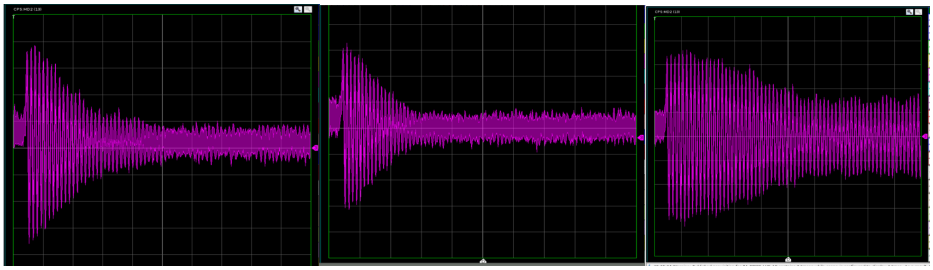

Figure 8.11. Measured phase difference between the bunch and the RF phase in single RF (left), BSM (center) and BLM (right) respectively for intensity $N_p = 1.7 \times 10^{11}$. For the DRF cases, voltage ratio $r = 0.1$ and harmonic ratio $r_h = 4$ have been considered. The scales are 100 mV/div on the vertical axis and 20 ms/div on the horizontal axis.

8.3 Conclusion

We applied again the straightforward beam-based measurement technique to study LLD experimentally but in very different conditions with respect to the SPS. In the PS, the remarkable reproducibility of the bunch length for both single RF and BSM across the analyzed voltage ratios allowed us to benchmark the analytical equation of the LLD threshold, proposed in Chapter 3. In particular, we evaluated the relative change in the threshold, which was computed based on the values of the voltage ratio and taking into account the variation of the bunch length. Finally, we also estimated the corresponding statistical errors for the analytical estimations. The findings show a very good agreement with the analytical predictions. Moreover, improved longitudinal stability for different double-harmonic RF configurations has been proven in BSM ($r_h = 2$).

For the higher harmonic RF system at the fourth harmonic of the principal one ($r_h = 4$), the intensity reach did not allow observing any LLD. On the contrary, in the BLM case, the oscillations of the bunch offset were, as expected, undamped, as the bunch length exceeded the critical phase of the synchrotron frequency inflection point.

Chapter 9

Summary and conclusions

The loss of Landau damping (LLD) in synchrotrons is a critical condition that can lead to beam quality degradation and particle loss. It occurs when a coherent mode emerges from the incoherent band of the particle oscillation frequencies. In the longitudinal plane, the LLD threshold can be raised, in principle, by reducing the longitudinal impedance of the individual components in the accelerator. However, increasing the synchrotron frequency spread by means of a double-harmonic RF system is often much more efficient. The present work expands the recent longitudinal LLD threshold studies in a single-harmonic RF case to the double-harmonic RF configuration.

Refined analytical estimates for the synchrotron frequency distribution allowed to derive an analytical expression for the LLD threshold from the Lebedev equation in the bunch shortening mode, where both RF systems are in phase at the bunch position for a non-accelerating bucket. An inductive impedance above transition energy (or capacitive impedance below transition energy) and particle distributions belonging to the binomial family have been considered. This scenario is relevant for most high (low) energy synchrotrons. In agreement with the single-harmonic RF case, the threshold is inversely proportional to the impedance cutoff frequency, f_c when $f_c \gg 1/\tau_{\text{full}}$, with τ_{full} as full bunch length. In line with past studies, the higher harmonic RF system significantly increases the LLD threshold. We demonstrated that it scales with the factor $(1 + r_V r_h^3)/\sqrt{1 + r_V r_h}$, where r_V and r_h are the voltage ratio and the harmonic number ratio respectively. The analytical equation for the LLD threshold has been benchmarked with a semianalytical approach using the code MELODY, showing a very good agreement for short bunch lengths. Further validation has been performed by comparing MELODY with the macroparticle tracking simulation code BLonD. Both codes, based on different approaches to study the longitudinal beam dynamics, agree extremely well. Non-monotonic LLD threshold dependency versus the bunch length observed in the past analysis was explained by the difference in the threshold definition based on kick response. We showed that an extremely slow decoherence after a kick can be observed in bunch shortening mode for intensities below the real LLD threshold, which remains a monotonic function of the bunch length.

The second relevant configuration examined for an inductive impedance above transition energy is the bunch lengthening mode operating with both RF systems

in counter-phase at the bunch position. Although it promises a higher synchrotron frequency spread, at first sight, it has strong limitations. In particular, if the maximum of the synchrotron frequency distribution does not correspond to the maximum particle oscillation amplitude, the LLD is lost at zero intensity. This is in agreement with previous studies and measurements. Since the bunch lengthening mode is highly sensitive to the relative phase Φ_2 between the two RF systems, an extensive parameter scan was performed to evaluate the LLD threshold in hybrid configurations. For example, for a cutoff frequency of an order of magnitude above the RF frequency, $f_c = 10 f_{\mathrm{rf}}$, a gain of a factor three with respect to the bunch shortening mode was observed for $\Phi_2 \approx 2 \pm \pi$. Nonetheless, the margin of error in the relative phase is very tight, which would make it most challenging to operate in this regime.

Below transition energy, $\eta \mathrm{Im}Z/k < 0$, the LLD occurs when the frequency of the coherent mode is at the lower limit of the incoherent synchrotron frequency band, $\Omega = \min[f_s(\phi)]$. Typically, the LLD threshold is higher than the above transition energy case. The additional focusing force due to beam-induced voltage distorts the potential well, ultimately collapsing the bucket. The limiting conditions for a binomial particle distribution were calculated, agreeing very well with the iterative bunch generation algorithm implemented in MELODY. In this energy regime, the bunch shortening mode has the minimum of the synchrotron frequency distribution at the tail of the bunch. However, when the synchrotron frequency distribution is non-monotonic (e.g., $r_h = 4$) its derivative becomes positive $df_s/d\phi > 0$, and a minimum occurs where $df_s/d\phi = 0$. In these conditions, a van Kampen mode with frequency at $\Omega = \min[f_s(\phi)]$ is present already at zero intensity, leading to a vanishing LLD threshold. In addition, for a binomial distribution with a tail form factor of $\mu > 1$, the threshold is independent of the impedance cutoff frequency. This is consistent with the single-harmonic RF case. On the contrary, the LLD threshold, in the bunch lengthening mode below transition energy, results in being monotonic as a function of the emittance. In particular, a jump in the derivative of the LLD threshold versus the phase, $dN_{\mathrm{th}}/d\phi$, was observed, which is linked to the change of the minimum synchrotron frequency, $\min[f_s(\phi)]$ from the center to the tail of the bunch. Beyond that, the LLD threshold converges to the single-harmonic RF case, no longer providing the benefits of using the bunch lengthening mode.

The work applied a straightforward beam-based measurement technique to study the LLD threshold experimentally. A single bunch is excited by a longitudinal phase kick to observe the decoherence and possibly undamped bunch offset oscillation in a rigid bucket due to the LLD. An extensive measurement campaign was performed in two different injector synchrotrons. In the SPS, we first focused on the single-harmonic RF system, taking into account only the voltage contribution coming from the 200 MHz RF system as a reference study. Subsequently, we moved to the relevant case of a double-harmonic RF system, analyzing the voltage contribution of the 800 MHz RF system in bunch shortening mode. The significant threshold increase for double-harmonic RF configurations has been demonstrated. Results were then benchmarked with MELODY and macroparticle tracking simulations with BLonD. Even though both numerical methods exhibit excellent agreement, the measured LLD threshold is about 30% lower than expected. This suggests further refinement in the broad-band part of the current SPS beam coupling impedance model and

evaluation of possible noise excitation from the RF system.

We also performed measurements in the PS, equipped with RF systems at 10 MHz, 20 MHz, and 40 MHz. Thus, frequency ratios of two and four were studied under very different conditions in terms of bucket filling factor compared to the SPS. The measurements were mainly devoted to benchmarking the scaling factor of the derived analytical equation for the LLD threshold. The findings have shown a very good agreement with the analytical predictions, and a longitudinal stability gain for different double-harmonic RF configurations has been proven in bunch shortening mode for a harmonic number ratio of $r_h = 2$. For a fourth harmonic RF system, the expected LLD threshold is so high that the intensity reach did not allow observation of LLD. As expected from theory, in bunch lengthening mode ($r_h = 4$), the bunches were long enough to be not damped at all.

Further studies could focus on deriving analytical equations for other configurations considering different impedance types, beam energy regimes, as well as the relative phase between the two RF systems. Additionally, the corresponding expressions of effective impedance could be introduced to evaluate the LLD threshold for arbitrary impedance models. Eventually, this work could be a basis for multi-bunch stability evaluation in double-harmonic RF systems.

Appendix A

Frenet Serret coordinate system

Let us consider a reference system (X, Y, Z) and let's write it in terms of a new reference system (x, s, y) fixed with the reference particle as is shown in the Figure A.1:

$$\begin{cases} X = (\rho + x)\cos\theta = (\rho + x)\cos\left(\frac{s}{\rho}\right) \\ Y = (\rho + x)\sin\left(\frac{s}{\rho}\right) \\ Z = y \end{cases} \tag{A.1}$$

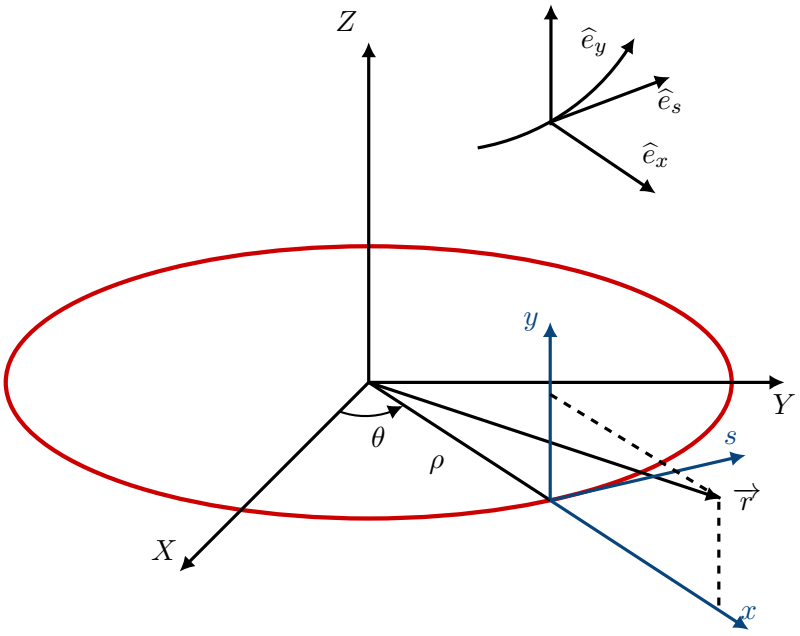

Figure A.1. Frenet Serret coordinate system.

We defined the position vector $\vec{r} = \rho\hat{e}_x + x\hat{e}_x + y\hat{e}_y$ in terms of the new coordinates. We assume that ρ is the accelerator curvature radius, which in general can vary along s, but we assume that inside the magnets it is constant. In other words, we have

$$\frac{d\rho}{ds} = 0.$$

If we consider now the infinitesimal displacement of the position vector $d\vec{r}$, referring to Figure A.2, we have:

$$d\vec{r} = \rho d\hat{e}_x + dx\hat{e}_x + xd\hat{e}_x + dy\hat{e}_y,$$

moreover, we have:

$$d\hat{e}_x = d\theta\hat{e}_s = \frac{ds}{\rho}\hat{e}_s.$$

Substituting the previous one in $d\vec{r}$, we obtain:

$$d\vec{r} = dx\hat{e}_x + (1 + \frac{x}{\rho})ds\hat{e}_s + dy\hat{e}_y$$

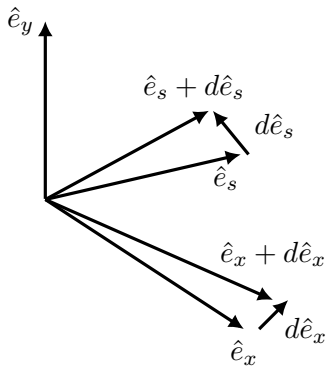

Figure A.2. Infinitesimal displacement in the new coordinates.

We can now compute the speed:

$$\vec{v} = \frac{d\vec{r}}{dt} = \dot{x}\hat{e}_x + (1 + \frac{x}{\rho})\dot{s}\hat{e}_s + \dot{y}\hat{e}_y.$$

In conclusion, the use of the metric coefficients $h_1 = 1$, $h_2 = 1 + \frac{x}{\rho}$, $h_3 = 1$ allows us to use all the operators in this new coordinates as $\vec{\nabla} f$, $\vec{\nabla} \cdot \vec{A}$ and $\vec{\nabla} \times \vec{A}$.

$$\vec{\nabla} f = \frac{1}{h_1}\frac{\partial f}{\partial x}\hat{e}_x + \frac{1}{h_2}\frac{\partial f}{\partial s}\hat{e}_s + \frac{1}{h_3}\frac{\partial f}{\partial y}\hat{e}_y = \frac{\partial f}{\partial x}\hat{e}_x + \frac{1}{1+\frac{x}{\rho}}\frac{\partial f}{\partial s}\hat{e}_s + \frac{\partial f}{\partial y}\hat{e}_y \tag{A.2}$$

$$\begin{aligned}\vec{\nabla} \cdot \vec{A} &= \tfrac{1}{h_1 h_2 h_3}\left[\tfrac{\partial(h_2 h_3 A_x)}{\partial x} + \tfrac{\partial(h_1 h_3 A_s)}{\partial s} + \tfrac{\partial(h_1 h_2 A_y)}{\partial y}\right] = \\ &= \tfrac{1}{1+\frac{x}{\rho}}\left[\tfrac{\partial\left[\left(1+\frac{x}{\rho}\right)A_x\right]}{\partial x} + \tfrac{\partial A_s}{\partial s} + \left(1+\tfrac{x}{\rho}\right)\tfrac{\partial A_y}{\partial y}\right]\end{aligned} \tag{A.3}$$

$$\begin{aligned}\vec{\nabla} \times \vec{A} = \frac{1}{h_2 h_3}\left[\frac{\partial(h_3 A_y)}{\partial s} - \frac{\partial(h_2 A_s)}{\partial y}\right]\hat{e}_x + \frac{1}{h_1 h_3}\left[\frac{\partial(h_1 A_x)}{\partial y} - \frac{\partial(h_3 A_y)}{\partial x}\right]\hat{e}_s + \\ + \frac{1}{h_1 h_2}\left[\frac{\partial(h_2 A_s)}{\partial x} - \frac{\partial(h_1 A_x)}{\partial s}\right]\hat{e}_y = \\ = \frac{1}{1+\frac{x}{\rho}}\left[\frac{\partial A_y}{\partial s} - \left(1+\frac{x}{\rho}\right)\frac{\partial A_s}{\partial y}\right]\hat{e}_x + \left[\frac{\partial A_x}{\partial y} - \frac{\partial A_y}{\partial x}\right]\hat{e}_s + \frac{1}{1+\frac{x}{\rho}}\left[\frac{\partial\left[\left(1+\frac{x}{\rho}\right)A_s\right]}{\partial x} - \frac{\partial A_x}{\partial s}\right]\hat{e}_y\end{aligned} \tag{A.4}$$

Appendix B

Time-dependent harmonic of the induced voltage

For convenience, we report again the definition of the coupling impedance and its wake function (see Chapter 2):

$$Z(\omega) = \int_{-\infty}^{\infty} \mathcal{W}(\phi) e^{-i\omega\phi/\omega_{\mathrm{rf}}} \frac{d\phi}{\omega_{\mathrm{rf}}}\,, \tag{B.1}$$

$$\mathcal{W}(\phi) = \frac{1}{2\pi} \int_{-\infty}^{\infty} Z(\omega) e^{i\omega\phi/\omega_{\mathrm{rf}}} d\omega\,. \tag{B.2}$$

Let us consider a perturbation of the line density as

$$\tilde{\lambda}(\phi, \Omega, t) = \tilde{\lambda}(\phi, \Omega) e^{i\Omega t}\,, \tag{B.3}$$

where $t = \Theta/\omega_0$ corresponds to the azimuth coordinate of the accelerator. In order to evaluate the induced voltage and the phase, ϕ, at $t(k = 0)$, we consider the line density k-turns before, namely $\tilde{\lambda}(\phi, \Omega) e^{i\Omega(t - kT_0)}$. The wake function delays accordingly to the same amount $W(\phi - \varphi + 2\pi hk)$. We sum the contributions along $k > 0$ to take into account the field contributions from the past turns. We express the induced voltage as the convolution of the line density with the wake function [51], i.e.,

$$\tilde{V}_{\mathrm{ind}}\,(\phi, t) = -qN_p \sum_{k=0}^{\infty} \int_{-\pi h}^{\pi h} \tilde{\lambda}(\varphi, \Omega) e^{i\Omega(t - kT_0)} \mathcal{W}(\phi - \varphi + 2\pi hk) d\varphi\,, \tag{B.4}$$

where the offset sum of $2\pi hk$ keeps track of the wakefield evolution over time.

For the causality principle, we can extend the sum for $k < 0$. Inserting Eq. (B.2) in Eq. (B.4).

$$\tilde{V}_{\mathrm{ind}}\,(\phi, t) = -qN_p e^{i\Omega t} \int_{-\infty}^{\infty} \tilde{\lambda}(\varphi, \Omega) d\varphi \int_{-\infty}^{\infty} Z(\omega) e^{i\omega(\phi - \varphi)/\omega_{\mathrm{rf}}} \sum_{k=-\infty}^{\infty} e^{i2\pi k(\omega - \Omega)/\omega_0} \frac{d\omega}{2\pi}\,. \tag{B.5}$$

The last term of Eq. (B.5) represents the Fourier expansion of periodic pulses

$$\sum_{k=-\infty}^{\infty} e^{i2\pi k(\omega - \Omega)/\omega_0} = \omega_0 \sum_{k=-\infty}^{\infty} \delta\left[\omega - (k\omega_0 + \Omega)\right]\,. \tag{B.6}$$

Therefore, substituting Eq. (B.6) in Eq. (B.5), the induced voltage can be expressed as:

$$\begin{aligned} \tilde{V}_{\mathrm{ind}}\left(\phi,t\right) &= -qN_p h\omega_0 e^{i\Omega t}\sum_{k=-\infty}^{\infty} Z_k(\Omega)\tilde{\lambda}_k(\Omega)e^{ik\phi/h}e^{i\Omega\phi/\omega_{\mathrm{rf}}} \Rightarrow \\ \Rightarrow \tilde{V}_{\mathrm{ind}}\left(\phi,t\right) &= e^{i\Omega t}\sum_{k=-\infty}^{\infty} \tilde{V}_k(\Omega)e^{ik\phi/h}e^{i\Omega\phi/\omega_{\mathrm{rf}}}\,, \end{aligned} \tag{B.7}$$

where $Z_k = Z(k\omega_0 + \Omega)$ and the harmonic of the line density is equal to

$$\tilde{\lambda}_k(\Omega) = \frac{1}{2\pi h}\int_{-\pi h}^{\pi h} \tilde{\lambda}(\phi,\Omega)e^{-ik\phi/h}e^{-i\Omega\phi/\omega_{\mathrm{rf}}}d\phi\,. \tag{B.8}$$

Appendix C

Mechanism of Landau damping

There are a large number of collective instabilities acting on high-intensity accelerators [51]. Landau damping [32] is a natural stabilization mechanism that prevents collective instabilities from arising when particles have sufficient synchrotron frequency spread.

Section 2.1.4 has shown that a particle can be approximated to a harmonic oscillator. If we consider an external perturbation with frequency Ω, the equation of motion governing the dynamics is:

$$\ddot{x} + \omega^2 x = \mathcal{A}\cos(\Omega t)\,, \tag{C.1}$$

and, imposing the initial condition $\dot{x}(0) = 0$ and $x(0) = 0$, its solution can be written as:

$$x(t) = -\frac{\mathcal{A}}{\Omega^2 - \omega^2}\left[\cos(\Omega t) - \cos(\omega t)\right]\,. \tag{C.2}$$

In order to deal with many particles, let us consider a set of N oscillators having different resonant frequencies with distribution $\rho(\omega)$ and a spread $\delta\omega$. A physical representation of this system can be a set of pendulums with different rope lengths, as illustrated in Fig. C.1.
The displacement of the center of mass is then:

$$\langle x(t)\rangle = -\mathcal{A}\int_{-\infty}^{\infty}\rho(\omega)\frac{\cos(\Omega t) - \cos(\omega t)}{\Omega^2 - \omega^2}d\omega\,. \tag{C.3}$$

Following [49, 51, 109–111], let us consider for simplicity a narrow beam spectrum around a frequency ω_x and driving frequency close to the oscillator frequency spectrum, i.e., $\Omega \approx \omega_x$ such that $\Omega + \omega \approx 2\omega_x$. Therefore, Eq. (C.3) becomes:

$$\langle x(t)\rangle = -\frac{\mathcal{A}}{2\omega_x}\int_{-\infty}^{\infty}\rho(\omega)\frac{\cos(\Omega t) - \cos(\omega t)}{\Omega - \omega}d\omega\,. \tag{C.4}$$

Moreover, for convenience, to avoid singularities in $\Omega - \omega = 0$, we introduce the variable $u = \omega - \Omega$. This leads to:

$$\begin{aligned}\langle x(t)\rangle &= \frac{A}{2\omega_x}\int_{-\infty}^{\infty}\frac{\rho(u+\Omega)}{u}[\cos(\Omega t) - \cos(\Omega t + ut)]du = \\ &= \frac{A}{2\omega_x}\left[\cos(\Omega t)\int_{-\infty}^{\infty}\rho(u+\Omega)\frac{1-\cos(ut)}{u}du + \right. \\ &\qquad \left. + \sin(\Omega t)\int_{-\infty}^{\infty}\rho(u+\Omega)\frac{\sin(ut)}{u}du\right]\,.\end{aligned} \tag{C.5}$$

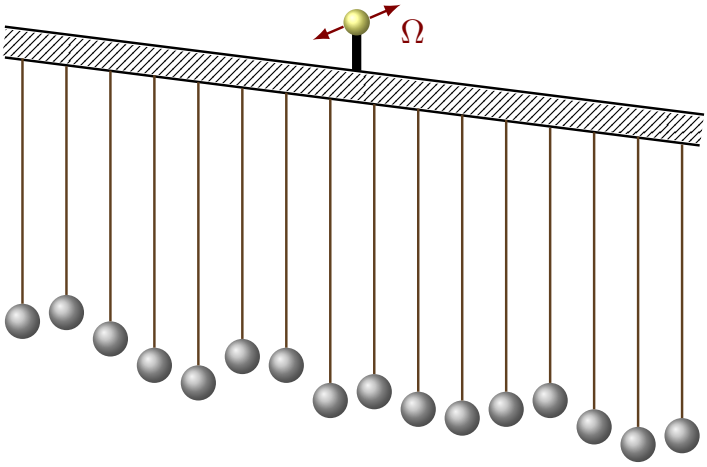

Figure C.1. Pendulum system representing a set of harmonic oscillators with slightly different angular velocity (different length of the ropes) perturbed by an external force with frequency Ω.

Since we are interested in long-term behavior, we can compute the limit to infinity. Thus, taking each term separately yields:

$$\begin{aligned} \lim_{t\to\infty} \frac{\sin ut}{u} &= \pi\delta(u), \\ \lim_{t\to\infty} \frac{1-\cos ut}{u} &= \mathrm{P.V.}\left(\frac{1}{u}\right), \end{aligned} \tag{C.6}$$

where $\delta(u)$ is the Dirac delta function. Eventually, by substituting into Eq. (C.6), we reach the final form of the center of mass displacement in the permanent regime, i.e.:

$$\langle x(t)\rangle = \frac{A}{2\omega_x}\left[\cos(\Omega t)\,\mathrm{P.V.}\int_{-\infty}^{\infty}\frac{\rho(\omega)}{\omega-\Omega}d\omega + \pi\rho(\Omega)\sin(\Omega t)\right]. \tag{C.7}$$

The system's center of mass oscillation amplitude does not increase with time but remains limited for $t \to \infty$. This is Landau damping which, in accelerator physics, is not a dissipative damping process but rather an absence of instability.

It is worth pointing out that if we consider different initial conditions (i.e., $\dot{x}(0) \neq 0$; $x(0) \neq 0$) Eq. (C.6) has additional terms, namely:

$$\dot{x}(0)\int \rho(\omega)\frac{\sin(\omega t)}{\omega}d\omega + x(0)\int \rho(\omega)\cos(\omega t)d\omega\,. \tag{C.8}$$

If we watch at the dynamic of the particles with these new initial conditions, we can see in Fig. C.2 that although the individual particle continues their oscillations, the center of mass is damped to zero. Nonetheless, this must be distinguished from Landau damping and represent rather a decoherence phenomenon (also known as phase-mixing or filamentation). Contrary to Landau damping, it's a dissipative process that leads to emittance growth.

The energy of an harmonic oscillator is proportional to the square of the oscillation amplitude. Hence, the total oscillation energy of the system is:

$$\mathcal{E} = \frac{NA^2}{\omega_x^2}\int \rho(u+\Omega)\frac{\sin^2(ut/2)}{u^2}du\,. \tag{C.9}$$

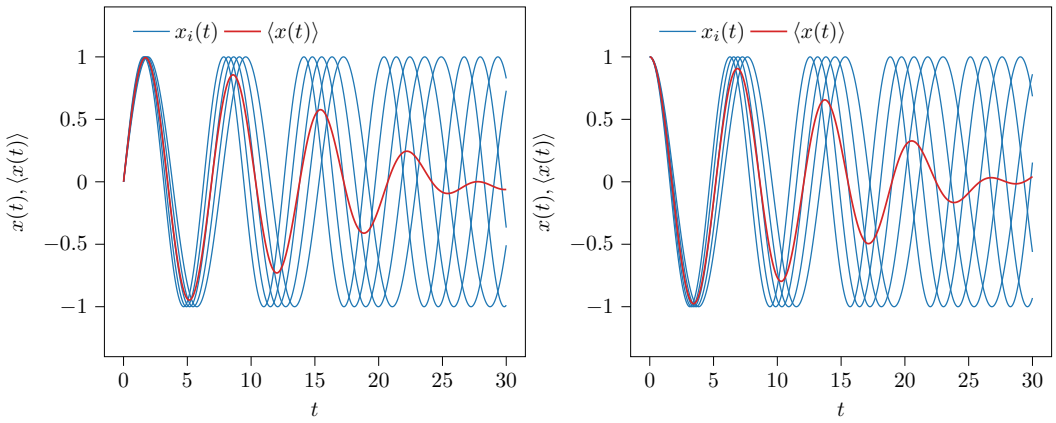

(a) $\dot{x}(0) \neq 0$; $x(0) = 0$. **(b)** $\dot{x}(0) = 0$; $x(0) \neq 0$.

Figure C.2. Motion of particles with frequency spread (in blue), and center of mass response in red. Two different initial conditions have been imposed.

As t increases, the region where $\sin^2(ut/2)/u^2$ assumes significant values narrows around $u = 0$ and tends to a Dirac, as:

$$\lim_{t\to\infty} \frac{\sin^2(ut/2)}{u^2} = \frac{\pi t}{2}\delta(u)\,, \tag{C.10}$$

and substituting gives:

$$\mathcal{E} = \frac{\pi N A^2}{2\omega_x^2}\rho(\Omega)t\,. \tag{C.11}$$

Equation (C.11) increases linearly with t, suggesting that the system absorbs energy from the driving force indefinitely while the center of mass response remains within the bounds. As we said, this energy is not dissipative and regards only a narrow portion of the particles oscillating close to the driving frequency. In particular, particles with $|\omega = \Omega| < 1/t$ are in resonance with the driving force. However, since their number decreases with time as $1/t$, while their amplitude increases as t, the net contribution to the center of mass displacement remains constant.

The asymptotic behavior in Eq. (C.7) holds for $t \gg \delta\omega$. Note that the resistive term is proportional to the particle distribution $\rho(\Omega)$. Landau damping is lost when the driving frequency is outside the spectrum and a beating phenomenon takes over. In addition, due to the granularity of the beam consisting of a finite number of particles, Landau damping also ceases when t is larger than $1/\Delta\omega_{i,j}$, where $\Delta\omega_{i,j}$ is the frequency spacing between two nearest particles. Thus, the condition for Landau damping is:

$$\frac{1}{\Delta\omega_{i,j}} \gg t \gg \frac{1}{\delta\omega}\,. \tag{C.12}$$

Bibliography

[1] M. K. Gaillard, P. D. Grannis, and F. J. Sciulli, "The standard model of particle physics," *Reviews of Modern Physics*, vol. 71, no. 2, p. S96, 1999.

[2] M. Oliphant, "The acceleration of particles to very high energies," *Classified memo submitted to DSIR, University of Birmingham Archive*, 1943.

[3] E. M. McMillan, "The synchrotron — a proposed high energy particle accelerator," *Physical Review*, vol. 68, no. 5-6, p. 143, 1945.

[4] E. Courant and H. Snyder, "Theory of the alternating-gradient synchrotron," *Annals of Physics*, vol. 3, no. 1, pp. 1–48, 1958.

[5] Conseil européen pour la recherche nucléaire (CERN), `https://home.cern/`.

[6] C. Bracco *et al.*, "Beam studies and experimental facility for the AWAKE experiment at CERN," *Nuclear Instruments and Methods in Physics Research Section A: Accelerators, Spectrometers, Detectors and Associated Equipment*, vol. 740, pp. 48–53, 2014.

[7] I. Efthymiopoulos *et al.*, "HiRadMat: A New Irradiation Facility for Material Testing at CERN," Tech. Rep. CERN-ATS-2011-232, 2011.

[8] D. Banerjee *et al.*, "The north experimental area at the CERN super proton synchrotron," Tech. Rep. CERN-ACC-NOTE-2021-0015, 2021.

[9] G. Aad *et al.*, "Observation of a new particle in the search for the standard model Higgs boson with the ATLAS detector at the LHC," *Physics Letters B*, vol. 716, no. 1, pp. 1–29, 2012.

[10] S. Chatrchyan *et al.*, "Observation of a new boson at a mass of 125 GeV with the CMS experiment at the LHC," *Physics Letters B*, vol. 716, no. 1, pp. 30–61, 2012.

[11] J. Coupard *et al.*, "LHC Injectors Upgrade, Technical Design Report," Tech. Rep. CERN-ACC-2016-0041, CERN, Geneva, Apr 2016.

[12] O. Aberle *et al.*, *High-Luminosity Large Hadron Collider (HL-LHC): Technical design report*. No. CERN-2020-010 in CERN Yellow Reports: Monographs, Geneva: CERN, 2020.

[13] A. Lasheen, T. Bohl, S. Hancock, E. Radvilas, T. Roggen, and E. Shaposhnikova, "Single Bunch Longitudinal Instability in the CERN SPS," in *Proc. of International Particle Accelerator Conference (IPAC'16), Busan, Korea, May 8-13, 2016*, no. 7 in International Particle Accelerator Conference, (Geneva, Switzerland), pp. 1670–1673, JACoW, June 2016.

[14] A. S. Lasheen, *Beam measurements of the longitudinal impedance of the CERN Super Proton Synchrotron.* PhD thesis, Université Paris Saclay (COmUE), 2017.

[15] J. Repond, *Possible Mitigations of Longitudinal Intensity Limitations for HL-LHC Beam in the CERN SPS.* PhD thesis, 2019.

[16] I. Karpov and M. Gadioux, "Mechanism of Longitudinal Single-Bunch Instability in the CERN SPS," in *Proc. IPAC'21*, no. 12 in International Particle Accelerator Conference, pp. 3161–3164, JACoW Publishing, Geneva, Switzerland, 08 2021.

[17] P. Belochitskii *et al.*, "Commissioning and first operation of the antiproton decelerator (AD)," in *Proceedings of the 2001 particle accelerator conference (Cat. No. 01CH37268)*, vol. 1, pp. 580–584, IEEE, 2001.

[18] L. Durieu, O. Ferrando, J.-Y. Hemery, J.-P. Riunaud, and B. Williams, "The CERN PS east area in the LHC era," in *Proceedings of the 1997 Particle Accelerator Conference (Cat. No.97CH36167)*, vol. 1, pp. 228–230 vol.1, 1997.

[19] H. Damerau *et al.*, "Improved longitudinal performance of the LHC beam in the CERN PS," in *Proc. 13th International Particle Accelerator Conference (IPAC'22)*, no. 13, pp. 2165–2168, JACoW Publishing, Geneva, Switzerland, 07 2022.

[20] E. Shaposhnikova, "Cures for Beam Instabilities in the CERN SPS and their Limitations," Tech. Rep. CERN-AB-2007-075, CERN, Geneva, 2006.

[21] H. Timko, T. Argyropoulos, I. Karpov, and E. Shaposhnikova, "Beam instabilities after injection to the LHC," in *Proc. 61st ICFA Advanced Beam Dynamics Workshop (HB'18), Daejeon, Korea, 17-22 June 2018*, no. 61, pp. 163–167, JACoW Publishing, July 2018.

[22] E. Shaposhnikova *et al.*, "Loss of Landau damping in the LHC," in *Proceedings, 2nd International Particle Accelerator Conference (IPAC 2011): San Sebastian, Spain*, p. MOPC057, 2011.

[23] M. Blaskiewicz *et al.*, "Longitudinal solitons in RHIC," in *Proceedings of the 2003 Particle Accelerator Conference*, vol. 5, pp. 3029–3031, IEEE, 2003.

[24] R. Moore *et al.*, "Longitudinal bunch dynamics in the Tevatron," in *Proceedings of the 2003 Particle Accelerator Conference*, vol. 3, pp. 1751–1753, IEEE, 2003.

[25] T. Argyropoulos, *Longitudinal beam instabilities in a double RF system.* PhD thesis, 2015. Presented 12 Jan 2015.

[26] A. Burov, "Van Kampen modes for bunch longitudinal motion," in *Proceedings of 46th ICFA Advanced Beam Dynamics Workshop on High-Intensity and High Brightness Hadron Beams*, 2010.

[27] H. Timko *et al.*, "Beam longitudinal dynamics simulation studies," *Phys. Rev. Accel. Beams*, vol. 26, p. 114602, Nov 2023.

[28] CERN BLonD Simulation Suite Code Repository: `https://gitlab.cern.ch/blond/BLonD`.

[29] CERN BLonD Simulation Suite Website: `http://blond.web.cern.ch`.

[30] I. Karpov and E. Shaposhnikova, "Generalized threshold of longitudinal multi-bunch instability in synchrotrons," *arXiv preprint arXiv:2309.06638*, 2023.

[31] M. Mangano *et al.*, "FCC physics opportunities: future circular collider conceptual design report volume 1," *European Physical Journal C*, vol. 79, no. 6, p. 474, 2019.

[32] L. D. Landau, "On the vibrations of the electronic plasma," *Uspekhi Fizicheskikh Nauk*, vol. 93, no. 3, pp. 527–540, 1967.

[33] V. K. Neil and A. M. Sessler, "Longitudinal Resistive Instabilities of Intense Coasting Beams in Particle Accelerators," *Review of Scientific Instruments*, vol. 36, pp. 429–436, 12 1965.

[34] F. Sacherer, "A longitudinal stability criterion for bunched beams," *IEEE Transactions on Nuclear Science*, vol. 20, no. 3, pp. 825–829, 1973.

[35] A. N. Lebedev, "Coherent synchrotron oscillations in the presence of a space charge," *At. Energ.* ***25****, 851*, 1968.

[36] V. Balbekov and S. Ivanov, "The influence of chamber inductance on the threshold of longitudinal bunched beam instability," in *Proceedings of 2nd European Particle Accelerator Conference, Nice, France*, pp. 1566–1568, 1990.

[37] A. Hofmann and F. Pedersen, "Bunches with local elliptic energy distributions," *IEEE Transactions on Nuclear Science*, vol. 26, no. 3, pp. 3526–3528, 1979.

[38] O. Boine-Frankenheim and T. Shukla, "Space charge effects in bunches for different RF wave forms," *Phys. Rev. ST Accel. Beams*, vol. 8, p. 034201, Mar 2005.

[39] O. Boine-Frankenheim and O. Chorniy, "Stability of coherent synchrotron oscillations with space charge," *Phys. Rev. ST Accel. Beams*, vol. 10, p. 104202, Oct 2007.

[40] E. Shaposhnikova, T. Argyropoulos, and I. Karpov, "Landau damping in the longitudinal plane," in *CERN Yellow Reports: Conference Proceedings*, vol. 9, pp. 54–54, 2020.

[41] Y. Chin, K. Yokoya, and K. Satoh, "Instability of a bunched beam with synchrotron frequency spread," *Part. Accel.*, vol. 13, no. KEK-82-18, pp. 45–66, 1982.

[42] N. G. Van Kampen, "On the theory of stationary waves in plasmas," *Physica*, vol. 21, no. 6-10, pp. 949–963, 1955.

[43] N. Van Kampen, "The dispersion equation for plasma waves," *Physica*, vol. 23, no. 6, pp. 641–650, 1957.

[44] K. Oide and K. Yokoya, "Longitudinal single-bunch instability in electron storage rings," Tech. Rep. KEK-Preprint-90-10, 1990.

[45] I. Karpov, T. Argyropoulos, and E. Shaposhnikova, "Thresholds for loss of Landau damping in longitudinal plane," *Phys. Rev. Accel. Beams*, vol. 24, p. 011002, Jan 2021.

[46] A. Vlasov, "On the kinetic theory of an assembly of particles with collective interaction," *Russ. Phys. J.*, vol. 9, pp. 25–40, 1945.

[47] I. Karpov. Matrix Equations for LOngitudinal beam DYnamics (MELODY) code, `https://gitlab.cern.ch/ikarpov/melody`.

[48] H. Wiedemann, *Particle accelerator physics*. Springer Nature, 2015.

[49] K. Y. Ng, *Physics of intensity dependent beam instabilities*. World Scientific, 2006.

[50] L. Palumbo, V. Vaccaro, and M. Zobov, "Wake fields and impedance," Tech. Rep. physics/0309023, LNF-94-041-P, LNF-94-041-P, 1995.

[51] A. W. Chao, "Physics of collective beam instabilities in high energy accelerators," *Wiley series in beam physics and accelerator technology*, 1993.

[52] S. Y. Lee, *Accelerator physics*. World Scientific Publishing Company, 2018.

[53] Y. Funakoshi *et al.*, "The SuperKEKB Has Broken the World Record of the Luminosity," *JACoW*, vol. IPAC2022, pp. 1–5, 2022.

[54] T. Bohl, T. P. R. Linnecar, E. Shaposhnikova, and J. Tückmantel, "Study of different operating modes of the 4th RF harmonic Landau damping system in the CERN SPS," Tech. Rep. CERN-SL-98-026-RF, 1998.

[55] H. Damerau, S. Hancock, A. Lasheen, and D. Perrelet, "RF Manipulations for Special LHC-Type Beams in the CERN PS," in *Proc. 9th International Particle Accelerator Conference (IPAC'18), Vancouver, BC, Canada, April 29-May 4, 2018*, no. 9 in International Particle Accelerator Conference, (Geneva, Switzerland), pp. 1971–1974, JACoW Publishing, June 2018.

[56] H. Damerau, "Introduction to Non-linear Longitudinal Beam Dynamics," in *CAS - CERN Accelerator School 2019: Introduction to Accelerator Physics*, 8 2021.

[57] E. Shaposhnikova, T. Bohl, and T. Linnecar, "Beam transfer functions and beam stabilisation in a double RF system," in *Proceedings of the 2005 Particle Accelerator Conference*, pp. 2300–2302, IEEE, 2005.

[58] B. W. Zotter and S. A. Kheifets, *Impedances and wakes in high-energy particle accelerators*. World Scientific, 1998.

[59] J. Liouville, "Note sur la théorie de la variation des constantes arbitraires," *Journal de mathématiques pures et appliquées*, vol. 3, pp. 342–349, 1838.

[60] C. N. Lashmore-Davies, "Kinetic theory and the Vlasov equation," 1987.

[61] G. Besnier, "Stabilité des oscillations longitudinales d'un faisceau groupe se propageant dans une chambre a vide d'impedance reactive," *Nuclear Instruments and Methods*, vol. 164, no. 2, pp. 235–245, 1979.

[62] E. Shaposhnikova, "Bunched beam transfer matrices in single and double RF systems," Tech. Rep. CERN-SL-94-19, CERN-SL-94-19-RF, CERN, Geneva, 1994.

[63] A. Burov, "Dancing bunches as van Kampen modes," in *Proceedings of the 24th Particle Accelerator Conference*, pp. 94–96, IEEE, 2011.

[64] J. B. J. Fourier, *Théorie analytique de la chaleur*. Gauthier-Villars et fils, 1888.

[65] K. Oide, "A mechanism of longitudinal single-bunch instability in storage rings," *Part. Accel.*, vol. 51, no. KEK-Preprint-94-138, pp. 43–52, 1994.

[66] M. D'Yachkov and R. Baartman, "Longitudinal single bunch stability," *Part. Accel.*, vol. 50, no. C94-10-17.2, pp. 105–116, 1995.

[67] Y. Shobuda and K. Hirata, "Longitudinal instability for a purely inductive wake function," *Physical Review E*, vol. 60, no. 2, p. 2414, 1999.

[68] L. Intelisano, H. Damerau, and I. Karpov, "Threshold for loss of longitudinal Landau damping in double harmonic RF systems," in *Proc. HB'21*, no. 64 in ICFA ABDW on High-Intensity and High-Brightness Hadron Beams, pp. 95–99, JACoW Publishing, Geneva, Switzerland, 04 2022.

[69] P. Bramham, S. Hansen, A. Hofmann, and P. Peschardt, "Active Landau Cavity on the 4th Harmonic of the RF Frequency," Tech. Rep. ISR-RF-TH-AH-cr (Run: 756/796/810), CERN, Geneva, 1977.

[70] E. A. George, A. Richard, and R. Ranjan, "Special functions," *Encyclopedia of Mathematics and its Applications*, vol. 71, 1999.

[71] I. Karpov, "Longitudinal mode-coupling instabilities of proton bunches in the CERN super proton synchrotron," *Phys. Rev. Accel. Beams*, vol. 26, p. 014401, Jan 2023.

[72] L. Intelisano, H. Damerau, and I. Karpov, "Measurements of longitudinal loss of Landau damping in the CERN Proton Synchrotron," in *Proc. 14th International Particle Accelerator Conference*, no. 14, pp. 2622–2625, JACoW Publishing, Geneva, Switzerland, 05 2023.

[73] L. Intelisano, H. Damerau, and I. Karpov, "Longitudinal loss of Landau damping in the CERN Super Proton Synchrotron at 200 GeV," in *Proc. 14th International Particle Accelerator Conference*, no. 14, pp. 2626–2629, JACoW Publishing, Geneva, Switzerland, 05 2023.

[74] S. v. d. Walt, S. C. Colbert, and G. Varoquaux, "The NumPy array: a structure for efficient numerical computation," *Computing in Science & Engineering*, vol. 13, no. 2, pp. 22–30, 2011.

[75] P. Virtanen *et al.*, "SciPy 1.0: fundamental algorithms for scientific computing in python," *Nature methods*, vol. 17, no. 3, pp. 261–272, 2020.

[76] R. Nishino and S. H. C. Loomis, "Cupy: A numpy-compatible library for nvidia GPU calculations," vol. 151, 2017.

[77] H. Timko, J. Esteban Müller, A. Lasheen, and D. Quartullo, "Benchmarking the Beam Longitudinal Dynamics Code BLonD," in *Proc. 7th of International Particle Accelerator Conference (IPAC'16), Busan, Korea, May 8-13, 2016*, (Geneva, Switzerland), pp. 3094–3097, JACoW, June 2016.

[78] D. Quartullo, L. Intelisano, I. Karpov, and G. Papotti, "Simulation Studies of Longitudinal Stability for High-Intensity LHC-Type Beams in the CERN SPS," in *Proc. 13th International Particle Accelerator Conference (IPAC'22)*, no. 13 in International Particle Accelerator Conference, pp. 2249–2252, JACoW Publishing, Geneva, Switzerland, 07 2022.

[79] C. Ohmori *et al.*, "Batch Compression Scheme for Multi-MW J-PARC," in *Proc. of International Particle Accelerator Conference (IPAC'17), Copenhagen, Denmark, 14-19 May, 2017*, no. 8 in International Particle Accelerator Conference, pp. 2294–2296, JACoW, May 2017.

[80] O. Geithner *et al.*, "Ion-optical measurements at cryring@esr during commissioning," in *Proc. 9th International Particle Accelerator Conference (IPAC'18), Vancouver, BC, Canada, April 29 - May 4, 2018*, no. 9 in International Particle Accelerator Conference, (Geneva, Switzerland), pp. 3161–3164, JACoW Publishing, June 2018.

[81] Y. Sugiyama *et al.*, "Simulation of Phase-space Offset Injection with Second Harmonic RF for Longitudinal Emittance Blow-up in J-PARC MR," *JPS Conf. Proc.*, vol. 33, p. 011031, 2021.

[82] F. C. Cai *et al.*, "Beam loading effects and microwave instability in the booster ring of a high intensity heavy-ion accelerator facility," *Phys. Rev. Accel. Beams*, vol. 23, p. 064402, Jun 2020.

[83] A. Lasheen, "Numerical noise due to binning in macroparticle simulations," Tech. Rep. CERN-ACC-NOTE-2022-0002, 2021.

[84] O. S. Brüning *et al.*, *LHC Design Report*. No. CERN-2004-003-V-1 in CERN Yellow Reports: Monographs, Geneva: CERN, 2004.

[85] H. J. Nussbaumer and H. J. Nussbaumer, *The fast Fourier transform*. Springer, 1982.

[86] O. M. Essenwanger, "Elements of statistical analysis," *The Netherlands: Elsevier*, 1986.

[87] A. Lasheen. "Single-bunch instability during ramp" (06/08/2015), Meetings of the LIU-SPS BD WG, CERN, `http://cern.ch/spsu/`.

[88] I. Karpov, T. Argyropoulos, S. Nese, and E. Shaposhnikova, "New Analytical Criteria for Loss of Landau Damping in Longitudinal Plane," in *Proc. HB'21*, no. 64 in ICFA ABDW on High-Intensity and High-Brightness Hadron Beams, pp. 100–105, JACoW Publishing, Geneva, Switzerland, 04 2022.

[89] B. W. Zotter, "The effective coupling impedance for bunched beam instabilities," Tech. Rep. CERN-ISR-TH-78-16, ISR-TH-78-16, 1978.

[90] Y. I. Alexahin, "On the Landau damping and decoherence of transverse dipole oscillations in colliding beams," *Part. Accel.*, vol. 59, no. CERN-SL-96-064-AP, pp. 43–74, 1996.

[91] H. Damerau *et al.*, "LHC injectors upgrade, technical design report," Tech. Rep. CERN-ACC-2014-0337, 2014.

[92] E. Shaposhnikova *et al.*, "Identification and reduction of the CERN SPS impedance," in *Proc. 57th ICFA Adv. Beam Dyn. Workshop High-Intensity High Brightness High Power Hadron Beams*, 2016.

[93] T. Roggen *et al.*, "The SPS 200 MHz TWC impedance after the LIU upgrade," in *Proc. of ICFA Advanced Beam Dynamics Workshop on High-Intensity and High-Brightness Hadron Beams (HB'16)*, no. 57, pp. 76–80, JACoW, Aug 2016.

[94] G. Hagmann *et al.*, "The CERN SPS Low level RF: The Cavity-Controller," in *Proc. 13th International Particle Accelerator Conference (IPAC'22)*, no. 13 in International Particle Accelerator Conference, pp. 903–906, JACoW Publishing, Geneva, Switzerland, 07 2022.

[95] A. Spierer *et al.*, "The CERN SPS Low Level RF: The Beam-Control," in *Proc. 13th International Particle Accelerator Conference (IPAC'22)*, no. 13 in International Particle Accelerator Conference, pp. 895–898, JACoW Publishing, Geneva, Switzerland, 07 2022.

[96] A. Lasheen and E. Shaposhnikova, "Evaluation of the CERN super proton synchrotron longitudinal impedance from measurements of the quadrupole frequency shift," *Phys. Rev. Accel. Beams*, vol. 20, p. 064401, Jun 2017.

[97] CERN SPS Longitudinal Impedance Model, `https://gitlab.cern.ch/longitudinal-impedance/SPS`.

[98] P. Kramer *et al.*, "In situ measurements of the SPS 200MHz accelerating cavity III," Tech. Rep. CERN-ACC-NOTE-2015-0021, 2015.

[99] T. Roggen, R. Calaga, F. Caspers, and C. Vollinger, "Measurements on the SPS 200 mhz travelling wave cavity towards an impedance model," Tech. Rep. CERN-ACC-NOTE-2016-0051, 2016.

[100] C. Zannini, *Electromagnetic simulation of CERN accelerator components and experimental applications*. PhD thesis, 2013.

[101] T. Kroyer, E. Gaxiola, and F. Caspers, "Longitudinal and transverse wire measurements for the evaluation of impedance reduction measures on the MKE extraction kickers," Tech. Rep. AB-Note-2007-028, CERN-AB-Note-2007-028, 2007.

[102] J. Campelo, "Longitudinal impedance characterization of the CERN SPS vacuum flanges," in *Proc. 6th International Particle Accelerator Conference (IPAC'15), Richmond, VA, USA, May 3-8, 2015*, no. 6, (Geneva, Switzerland), pp. 363–365, JACoW, June 2015.

[103] P. Baudrenghien, "Low-level RF - Part I: Longitudinal dynamics and beam-based loops in synchrotrons," in *CERN Accelerator School: Course on RF for Accelerators*, 1 2012.

[104] S. L. Hahn, *Hilbert Transforms in Signal Processing*. Norwood, MA, USA: Artech House, 1996.

[105] M. J. D. Powell, "An efficient method for finding the minimum of a function of several variables without calculating derivatives," *The Computer Journal*, vol. 7, pp. 155–162, 01 1964.

[106] A. Lasheen *et al.*, "Beam measurement of the high frequency impedance sources with long bunches in the CERN super proton synchrotron," *Phys. Rev. Accel. Beams*, vol. 21, p. 034401, Mar 2018.

[107] J. Campelo *et al.*, "An Extended SPS Longitudinal Impedance Model," in *Proc. 6th International Particle Accelerator Conference (IPAC'15), Richmond, VA, USA, May 3-8, 2015*, no. 6, pp. 360–362, JACoW, June 2015.

[108] M. Morvillo *et al.*, "The PS 13.3-20 MHz RF systems for LHC," in *Proceedings of the 2003 Particle Accelerator Conference*, vol. 3, pp. 1724–1726 vol.3, 2003.

[109] D. Sagan, "On the physics of Landau damping," Tech. Rep. CLNS-93-1185, 1 1993.

[110] A. Hofmann, "Landau damping," in *CAS - CERN Accelerator School: Intermediate Accelerator Physics*, pp. 271–304, CERN, 2006.

[111] W. Herr, "Introduction to Landau damping," *arXiv:1601.05227*, 2016.